ÉCOLE CENTRALE LYON

N°ordre : 2011-37

Thèse de l'Université de Lyon

Délivrée par l'Ecole Centrale de Lyon
Spécialité : Mécanique des Fluids

Soutenue prévue le 09 novembre 2011 à l'Ecole Centrale de Lyon
par

Mlle Tian DENG

Préparée au Laboratoire de Mécanique de Fluides et d'Acoustique
Directeur de thèse :
Professeur Mikhael Gorokhovski

LES combined with statistical models of spray formation closely to air-blast atomizer

Ecole Doctorale Mécanique et Energétique

Composition du jury:

Gérard LAVERGNE	Professeur, SupAero de Toulouse	Rapporteur
Jean COUSIN	Professeur, INSA de Rouen	Rapporteur
Michel LANCE	Professeur, Université Lyon I	Examinateur
Mikhael GOROKHOVSKI	Professeur, Ecole Centrale de Lyon	Directeur de thèse
Catherine LE RIBAULT	Chargée de recherche au CNRS, LMFA	Co-encadrante de thèse
Lipeng LU	Professeur, Université de Beihang, Pekin	Examinateur
Xiaofeng SUN	Professeur, Université de Beihang, Pekin	Examinateur

UNIVERSITÉ DE LYON

Acknowledgements

This thesis was prepared and accomplished in the Laboratoire de Mcanique des Fluides et d'Acoustique in Ecole Centrale de Lyon. I want to thank the Director of the Laboratory, Michel Lance, for his kindly support.

I am very thankful to the jury members, Professor Grard LAVERGNE, Professor Jean COUSIN, Professor Michel LANCE, Professor LU Lipeng and Professor SUN Xiaofeng, for the time and energy they have put in reading my manuscript and their interesting and valuable comments on this work.

I would especially like to express my deepest and sincere gratitude to my supervisor Professor Mikhael GOROKHOVSKI who awakened my interest in this topic and gave me continuous guidance, steadfast support, limitless patience, encouragement, and invaluable advices during the past three years. This thesis could not have been accomplished without his supervision and help he provided me with amply.

I would like to thank my co-supervisor Dr. Catherine LE RIBAULT. Her assistance throughout duration of my project and knowledge on programming she shared with me contributed greatly to the completion of this work. I would like to extend my appreciation to Dr. SHAO Liang who gave me much encouragement and help during these three years. I always remember his friendliness. I would also like to thank Professor HUANG Yong, who helped me on both the work and the life when I was in Beihang University in China, and he is also concerned with my thesis.

Also many thanks to all the great people at the Laboratoire de Mcanique de Fluides et d'Acoustique. I have been extremely lucky and blessed

with many cheerful and friendly colleagues and friends. Here, I would like to express my special thanks to Jean-Marc Vignon and Rémi Zamansky for their selfless help. My friends together with me in l'Ecole Centrale de Lyon have been very encouraging and patient with me. They have helped me in so many ways than they would ever know.

The financial support from the China Scholarship Council (CSC) that made this project possible is deeply acknowledged.

I am sure there are others who have helped along the way. I believe they will not be offended if I have neglected to mentioned their names, but I am sure they know how thankful I was for their support.

Last, but not least, I am deeply grateful to my parents for always being there for me, through all the difficult times. Without their patience, understanding and great support this dissertation may well have never been completed. They are, without a doubt, the best parents I could imagine. I have not thanked them nearly enough for what they have done and continue to do for me. I would like to thank my brother, DENG Yan, for the love he has always shown towards me.

Résumé

Cette thèse présente une extension de l'approche stochastique de l'atomisation primaire de type air assisté près d'un injecteur. Cette approche avait déjà été introduite dans les publications de Gorokhovski *et al*. Dans le cadre de la simulation des grandes échelles, la zone d'atomisation primaire est simulée comme un corps immergé avec une structure stochastique. Ce dernier est défini par la simulation stochastique de la position et de la courbure de l'interface entre le liquide et le gaz. La simulation de la position de l'interface est basée sur l'hypothèse de symétrie d'échelle pour la fragmentation. La normale extérieure à l'interface est modélisée en supposant une relaxation statistique vers l'isotropie. Les statistiques de la force du corps immergé servent de conditions aux limites pour le champ de vitesse issu de la LES ainsi que pour la production des gouttes de l'atomisation primaire. Celles-ci sont ensuite transportées par une approche lagrangienne. Les collisions entre les gouttes dans la zone d'atomisation primaire sont prises en compte par analogie avec l'approche standard de la théorie cinétique des gaz. Une fermeture est proposée pour la température statistique des gouttelettes. Cette approche est validée par des comparaisons avec les mesures expérimentales de la thèse de Hong. Les résultats numériques pour la vitesse et de la taille des gouttes dans le spray à différentes distances du centre du jet et de l'orifice de la buse sont relativement proches des résultats expérimentaux. Différentes conditions d'entrée pour la vitesse sont testées et comparées aux résultats expérimentaux. Par ailleurs, le rôle spécifique de la zone de recirculation devant le dard liquide est soulignée par le battement du dard liquide et la production de gouttelettes.

Mots clés : écoulement diphasique, atomisation, modèles stochastiques, force de corps immergé, simulation des grandes échelles, dispersion de gouttelettes , combustion interne, moteurs de fusée.

Abstract

This thesis introduced an extension to stochastic approach for simulation of air-blast atomization closely to injector. This approach was previously proposed in publications of Gorokhovski with his PHD students. Our extension of this approach is as follows. In the framework of LES approach, the contribution of primary atomization zone is simulated as an immersed solid body with stochastic structure. The last one is defined by stochastic simulation of position-and-curvature of interface between the liquid and the gas. As it was done previously in this approach, the simulation of the interface position was based on statistical universalities of fragmentation under scaling symmetry. Additionally to this, we simulate the outwards normal to the interface, assuming its stochastic relaxation to isotropy along with propagation of spray in the down-stream direction. In this approach, the statistics of immersed body force plays role of boundary condition for LES velocity field, as well as for production of primary blobs, which are then tracked in the Lagrangian way. In this thesis, the inter-particle collisions in the primary atomisation zone are accounted also by analogy with standard kinetic approach for the ideal gas. The closure is proposed for the statistical temperature of droplets. The approach was assessed by comparison with measurements of Hong in his PHD. The results of computation showed that predicted statistics of the velocity and of the size in the spray at different distances from the center plane, at different distances from the nozzle orifice, at different inlet conditions (different gas velocity at constant gas-to-liquid momentum ratio, different gas-to-liquid momentum ratio) are relatively close to measurements. Besides, the specific role of recirculation zone in front of the liquid core was emphasized in the flapping of the liquid core and in the droplets production.

Keywords: two-phase flow, atomization, stochastic model, immersed body force, Large Eddy Simulation, droplet dispersion, internal combustion and rocket engines

Contents

List of Figures

List of Tables

Chapter 1

Introduction

1.1 Introduction to air-blast atomization: knowledge from experiments and scales

In many propulsion power related applications, fuel or oxidizer, initially introduced into combustion chamber as a continuous liquid jet, disintegrates into filaments and drops due to interaction with the gas. The vapour issued from the produced liquid fragments mixes with the turbulent gas flow and chemically reacts. If the produced spray is not well-atomized into small droplets, the mixing is not perfect, and the combustion process is incomplete. This provokes the power loss, an additional consumption of the fuel and increased formation of pollutions. Therefore understanding of complex process of spray formation, closely region, and its prediction is of great interest to engineers, and in general, to researchers in the domain of fluid mechanics.

In air-craft and rocket engines, the liquid jet is atomized by a coflowing high-speed jet of the gas. Such a type of breakup is referred to as air-blast atomization (Chigier, 1991; Engelbert *et al.*, 1995; Farago & Chigier, 1992; Lasheras & Hopfinger, 2000; Villermaux, 2007; Eggers & Villermaux, 2008; Gorokhovski & Herrmann, 2008). Our work is focused on simulation of spray formation and dynamics controlled by air-blast atomization.

A typical configuration of air-blast atomizer in air-craft engine is shown in Figure 1.1. In such injector, the liquid fuel is injected at low pressure, as a thin

annular liquid sheet. Two high speed airstreams co-flow along with the liquid and transfer a large amount of kinetic energy. Because of such contact with the gas-stream, the liquid sheet is sheared on either side. This leads to disintegration of the liquid into ligaments, threads, and small droplets.

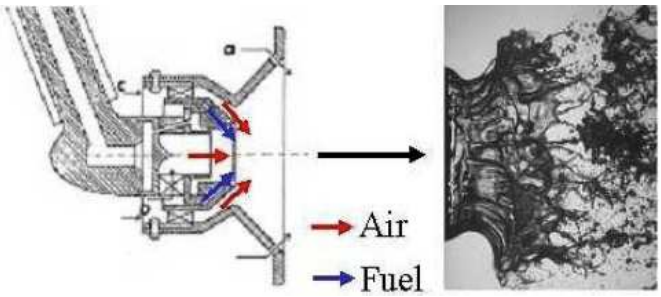

Figure 1.1: Atomization of annular liquid sheet in conditions of air-craft engine (Lalo *et al.*, 2006).

Figure 1.2 shows schematically such a type of atomization in the rocket-like conditions. Here the central jet of liquid oxygen emerges at low velocity, and is entrained into motion by high-speed stream of gaseous hydrogen. The sheared liquid jet becomes wavy, with the following disruption into filaments, and stripping of fine droplets by the high-speed gas motion.

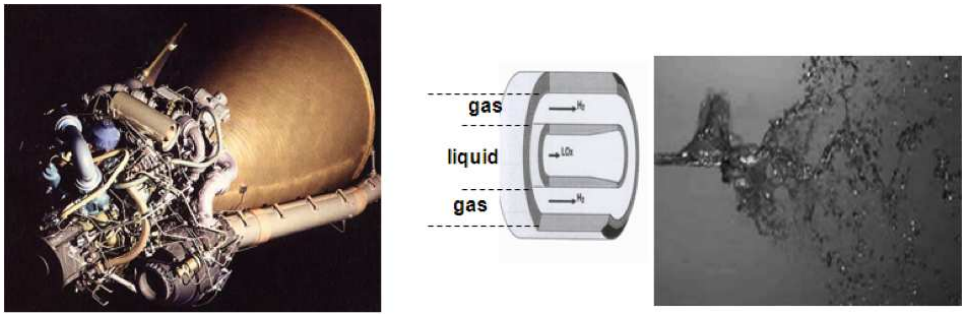

Figure 1.2: Schematic of air-blast atomizer in conditions of rocket engine.

In both cases, it is seen that in close vicinity of injector, the liquid is not yet fragmented. Usually this zone is called as liquid core. It is defined as the area of flow in which the fraction mass of liquid is close to unity, and the liquid bulk retains as maximum unbroken (Hopfinger, 2001). Many complex interactions

appear at the periphery of the liquid core, leading to formation of filaments and their detachment from the liquid core. Such a phase of the liquid core depletion is called primary atomization. The fragments pinched off from the liquid core may collide. Eventually, the collisions between fragments may cause their coalescence or breakup. The fragments may be also stripped by the fast gas flow, producing the small droplets. The phase of production of small droplets from the parent liquid fragments is usually called as secondary atomization process. It is clear that the smaller produced droplets are, the more intensive evaporation is, then the better mixing between gaseous reactants is, and consequently the more efficient combustion occurs. Schematically the spray combustion structure is given in Figure 1.3.

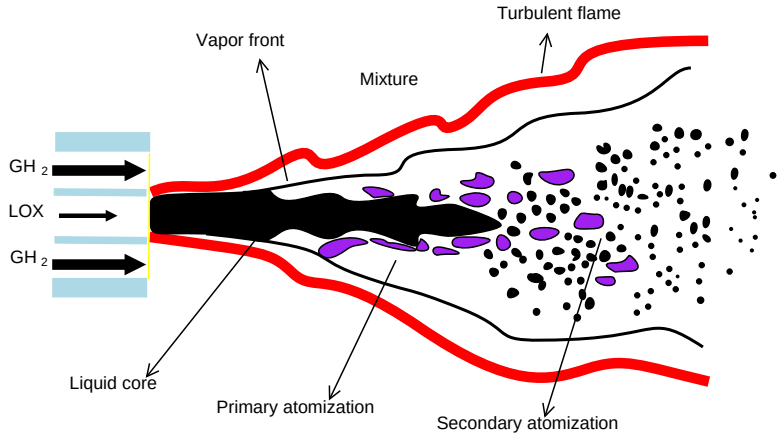

Figure 1.3: Schematic of the spray combustion.

In view of the practical importance, the experimental and analytical studies of air-blast atomization were performed in scientific groups of Hopfinger, Villermaux, Cartellier, Lasheras, with their Ph.D. students Rehab (1997; Rehab *et al.*, 1997), Raynal (1997), Marmottant (2001; Marmottant & Villermaux, 2004), Hong (2003; Hong *et al.*, 2002), Rayana (2007) and Varga (2002; Varga *et al.*, 2003). These and other experimental studies (see Engelbert *et al.*, 1995, for example) established a large number of dimensionless scaling parameters involved in primary air-blast atomization. It certainly includes the Weber number:

$$We = \frac{\rho_g (u_{g,0} - u_{l,0})^2 D_l}{2\sigma} \tag{1.1}$$

and the Reynolds numbers:

$$Re_l = \frac{\rho_l u_{l,0} D_l}{\mu_l} \quad \text{and} \quad Re_g = \frac{u_{g,0}(D_g - D_l)}{\nu_g} \tag{1.2}$$

Here $u_{l,0}$ is the inlet velocity of liquid, $u_{g,0}$ is the inlet velocity of the gas stream, σ is the surface tension, D_l is the inlet diameter for the liquid jet, and $D_g - D_l$ is the inlet size of the coflowing gaseous jet. However, the significant parameters are also the gas-to-liquid density, mass and dynamic pressure ratios: ρ_l/ρ_g, $m = \frac{\rho_g u_{g,0}(D_g^2 - D_l^2)}{\rho_l u_{l,0} D_l^2}$ and $M = \frac{\rho_g u_{g,0}^2}{\rho_l u_{l,0}^2}$. From these three parameters, the primary role was attributed to the last one, namely to the momentum ratio (this parameter will be emphasized in the present study, as well):

$$M = \frac{\rho_g u_{g,0}^2}{\rho_l u_{l,0}^2} \tag{1.3}$$

For example, the experimental correlations between averaged length L of the liquid core and parameters (1.1)-(1.3) were proposed by expressions given in Table 1.1.

Table 1.1: Experimental correlations between averaged length of the liquid core and parameters (1.1)-(1.3).

Experiment	Gas	Liquid	$D_l(mm)$	$D_g(mm)$	Experimental Correlations
Eroglu *et al.* (1991)	air	water	0.971	10.36	$\frac{L}{D_l} = 0.66(\frac{We}{2})^{-0.4} Re^{0.6}$
Mayer & Branam (2004)	azote	ethanol	2.2	10	$\frac{L}{D_l} = 1.7(\frac{\rho_g}{\rho_l})^{0.18} \ln(\frac{Re_l}{\sqrt{We}}) - 0.16$
Lasheras *et al.* (1998)	air	water	3.8	5.6	$\frac{L}{D_l} = \frac{6}{\sqrt{M}}$

Inside the coaxial nozzle, the high-speed gas flow develops the boundary layer on the rigid boundary of separation between two parallel flowing streams of the

gas and the liquid. The non-dimensional thickness of the incoming boundary layer

$$\frac{\delta_g}{D_g - D_l} \tag{1.4}$$

was also defined as the very significant parameter; its contribution is described hereafter. As an important parameter, one can also reference the Ohnesorge number (Marmottant, 2001)

$$Oh = \frac{\mu_l}{\sqrt{\rho_l \sigma D_l}} \tag{1.5}$$

From the knowledge obtained in referenced above studies, the dominant mechanism of air-blast atomization is proposed. It is schematically shown in Figure 1.4.

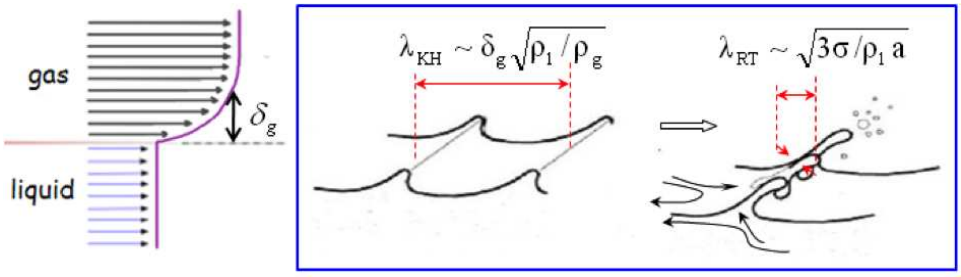

Figure 1.4: Schematic of primary break-up mechanisms (Hong, 2003).

At the exit, the boundary layer interacts with the liquid jet and gives rise to the Kelvin-Helmholtz instability on the free surface, resulting in longitudinal waves. According to Raynal (1997), the most unstable longitudinal wavelength λ_{KH} of the Kelvin-Helmholtz instability is controlled by the thickness of incoming boundary layer, δ_g. At a high Weber number, Villermaux (1998) estimated:

$$\lambda_{KH} \approx C_{KH} (\frac{\rho_l}{\rho_g})^{\frac{1}{2}} \delta_g \tag{1.6}$$

where for coaxial air-blast atomizer, the parameter $C_{KH} = 2$ (Marmottant, 2001). Raynal (1997) used the Blasius expression for thickness of the boundary layer: $\delta_g = C_\delta \frac{D_g - D_l}{2\sqrt{Re_g}}$, and $Re_g = \frac{u_{g,0}(D_g - D_l)}{\nu_g}$ is the Reynolds number. From measurements, Marmottant (2001) has found that $C_\delta = 5.6$.

The evolution of Kelvin-Helmholtz instability, authors refer to as primary instability phase. From other side, the issuing jet is subject to the large scale instability of flow, and it gets flapping. Then the crests of primary instability waves are exposed to the gas flow; those crests get accelerated. This leads to the rapid evolution of the Rayleigh-Taylor instability in the transversal direction (Varga, 2002; Hong, 2003). Arising of such type of instability authors refer to as the secondary instability phase. The expression of most amplified wavelength of the Rayleigh-Taylor instability is known from Chandrasekhar (1961):

$$\lambda_{RT} = 2\pi\sqrt{\frac{3\sigma}{\rho_l a}} \tag{1.7}$$

where a denotes the acceleration of liquid.

The filaments of order λ_{RT} are fragmented by the fast motion of the gas, producing primary drops of size:

$$r < \lambda_{RT} \tag{1.8}$$

These drops may be subjected to the secondary atomization process, thereby forming the spray. The described scenario is demonstrated in Figure 1.5 taken from Rayana (2007).

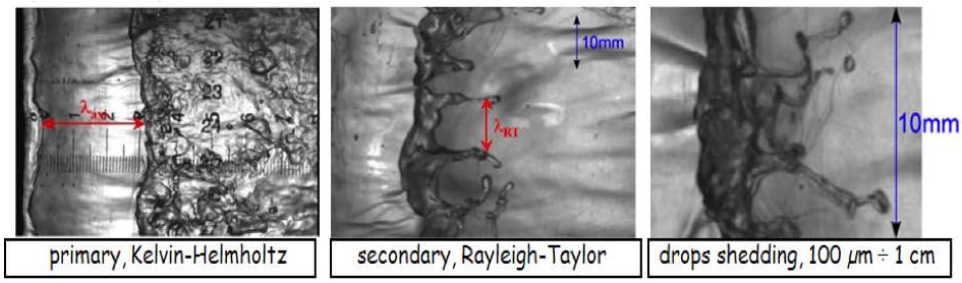

Figure 1.5: Scenario of the primary atomization and secondary atomization process (Rayana, 2007).

In order to estimate from (1.7) the typical size of stripped droplet, proportionally to λ_{RT}, Lasheras & Hopfinger (2000), Varga *et al.* (2003) proposed the following scheme, Figure 1.6. The acceleration due to drag force acting on the unit mass of the wave's crest, which is exposed to the gas-stream by its interface

A_n, is proposed to be $a = \frac{1}{2}\frac{C_D\rho_g(u_{g,0}-u_c)^2A_n}{m_n}$, where C_D is constant, and u_c is the convection velocity of the interface:

$$u_c = \frac{\sqrt{\rho_g}u_{g,0} + \sqrt{\rho_l}u_{l,0}}{\sqrt{\rho_g} + \sqrt{\rho_l}} \tag{1.9}$$

The expression (1.9) was given by Dimotakis (1986) from the equality of dynamic pressures on $\rho_g(u_g - u_c)^2 = \rho_l(u_c - u_l)^2$. Then assuming that the mass of filament is $m_n = \rho_l A_n b$ where b is the initial thickness of the liquid layer. Under the proposed mechanism in Figure 1.6, the initial thickness of the web is going to destabilize the form of filaments is proportional to the wavelength associated with the primary instability λ_{KH}, Hong (2003) proposed $b = \alpha_n\lambda_{KH}$ (α_n is constant). Hong (2003) and Varga (2002) identified α with the experiments: $\alpha = 0.1$ with Varga (2002) and $\alpha = 0.04$ with Hong (2003). Then transverse instability wavelength was obtained:

$$\lambda_{RT} = 2\pi\sqrt{\frac{3\sigma}{\rho_l a}} = 2\pi\left(\frac{6\sigma\alpha_n\delta_g C_{KH}}{\rho_g C_d}\right)^{\frac{1}{2}}\left(\frac{\rho_l}{\rho_g}\right)^{\frac{1}{4}}\frac{1}{u_{g,0} - u_{l,0}} \tag{1.10}$$

In fact, if the typical velocity of interface is assumed to be (1.9), this interface moves at constant velocity without acceleration. This motivated (Gorokhovski *et al.*, 2009) to propose and to assess estimation of λ_{RT} differently from (1.10) expression. Authors assumed that the wave crest with characteristic length λ_{KH} is accelerated by the drag force $F = \frac{1}{2}C_D\rho_g(u_{g,0} - u_{l,0})^2A_n$. Then the kinetic energy of the gas flow, which is transferred to the liquid element per unit time, is $F \cdot u_{g,0}$. Writing the momentum of the liquid element as $\rho_l u_{l,0}A_n\lambda_{KH}$, the acceleration can be expressed as $a = \frac{\frac{1}{2}C_D\rho_g(u_{g,0}-u_{l,0})^2u_{g,0}}{\rho_l u_{l,0}\lambda_{KH}}$, and λ_{RT} from (1.7) is

$$\lambda_{RT} = 2\pi\left(\frac{6C_{KH}}{C_D}\right)^{\frac{1}{2}}\left(\frac{\rho_l}{\rho_g}\right)^{\frac{1}{4}}\delta_g We_{\delta_g}^{-\frac{1}{2}}\left(\frac{u_{l,0}}{u_{g,0}}\right)^{\frac{1}{2}} \tag{1.11}$$

where

$$We_{\delta_g} = \frac{\rho_g(u_{g,0} - u_{l,0})^2\delta_g}{\sigma} \tag{1.12}$$

It might be noted that Hong (2003) observed significance of the injection velocity of liquid on the size spray droplets; in expression (1.11), this velocity appears explicitly.

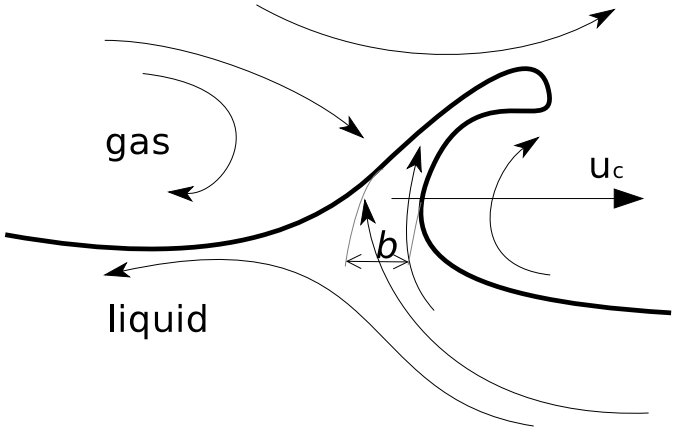

Figure 1.6: Schematic of a primary longitudinal wave exposed on the oncoming gas flow in a coaxial liquid-gas jet (Varga, 2002; Hong, 2003).

As to the typical size of droplets in the far-field of spray, it is usually determined by critical or maximum stable size, when the disruptive hydrodynamic forces are balanced by the capillary forces:

$$r_{cr} = \frac{We_{cr}\sigma}{\rho_g U_{rel}^2} \tag{1.13}$$

where U_{rel} is the relative between liquid and gas velocity, and We_{cr} is the critical Weber number, which can be taken equal to 6 over a large interval of Ohnesorge numbers (Gel'fand *et al.*, 1975; Pilch & Erdman, 1987). The question is how to estimate U_{rel}. Kolmogorov, in his article (Kolmogorov, 1941), proposed that a drop in the turbulent flow is stretched up to the moment when this stretching is of order of surface tension force. Then he estimated U_{rel} from expression of typical increment of the gas velocity in homogeneous stationary turbulence. If ε is the viscous dissipation, his estimation was:

$$r_{cr} = \frac{1}{2}\left(\frac{We_{cr}\sigma}{\rho_g \varepsilon^{2/3}}\right)^{3/5} \tag{1.14}$$

These expressions do not account for the liquid density. At the same time, a moving in turbulent flow droplet will respond to its turbulent stretching only partially, due to its inertia. Gorokhovski (2001) used relation given in Kuznetsov & Sabel'nikov (1990):

$$\langle U_{rel}^2 \rangle \approx \varepsilon \tau_{st} \tag{1.15}$$

where τ_{st} is the Stokes time scale:

$$\tau_{st} = \frac{2\rho_l r^2}{9\rho_g \nu_g} \frac{1}{1 + 0.15 Re_p^{0}.687} \tag{1.16}$$

Using this relation, Gorokhovski (2001) estimated:

$$r_{cr} = \frac{1}{2} (\frac{We_{cr} 18 \nu_g \sigma}{\varepsilon \rho_l})^{1/3} \tag{1.17}$$

Both relations are valid only if the mechanism of secondary atomization is attributed to turbulence in the gas flow.

1.2 Proposed approach for simulation and structure of the manuscript

Evaluating the influence of all parameters in referenced in Section 1.1 for different regimes of break-up, and in realistic operating conditions (high velocities and pressures; strongly non-homogeneous 3D dense gas-liquid flow) is a difficult task for experimentalists. The numerical modeling of primary airblast atomization may provide a way of overcoming this problem. The question raised is: how to model? There is a solid body of papers and books, where modelling gas flows laden by dispersed solid particles or liquid droplets are described. The main numerical approaches are well-known. They incorporate the governing equations for the gas mixture, averaged in the framework of RANS or filtered in the framework of LES, and completed by closure model for the turbulent viscosity. The numerical integration of those equations is performed along with computation of each individual trajectory of a particle, or of a parcel of particles. Coupling between phases, models for evaporation and combustion, for droplet dispersion and collision, all such models are also included into simulation. However closely to injector, where spray is in the phase of formation, the liquid phase is no more dispersed, and the remaining question is again: how to model? The choice of possible way which could be known from the literature is limited. The first alternative

is to apply a DNS-like approach on the basis of integration of the Navier-Stokes equations, with identification (capturing or tracking) of the gas-liquid interface at each time step. In such a technique, the liquid fragments are pinched off, when the progressively stretched filament becomes of order of the typical size of the numerical cell. Having a close look on an elements of breakup (dynamics of a filament, a drop formation, a drop coalescence, evolution of primary instability), the DNS-like approach may significantly help in understanding of processes involved. However, when the Weber number is high, the computational expense associated with resolution of length scales of breaking ligaments is very high. Hence application of such approaches in practical conditions, in a whole domain of atomizing spray, is limited by the Weber and the Reynolds numbers. Besides the problem of the mass conservation during breakage process remains open. Another way is to consider the primary atomization process in the framework of a single "fluid", controlled by turbulent mixing of a high-density jet with an ambient gas, in lines of RANS approach. This approach does not require much of CPU time, and was shown computationally efficient in practical applications. In the case of air-blast atomization, the future studies may show the efficiency of this approach, despite some reserve concerning application the gradient-like hypothesis in the framework of this approach. The third way, may be the simplest one, is to integrate the governing equations for the gaseous phases by LES approach, simultaneously with injection of round proliferating blobs (initially, of the nozzle exit diameter) into computational domain. The model of primary blobs breakup may include the main mechanism of primary atomization. We have chosen the forth way, which is stochastic approach. In this approach, the main mechanism of primary atomization is presumed, as a global parameter of the stochastic process. The liquid distribution, the configuration of the liquid core and its curvature are resulted from the stochastic modeling along with LES computation of turbulent gas flow. The region closely to injector is considered as an immersed porous body with the stochastic structure. The immersed body force is introduced as an extra-force acting on the gas flow. The filtered Navier-Stokes equations to be resolve are:

$$\frac{\partial \langle u_i \rangle}{\partial t} = \begin{cases} -\frac{\partial \langle u_i u_j \rangle}{\partial x_j} + \frac{1}{\rho_g} \frac{\partial \langle \sigma_{ij} \rangle}{\partial x_j}, & \text{if} \quad P_l = 0 \\ P_l \dot{U}_S n_i, & \text{if} \quad P_l \neq 0 \end{cases}$$

1.2 Proposed approach for simulation and structure of the manuscript

These equations contain three variables: (i) the probability to find the liquid in the vicinity of injector $P_l(\vec{x},t)$; (ii) the local magnitude of interface acceleration $\dot{U}_S(\vec{x},t)$; (iii) the outwards stochastic direction of interface $n_i(\vec{x},t)$, which may be associated with the instantaneous curvature. These variables need to be modeled. The dispersed phase considered along with these equations is governed by the following equation:

$$\frac{d\overline{v_{p,i}}}{dt} = \frac{\langle u_i \rangle - \overline{v_{p,i}}}{\tau_{st}} - \frac{\partial}{\partial x_i}(\frac{T_p}{m_p})$$

where $\overline{v_{p,i}}$ is component of the liquid drop velocity averaged over inter-drop collisions; T_p is the statistical temperature due to collisions (activated only in subregion $0 < P_l < 1$), and τ_{st} is the expression of the Stokes time. The idea of this approach was proposed in Gorokhovski (2010). The practical realization and assessment of this approach by comparison with measurements represents the objective of our present work.

The following structure of manuscript is as follows:

In Chapter 2, the main modern numerical approaches, developed for flows with atomizing spray, are described. This Chapter is ended up by motivation and formulation of the proposed approach.

In Chapter 3, the stochastic models, involved in this approach, are described and tested.

Chapter 4 is devoted to assessment of numerical method and finite-difference mesh, which was applied for simulation of turbulent gas flow.

Chapter 5 represents simulations with the inlet conditions of experiment of Hong (2003), and contains assessment and discussion on obtained numerical results. The manuscript is ended by Conclusion.

Appendixes A-E contain information on the applied numerical scheme, on the turbulence modeling, and on the Kelvin-Helmholtz and the Rayleigh-Taylor types of instabilities.

Chapter 2

Approaches for numerical simulations of two-phase immiscible flows with interface

Hereafter we will describe the main ideas in different approaches for numerical simulations of two-phase immiscible flows with interface. This description is based on two recent reviews (Gorokhovski, 2011; Gorokhovski & Herrmann, 2008).

2.1 Interfacial phenomena and conditions at the boundary gas/liquid

2.1.1 Surface tension and Laplace pressure

When the liquid is in contact with the gas, it forms an interface layer. The thickness of this layer is of order of typical radius of the intermolecular cohesion ($\sim 10^{-7}$ cm for simple molecules). In this layer, molecules interact not only with molecules in the liquid but also with neighboring molecules in the gas, which leads to difference in averaged free energy of molecules depending on proximity to the interface layer. For the molecules inside the liquid bulk, forces from all directions may cancel each other out, and the molecules may remain at near equilibrium. The molecules that are at the surface are pulled into the liquid bulk. Therefore

the surface layer is under intensive agitation; the molecules at the surface are continuously replaced through their motion into the bulk. The statistical result of such molecular agitation is the surface tension, providing specific physical properties of the interface layer, in difference with the interior of the liquid bulk.

Starting from the pioneer studies of Gibbs (1876), the interface layer is considered as a zero mass elastic membrane (similar to infinitely thin soap film) of surface area Σ that resists stretching and has a tendency to contract. Along with the volume V , the surface area Σ represents the new independent parameter in thermodynamics of heterogeneous systems. The thermodynamic force related to Σ is referred to as the surface tension σ. Its classical definition is as follows. The work needed to increase Σ on $d\Sigma$ during a process at constant temperature and volume, and without chemical reactions, is:

$$\delta W = dF_{\Sigma} = \sigma d\Sigma \tag{2.1}$$

where F_{Σ} is the free energy. It is seen that σ characterizes equilibrium between liquid and gas, and is defined by free energy available per unit surface area. An equilibrium shape of the interface (at equal temperatures and chemical potentials in both liquid and gas) is defined by the Laplace equation:

$$P^{(l)} - P^{(g)} = 2\sigma k \tag{2.2}$$

where $P^{(l)} - P^{(g)}$ is the pressure imbalance between liquid and gas, usually referred to as the interfacial pressure or the Laplace pressure, and k is the mean curvature in the given point of interface.

The variation of the surface tension with increasing temperature is inversely proportional to the absolute temperature:

$$(\frac{d\sigma}{dT})_{\Sigma} = -\frac{L}{T} \tag{2.3}$$

where L is the latent heat of formation of the unit surface. In classical thermodynamics (Bazarov, 1964), it is shown by analogy with the Carnot cycle, in which thin soap film was stretching first at the constant temperature, then stretched adiabatically, and further this soap film was contracted first at the constant temperature, and then adiabatically. More extended empirical correlations for σ can

be found in the literature (Vargaftik *et al.*, 1996). In the following, we will use the constant surface tension, and those extended correlations are not given in our manuscript.

If the area of the interface is significant (formation of liquid drops in air, or small gas bubbles in water), the effects of surface tension should be taken into account. To this end, two interesting historical examples were described in (Eggers & Villermaux, 2008). En 1508, Leonardo de Vinci considered a drop formation from a narrow liquid column running down (as it takes place in the case of a dripping faucet, for example). His reasoning was as follows. Falling liquid is accelerating due to the gravity, and the mass conservation in the liquid cylinder requires its retraction. Once the radius of liquid column is small enough, the drop is pinched off. The question was: what is the length of the column, when the drop is pinched off. If the final velocity at the moment of drops detachment is $v = \sqrt{2gx}$, the radius of the column is h, and the flow rate is $Q = \pi h^2 v$, the answer is: $x = \frac{Q^2}{(\pi h^2)^2 2g}$. Using for example the typical properties for the liquid glass column, $\pi h^2 \approx 10^{-5} cm^2$, $Q \approx 1 ml/s$, the value of x becomes unrealistically big: $x = 10^5$. The resolution of this paradox was given by Laplace in 1805, and more precisely by Rayleigh theoretically and by Plateau (1873) (experimentally). According to Laplace, the surface tension acts in two ways: effectively, it resists to the column retraction, as an elastic membrane, but once the cylindrical shape reached the critical radial curvature, the surface tension will drive this retraction, and will prompt the drops formation. The Rayleigh theory shows that exponential growth rate of the fastest-growing disturbance is given by

$$\tau_R = (\frac{\rho_l h_0^3}{\sigma})^{1/2} \tag{2.4}$$

where h_0 is the initial radius of the liquid column. It is seen that increasing h_0 accelerates the motion under surface tension. Rayleigh gives the wave-length corresponding to τ_R is :

$$\lambda \approx 2\pi \sqrt{\frac{3\sigma}{\rho_l g}} \sim 4.5 h_0 \tag{2.5}$$

which implies that the order of liquid column length, when the drop is pinched off, is of few its initial radii.

2.1.2 Classical conditions at the interface

Let us consider now the boundary condition at the interface between two moving media, liquid and gas. First, according to classical no-slip conditions, the viscous fluid sticks to both sides of the interface. This implies that on the interface:

$$(u_{g,i} - u_{l,i})n_i = 0 \tag{2.6}$$

where n_i are components of the outwards unit normal, directed from the liquid to the gas, and u_i are components of the velocity in each of two media. Hereafter a summation over the repeated indices is implied.

Second, since the surface tension is supposed to be constant, and the interface is supposed to be of zero mass, the resultant traction force at the interface is equivalent to the Laplace pressure (2.2) (Landau & Lifshitz, 2000):

$$n_k(\sigma_{ij}^{(g)} - \sigma_{ij}^{(l)}) = \sigma k n_i \tag{2.7}$$

where σ_{ij} is the stress tensor at the interface:

$$\sigma_{ij}^{(l,g)} = -\delta_{ij}p^{(l,g)} + 2\mu^{(l,g)}S_{ij}^{(l,g)} \tag{2.8}$$

and

$$S_{ij} = \frac{1}{2}(\frac{\partial u_i}{\partial x_j} + \frac{\partial u_j}{\partial x_i}) \tag{2.9}$$

is the strain rate tensor, $p^{(l,g)}$ and $\mu^{(l,g)}$ are the pressure and the viscosity respectively (either in the liquid or in the gas), δ_{ij} is the Kronecker's delta, and curvature is defined by

$$k = \frac{\partial n_j}{\partial x_j} \tag{2.10}$$

The condition (2.7) may be also written in the following form:

$$(2\mu_l S_{ij}^{(l)} - 2\mu_g S_{ij}^{(g)})n_j = (p^{(l)} - p^{(g)})n_i + \sigma k n_i \tag{2.11}$$

It should be noted that with (2.6), only tangential to the interface components of the strain rate tensor are involved into (2.11). Conditions (2.6), (2.11) are used

in recent numerical approaches developed for numerical simulations of two-phase immiscible flows with interface.

2.2 DNS Approaches

2.2.1 Immersed Boundary Formulation

Consider a viscous incompressible fluid fills by domain Ω containing an internal elastic zero mass boundary $\Sigma(t)$ that moves with the fluid and separates Ω into two regions $\Omega_1(t)$ and $\Omega_2(t)$ (see Peskin, 1977, with details in Peskin, 2007).

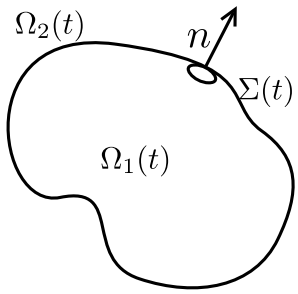

Figure 2.1: A viscous incompressible fluid filled domain Ω with boundary $\phi(t)$.

The motion is governed by the Navier-Stokes equations with source term. This source term represents density of surface tension force, which delta- concentrated on the moving boundary:

$$\rho(\frac{\partial u_i}{\partial t} + \frac{\partial u_i u_j}{\partial x_j}) = -\frac{\partial p}{\partial x_i} + \mu \frac{\partial^2 u_i}{\partial x_j \partial x_j} + f_i \tag{2.12}$$

$$f_i(\vec{x}, t) = \int_{\Sigma(t)} \sigma k(\vec{x}') n_i(\vec{x}') \delta(\vec{x} - \vec{x}') d\Sigma(\vec{x}') \tag{2.13}$$

$$\frac{\partial u_j}{\partial x_j} = 0 \tag{2.14}$$

Here $\delta(\vec{x})$ is three-dimensional Dirac function, $\delta(\vec{x}) = \delta(x_1)\delta(x_2)\delta(x_3)$. Integrating (2.13) over an arbitrary domain Φ ($d\vec{x} = dx_1 dx_2 dx_3$ is the element of volume of integration) , one yields:

$$\int_{\Phi} f_i(\vec{x},t)d\vec{x} = \int_{\Sigma(t)\cap\Phi} \sigma k(\vec{x}')n_i(\vec{x}')d\Sigma(\vec{x}') \tag{2.15}$$

It is seen that in the framework of formulation (2.12)-(2.14), the total contribution of surface tension force over an arbitrary domain Φ is defined by integration of this force over the interface containing in the interior of Φ. Equations (2.12)-(2.14) are equivalent to formulation from the book on Fluids Mechanics (Landau & Lifshitz, 2000):

$$\rho_l(\frac{\partial u_{l,i}}{\partial t} + \frac{\partial u_{l,i}u_{l,j}}{\partial x_j}) = -\frac{p_l}{\partial x_i} + \mu_l \frac{\partial^2 u_{l,i}}{\partial x_j \partial x_j}, \quad \frac{\partial u_{l,j}}{\partial x_j} = 0, \quad \text{if} \quad \vec{x} \in \Omega_l(t) \tag{2.16}$$

$$\rho_g(\frac{\partial u_{g,i}}{\partial t} + \frac{\partial u_{g,i}u_{g,j}}{\partial x_j}) = -\frac{p_g}{\partial x_i} + \mu_g \frac{\partial^2 u_{g,i}}{\partial x_j \partial x_j}, \quad \frac{\partial u_{g,j}}{\partial x_j} = 0, \quad \text{if} \quad \vec{x} \in \Omega_g(t) \tag{2.17}$$

$$(u_{g,i} - u_{l,i})n_i = 0, \qquad \text{if} \quad \vec{x} \in \Sigma(t) \tag{2.18}$$

$$(2\mu_l S_{ij}^{(l)} - 2\mu_g S_{ij}^{(g)})n_j = (p^{(l)} - p^{(g)})n_i + \sigma k n_i, \qquad \text{if} \quad \vec{x} \in \Sigma(t) \tag{2.19}$$

In (2.16)-(2.17), we neglected the contribution of body forces. Following Peskin (1977), the interface $\Sigma(X(t),t)$ is a smooth function depending on positions $X(t)$ of material points ("markers"), which are located on the interface. These particles are tracked by Eulerian velocity at the position of interface. For the m-th sample point on the interface, it writes:

$$\frac{d\vec{X}_m}{dt} = \vec{u}(\vec{X}_m,t) = \int_{\vec{x}\in\Omega} \vec{u}(\vec{x},t)\delta(\vec{x} - \vec{X}_m)d\vec{x} \tag{2.20}$$

Identification of free interface by tracking of massless Lagrangian particles stands from the pioneer work "Markers and Cells" by Harlow & Welch (1965). In this approach, the fluid domain is populated by particles which are tracking by Eulerian velocity field. To maintain the uniform distribution of such particles along with evolution of the flow represents a nontrivial task. To this end, Daly

& Pracht. (1967) used particles only on the free boundary. This procedure was strongly advanced by Tryggvason & Unverdi (1992) for the case of 3D flow.

When interfaces merge or breakup, the tracking procedure becomes complicated. The Level Set Formulation avoids this problem. Before its description, we rewrite (2.16)-(2.17) in the integral form (Smereka, 2003):

$$\int_{\Omega=\Omega_1+\Omega_2} \rho(\frac{\partial u_i}{\partial t} + \frac{\partial u_i u_j}{\partial x_j})d\vec{x} = \int_{\partial\Omega} \sigma_{ij} n'_j dS - \int_{\Sigma(X(t),t)} (\sigma^l_{ij} - \sigma^g_{ij}) n_j d\Sigma \quad (2.21)$$

where $\partial\Omega$ denotes the overall boundary of domain Ω, n'_j are components of the outwards to $\partial\Omega$ normal vector, and the following definitions are used respectively for components of velocity and stress tensor, as well as for density and viscosity:

$$u_i = \begin{cases} u_{g,i}, & \text{if} \quad \vec{x} \in \Omega_g \\ u_{l,i}, & \text{if} \quad \vec{x} \in \Omega_l \end{cases} \quad (2.22)$$

$$\sigma_{ij} = \begin{cases} \sigma_{g,ij}, & \text{if} \quad \vec{x} \in \Omega_g \\ \sigma_{l,ij}, & \text{if} \quad \vec{x} \in \Omega_l \end{cases} \quad (2.23)$$

$$\rho = \begin{cases} \rho_g, & \text{if} \quad \vec{x} \in \Omega_g \\ \rho_l, & \text{if} \quad \vec{x} \in \Omega_l \end{cases} \quad (2.24)$$

$$\mu = \begin{cases} \mu_g, & \text{if} \quad \vec{x} \in \Omega_g \\ \mu_l, & \text{if} \quad \vec{x} \in \Omega_l \end{cases} \quad (2.25)$$

Using the divergence theorem, and accounting for (2.7), equation (2.21) takes the following integral form:

$$\int_{\Omega=\Omega_1+\Omega_2} \rho(\frac{\partial u_i}{\partial t} + \frac{\partial u_i u_j}{\partial x_j})d\vec{x} = \int_{\Omega=\Omega_1+\Omega_2} \frac{\partial \sigma_{ij}}{\partial x_j} d\vec{x} - \int_{\Sigma(X(t),t)} \sigma k n_i d\Sigma \quad (2.26)$$

The advantage of (2.12) and (2.26) is that the boundary condition at interface is included into equation of motion; while, again, the difficulty is related to necessity of tracking procedure for definition of interface topology.

2.2.2 Level Set Formulation

In the Level Set Approach (Smereka, 2003; Sussman, 1994; Sussman *et al.*, 1994; Sussman *et al.*, 1996; Sussman & Smereka, 1997 and Osher & Sethian, 1988) a specific scalar field $\phi(\vec{x},t)$ (Fig.2.2) is introduced in order to attribute interface to the iso-surface of presumed scalar value (say zero, as in Fig.2.2):

$$\Sigma(t,\vec{x}|_{\phi(\vec{x},t)=0}) \tag{2.27}$$

The outwards normal to the interface is defined by

$$\vec{n} = \left.\frac{\nabla\phi}{|\nabla\phi|}\right|_{\phi=0} \tag{2.28}$$

Its link to curvature (2.10) is

$$k(\phi) = \nabla\cdot\vec{n} = \nabla\cdot\left.\frac{\nabla\phi}{|\nabla\phi|}\right|_{\phi=0} \tag{2.29}$$

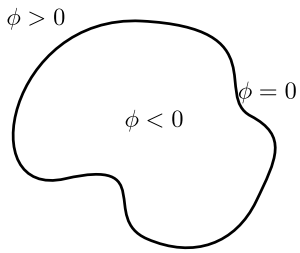

Figure 2.2: An illustration of the level set function in two-phase flow.

The scalar field $\phi(\vec{x},t)$ is governed by the following transport equation:

$$\frac{\partial\phi(\vec{x},t)}{\partial t} = -u_j\frac{\partial\phi}{\partial x_j} \tag{2.30}$$

By definition of the area element $d\Sigma = |\nabla\phi|\delta(\phi)d\vec{x}$, and using the property of the Dirac delta function (Landau & Lifshitz, 1975), equation (2.26) takes the following local form:

$$\rho(\frac{\partial u_i}{\partial t} + \frac{\partial u_i u_j}{\partial x_j}) = \frac{\partial\sigma_{ij}}{\partial x_j} - \sigma k\delta(d)n_i \tag{2.31}$$

where $\delta(d) = |\nabla\phi|\delta(\phi)$, and d is the normal distance to the interface. So far the interface (2.29) can be captured from (2.30), (2.31) instead of the tracking procedure.

The recent developments of the Level Set Formulation and its applications to modeling primary atomization, performed in scientific groups of Alain Berlemont (CORIA laboratory) and Jean-Luc ESTIVALEZES (ONERA Toulouse) (Tanguy, 2004; Ménard *et al.*, 2007; Trontin, 2009; Couderc, 2007), as well as in CTR of the Stanford University, Herrmann & Gorokhovski (2008) and Desjardins & Pitsch (2009) showed that Level Set Approach may help in describing the physics of primary atomization. The close look on the dynamics of a filament, on a drop formation and coalescence, on evolution of primary instability, allows to describe the mechanism involved in the process. An example from Desjardins & Pitsch (2009) of interface simulated under air-blast atomization, is illustrated in Figure 2.3. For comparison, the experimental visualization of Rayana (2007) is given on the right-hand side of this Figure 2.3. In computation, the properties of both fluids, including the surface tension coefficient, are those of water and air, with the exception that the water density has been reduced to $\rho = 50kg/m^3$ in order to ensure numerical stability. As in the experiment, the momentum flux ratio is set to $M = 16$, with a bulk air velocity of $U_g = 20m/s$ and a bulk water velocity of $U_l = 0.7746m/s$, for a height of the water layer of $10cm$. It is seen that in accordance with experimental observations the simulation predicts also the initial Kelvin-Helmholtz instability, resulting in ligament formation.

However, when the Weber number is very large, the computational expense associated with the resolution of all length scales is very high, and practical application of Level Set type approaches to whole primary atomization process is limited. There are also two fundamental problems which are needed to be solved. The first one concerns the mass conservation at the breakage, since, in principal, the last one takes place on unresolved scales, and after many breakups, a significant liquid mass deficiency may appear. The second problem is numerical. In general case, the norm of scalar gradient $|\nabla\phi|$ is continuously growing. This makes difficult to handle equation (2.30) numerically in such a way that the velocity field from Navier-Stokes equations remains not affected.

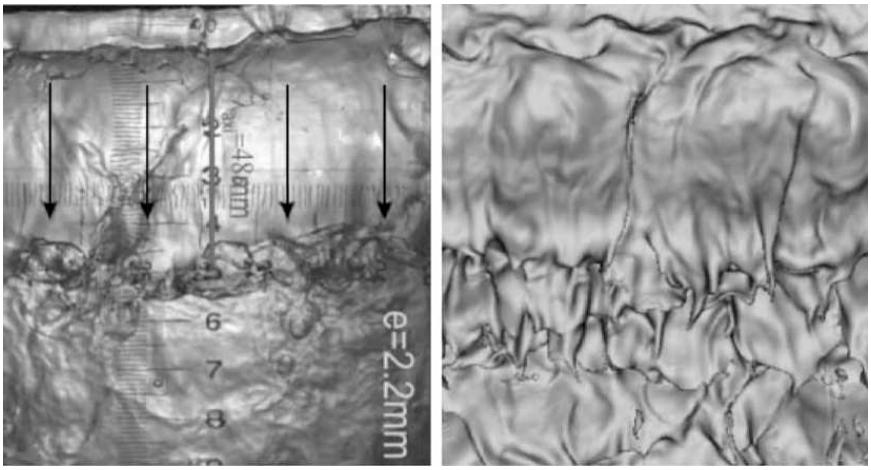

Figure 2.3: Top view of the phase-interface in the shear layer flow. Flow direction is from top to bottom; on the LHS: experimental visualization of Rayana (2007); on the RHS: simulation by Desjardins & Pitsch (2009) using Level Set Approach.

2.2.3 Volume of Fluid (VOF) Formulation

The volume of fluid method (VOF) was first introduced by Hirt & Nichols (1981) for incompressible two-phase flows. In the VOF method, a single set of momentum equations is shared by the fluids, and the volume fraction of each of the fluids $\Phi(\Omega, t)$ is tracked throughout the domain, where Ω represents a computational cell and t is time. Mixed cells will have a volume fraction Φ between 0 and 1 and cells without interfaces (pure cells) will have a volume fraction equal to 0 or 1. Figure 2.4 shows a typical volume fraction distribution.

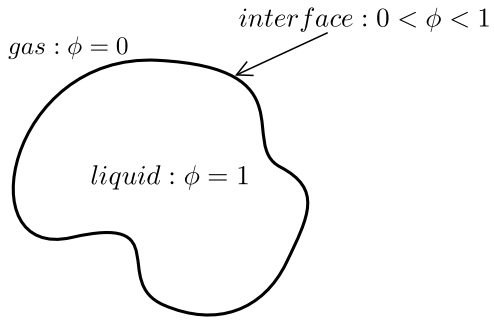

Figure 2.4: An illustration of the volume fraction function in two-phase flow.

Similar to the level set function, the transport equation for volume fraction

function is given by

$$\frac{\partial \Phi}{\partial t} + \frac{\partial u_j \Phi}{\partial x_j} = 0 \tag{2.32}$$

The density and viscosity of the gas-liquid two-phase flow are considered as functions of the liquid volume fraction, and densities and viscosities of both phases (De Villiers *et al.*, 2004; Gueyffier *et al.*, 1999; Gao *et al.*, 2003), given by

$$\rho = \Phi \rho_l + (1 - \Phi)\rho_g \tag{2.33}$$

$$\mu = \Phi \mu_l + (1 - \Phi)\mu_g \tag{2.34}$$

One major advantage of representing a free surface using volume fractions is the fact that accurate algorithms for advecting the volume fraction function can be developed so that mass is conserved while still maintaining a sharp representation of the interface (Sussman & Puckett, 2000). However, a disadvantage of the VOF method is that it is difficult to compute accurate local normal vectors and curvatures from volume fractions, because the spatial derivatives of volume fraction function transition sharply in the neighborhood of the free surfaces. The standard VOF method calculates the curvature by first modifying the volume fractions in a special way. However, as Sussman noted, if one does not introduce sufficient smoothing, the curvature of the surface will be highly oscillatory. If one smoothes too much then the numerical algorithm smears curvature changes on the free surface and this has the effect of making the curvature constant.

2.3 Phenomenological Models

The objective of phenomenological models is to represent the essential features of spray formation, without consuming much of CPU time and memory. The first category of phenomenological models comprises the conventional Lagrangian models, which are widely-used in industrial numerical codes during last thirty years.

2.3.1 Drops Population models

In these models, along with integration of governing equations for the gaseous phases, the round proliferating blobs (initially, of the nozzle exit diameter) are injected into computational domain, and are tracked with exchange of mass, momentum, and energy between the spray and the gas. The gas flow is computed either by RANS or by LES approaches. These numerical models have been successful because they are computationally efficient and at the same time provide reasonable agreements with experimental measurements, mostly in terms of penetration and spray angle, and in limited cases, also in terms of drop size, number density and their distributions. In these models, the presumed mechanisms of the initial breakup of the liquid jet - surface instabilities (Beale & Reitz, 1999; Habchi & Baritaud, 1997; Reitz, 1987; Patterson & Reitz, 1998), drop shedding (Yi & Reitz, 2004), spontaneous breakup (Tanner, 2004), jet turbulence (Huh & Gosman, 1991), cavitation (Arcoumanis *et al.*, 1997; Arcoumanis & Gavaises, 1998; Kong *et al.*, 1999) - are used in breakup of each tracking sphere. In practical conditions (high Weber or Reynolds numbers), each breakage is characterized by infinite number of degrees of freedom, in such a way that resulting size of each produced droplets may be predicted only at a certain probability. To this end, in Gorokhovski (2001), it is proposed to simulate breakup in the framework of the stochastic scenario. The "lack of memory" stochastic process was proposed, which at large rate of spray formation leads to exponential distribution of drops radius; this distribution was confirmed in measurements. Later on, in Gorokhovski & Saveliev (2003) with coupling to RANS approach in the gas flow, and in Apte *et al.* (2003) with coupling to LES approach in the gas flow, the authors incorporated another stochastic process which was focused on statistical universalities of breakup under scaling symmetry. The parameters of those implemented stochastic processes stem from presumed physical mechanism of breakup. Example of blobs distribution from Apte *et al.* (2003) is given in Figure 2.5.

Although the conventional models may predict the global parameters of spray in practical conditions, and although these models do not require significant CPU time and memory, as it is the case in DNS-type simulation, the liquid flow in these models is mimicked by motion of round spheres. Closely to injector (red frame

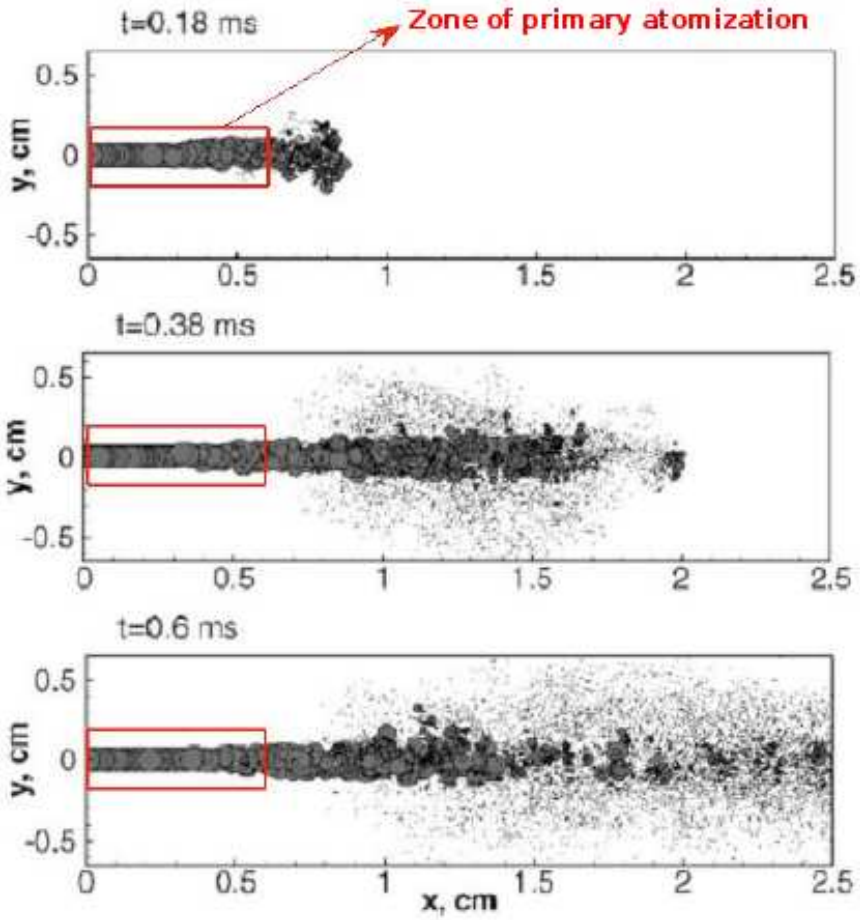

Figure 2.5: Time evolution of spray in a nitrogen-filled closed cylindrical chamber (Apte *et al.*, 2003).

in Fig.2.5), such a statistical representation of liquid flow oversimplifies its real complex dynamics and interactions with gas.

2.3.2 Eulerian Mixing model

Consider a high Reynolds (or Weber) number flow of two incompressible and randomly interacting media. In this practical case, the definition of instantaneous interface becomes a difficult task. One of the ways was proposed by Vallet *et al.* (2001): primary atomization is described in the framework of a single "fluid", as turbulent mixing of a high-density jet with ambient gases. This was formalized in lines of RANS approach as follows. Without surface tension effects, the instantaneous equations of two-fluids flow is:

$$\rho(\frac{\partial u_i}{\partial t} + \frac{\partial u_i u_j}{\partial x_j}) = \frac{\partial \sigma_{ij}}{\partial x_j} \tag{2.35}$$

$$\frac{\partial \rho}{\partial t} + \frac{\partial \rho u_j}{\partial x_j} = 0 \tag{2.36}$$

From these equations, the ensemble-averaged equations can be generated by the techniques, which were set down for suspensions and porous media in Saffman (1971), Ludgren (1972), Joseph & Lundgren (1990). Introducing an indicator function

$$Y(\vec{x}) = \begin{cases} 0 & \text{if} \quad \vec{x} \in \Omega_g \\ 1 & \text{if} \quad \vec{x} \in \Omega_l \end{cases} \tag{2.37}$$

the ensemble-averaged equations are:

$$\frac{\partial \overline{\rho}\tilde{Y}}{\partial t} + \frac{\partial \overline{\rho}\tilde{Y}\tilde{u}_j}{\partial x_j} = -\frac{\partial \overline{\rho Y'' u_j''}}{\partial x_j} \tag{2.38}$$

$$\frac{\partial \overline{\rho}\tilde{u}_i}{\partial t} + \frac{\partial \overline{\rho}\tilde{u}_i\tilde{u}_j}{\partial x_j} = -\frac{\partial \overline{\rho u_i'' u_j''}}{\partial x_j} + \frac{\partial \overline{\sigma}_{ij}}{\partial x_j} \tag{2.39}$$

$$\frac{\partial \overline{\rho}}{\partial t} + \frac{\partial \overline{\rho}\tilde{u}_j}{\partial x_j} = 0 \tag{2.40}$$

where $\tilde{Y}$ is the local averaged mass fraction of the liquid, Y'' denotes the fluctuation about $\tilde{Y}$, $\overline{\rho}$ is the local mean density in two-fluid flow, $\tilde{u}_i$ is the $i-th$ component of the local mass-averaged velocity in two-fluid flow, and u_i'' denotes the fluctuation about $\tilde{u}_i$. The gradient-type closure for dispersion of liquid is used $\overline{\rho Y'' u_j''}$ (Vallet *et al.*, 2001). By using the techniques of algebraic stress modeling (Rodi, 1976), the expressions for the Reynolds stress tensor $\overline{\rho u_i'' u_j''}$, with contribution of pressure-gradient drift fluxes due to the high density variation $\overline{u_j''}\frac{\partial \overline{P}}{\partial x_i}$ and $\overline{Y''}\frac{\partial \overline{P}}{\partial x_i}$, are proposed (see also Baev *et al.*, 1987).

Additionally to (2.38)-(2.40), the scalar field $\overline{\Sigma}$, presenting the mean amount of interfacial surface per unit volume, was introduced in this approach. The knowledge of local $\overline{\Sigma}$ is thought to estimate the mean radius of droplets $r = 3\overline{\rho}\tilde{Y}/\rho_l\overline{\Sigma}$ at the given location. The universal form of transport equation of $\overline{\Sigma}$ is presumed with terms of its mean convection, gradient-type diffusion, production (stretching) and destruction (coalescence):

$$\frac{\partial \overline{\Sigma}}{\partial t} + \frac{\partial \tilde{u}_j \overline{\Sigma}}{\partial x_j} = \frac{\partial}{\partial x_j}(D_\Sigma \frac{\partial \overline{\Sigma}}{\partial x_j}) + \frac{1}{\tau_{prod}}\overline{\Sigma} - \frac{1}{\tau_{destr}}\overline{\Sigma}^2 \tag{2.41}$$

The production of $\overline{\Sigma}$ is addressed to the turbulent stretching; expressions of turbulent time scale are used. In equilibrium, when turbulent stretching is balanced by capillary forces, i.e. the critical Weber number is of order of unity, it follows from (2.41) that further, in terms of the maximum stable radius r_{eq}: $\frac{1}{\tau_{destr}} = \frac{\rho_l r_{eq}}{3\tau_{prod}\overline{\rho}\tilde{Y}}$. The model (2.38)-(2.41) naturally lends itself to the RANS codes which are in widespread use. The potentials of this approach were shown in CORIA laboratory, in the scientific group of F.X. Demoulin (Beau, 2006; and Lebas, 2007). In Wei (2007), it was mentioned that additional corrections were needed for new constants in the proposed in Vallet *et al.* (2001) modifications into the turbulence model. Despite a general reserve that the transport of $\overline{\Sigma}$ is modelled in (2.24)-(2.25) by diffusion-like hypothesis; neglecting thereby the spatial grouping effects of liquid elements, the Eulerian Mixing Approach was successfully used in simulation of spray combustion in rocket-like conditions (Jay *et al.*, 2006). This is illustrated in Figure 2.6, in which the experimental visualisation of OH emissions from Juniper *et al.* (2001) is compared with results of RANS computations

of local combustion rate. Numerical results of computation of spray were not reported in this study.

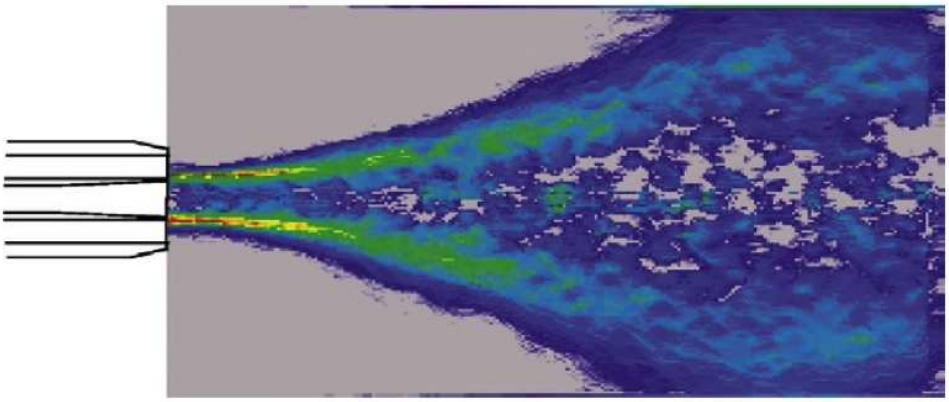

(a)

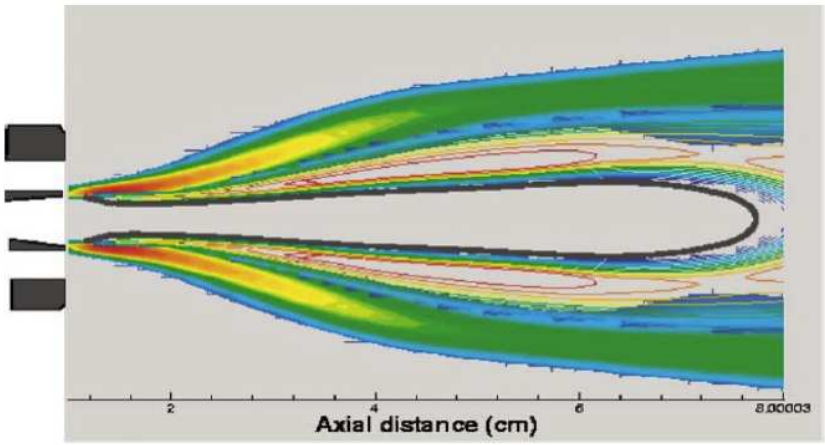

(b)

Figure 2.6: On the top: Mean light intensity radiated by OH-radicals in the experimental flame (Juniper *et al.*, 2001); On the bottom: Calculated in (Jay *et al.*, 2006) mean reaction rate plotted on the same scale of colors. Isocontours of gaseous oxygen in the range $[0.5, 0.8]$ with an increment of 0.05 and isocontour of liquid oxygen mass fraction $\tilde{Y}_l = 0.5$ (thickened line). The plots are restricted to the initial $7cm$.

2.3.3 Fragmentation Model and new proposal

Introduction

For introduction to this approach, let us start with the picture of slow crack propagation in a sheet of paper (Måløy *et al.*, 2006). A very complex fracturing, with burst-like events, is seen over a broad range of individual cracks. In the vicinity of each rupture, one can find as a small one as far as a big one. The question is can we predict this deterministically? The answer is "probably no", it is a too difficult task. Due to interactions between multiple micro defects, each crack is characterized by a huge number of degrees of freedom. Then it is natural to abstract the essential features of this fracturing, and to model it as simple as possible (situation is similar to turbulence at a high Reynolds number).

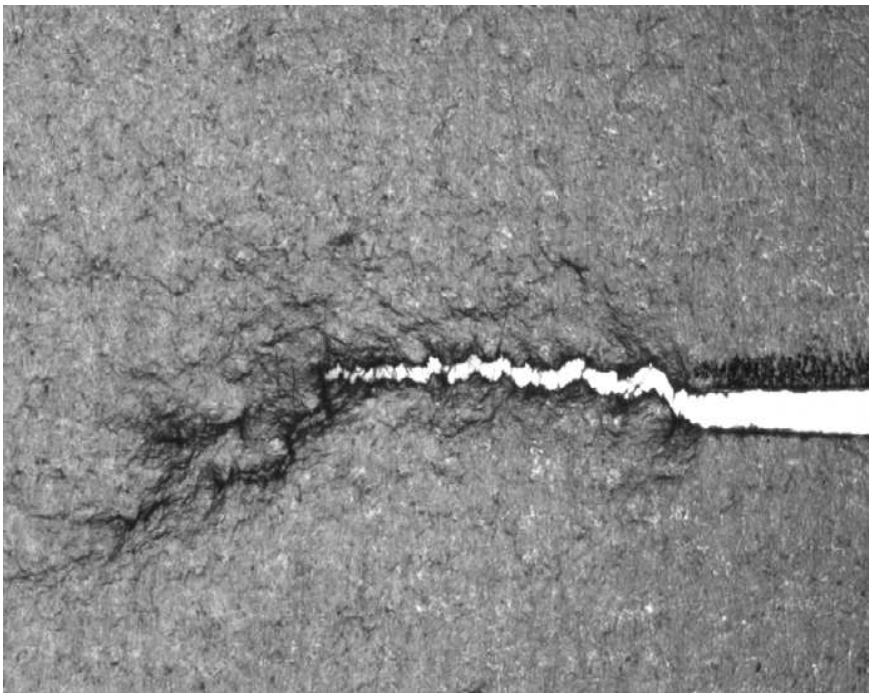

Figure 2.7: Instaneous picture of slow crack propagation in a sheet of paper (Bonamy *et al.*, 2008).

We think of experiment, in which we start at the same strain rate, wait the same time in each trial, and record the length of appearing fingers. The question raised is what is the probability to get a finger in between $[r, r + \Delta r]$, and what

is the evolution of this probability with increasing "time" ? In fact, these questions define the simplest ("naive") view on fragmentation: the fragmentation is viewed as stochastic process with breaking, or splitting of a material into smaller fragments (Sornette, 2000). This domain of modern physics plays an important role in the study of a variety of physical, chemical, and geological processes, including solid particle decomposition, network branching, materials degradation such as fiber composites, rocks, concrete, polymers which are subject to an external load or compression. A dramatic example is the aging of present aircrafts due to repeated loading in a corrosive environment. Examples of fragmentation also include turbulence and atomization. The common property shared by those examples is that each rupture is produced by a collective result of involved in long-range forces. Higher the global parameter of fragmentation (shear rate for the case of the crack propagation in paper) is, and weaker properties of a material to resist to fragmentation are, then broader the spectrum of ruptures which can be eventually produced at each location is.

In nature, the fragmentation emerges in relation with others physical processes: flowing and elastic response. The next picture represents the air-blast atomization (Lasheras *et al.*, 1998) of liquid jet surrounded by a high-speed coaxial gas flow. Specifically for (d)-(h), it is seen that number of degrees of freedom for each filament production is huge, and that the zone of primary atomization is characterized by a complex network of threads, which can persist in the close vicinity to the liquid bulk. Can DNS represent statistically such a complexity of whole spray formation? Simulations in the future will answer.

However when the Weber number is high enough, the frequency of formation of liquid branches and ligaments is relatively high. Then it is natural to introduce an essential mechanism of breakup, as a global controlling parameter, and to model this atomization stochastically by the following scenario: the issuing liquid jet is subject to fragmentation under load of the momentum difference in the liquid and the gas; the zone of primary atomization is viewed as zone of fragmentation (Figure 2.9).

The approach proposed here is very simplified. We consider a flowing turbulent connected media with an immersed composite body in the close vicinity of air-blast atomizer. This immersed body is bordered by fragmentation zone, and

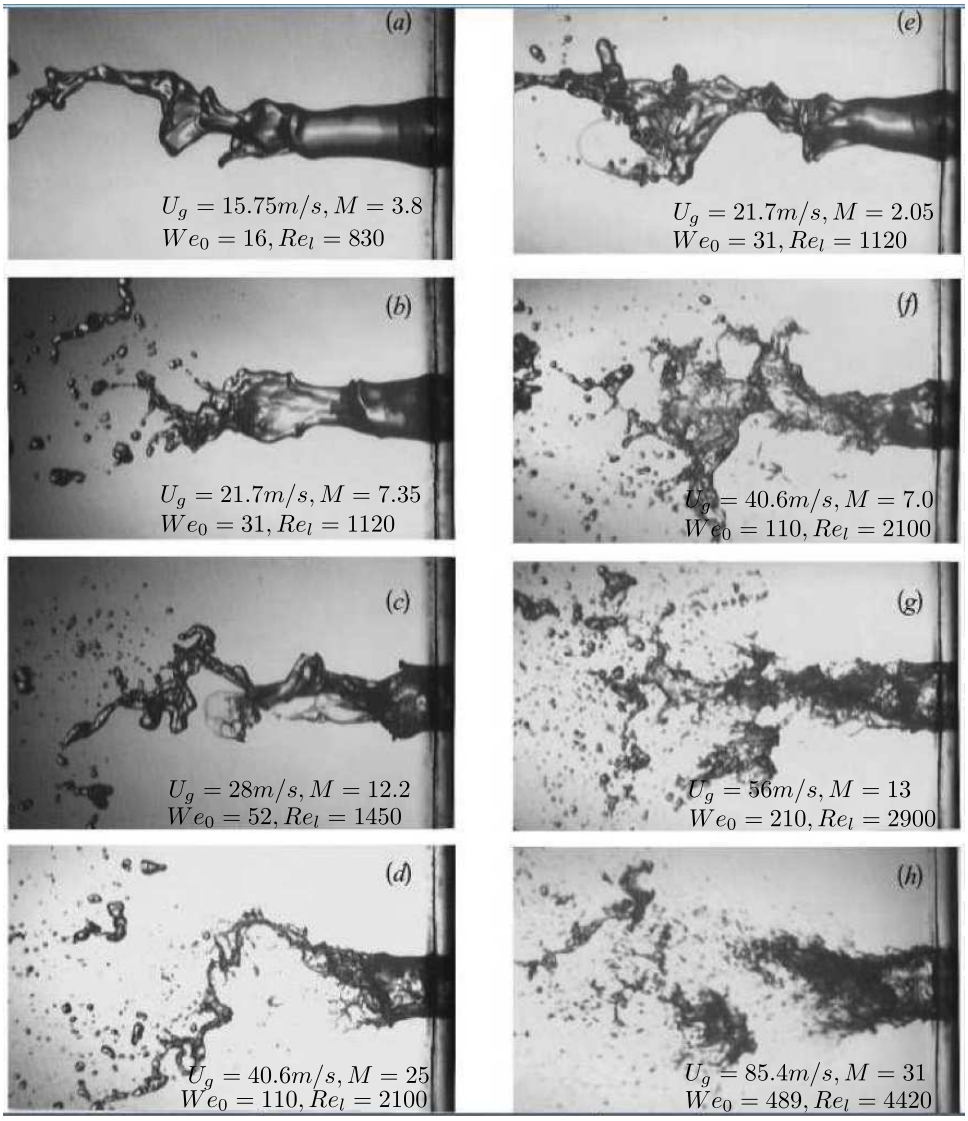

Figure 2.8: Instantaneous photos of air-blast atomization in the liquid jet surrounded by a high-speed coaxial gas flow. Photos correspond to different inlet velocities for the gas and the liquid flow (Lasheras *et al.*, 1998).

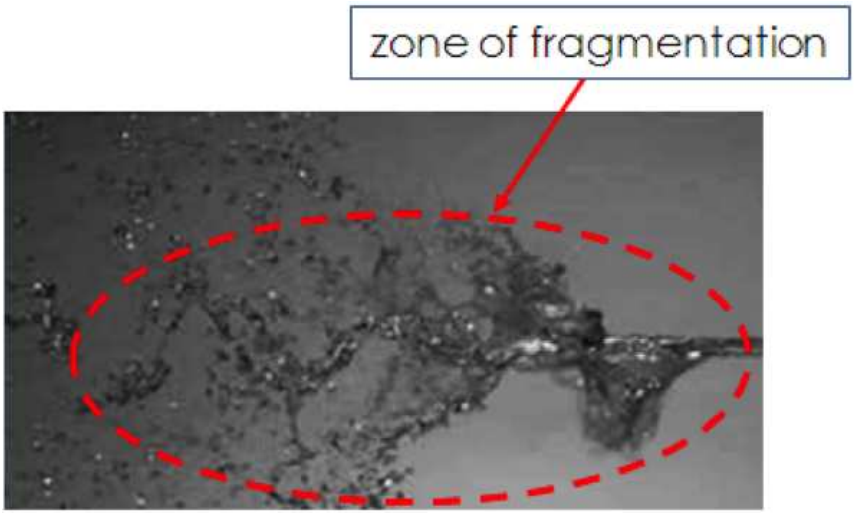

Figure 2.9: A plane liquid jet surrounded by a high-speed gas-flow. Images from ONERA (Trontin, 2009).

contains the connected (continuous) phase, and the not connected (dispersed) phase. In the composite immersed body, two processes are assumed to be fast comparing to the large (resolved) turbulent time-scale: it is the frequency of filament network formation, and the frequency of collisions between detached liquid elements. Another physical assumption is that the local acceleration in the immersed composite body is controlled by its value on the interface. Then the connected phase is assumed to be governed by the following filtered equations:

$$\frac{\partial \langle u_i \rangle}{\partial t} = \begin{cases} -\frac{\partial \langle u_i u_j \rangle}{\partial x_j} + \frac{1}{\rho_g} \frac{\partial \langle \sigma_{ij} \rangle}{\partial x_j}, & \text{if} \quad P_l = 0 \\ P_l \dot{U}_S n_i, & \text{if} \quad \vec{x} \in \Omega_l \end{cases} \tag{2.42}$$

where brackets $\langle ... \rangle$ denote filtering in terms of LES approach, thereby $\langle u_i \rangle$ denotes the filtered velocity component, $P_l(\vec{x}, t)$ is the probability to find the liquid at the given point, $\dot{U}_S(\vec{x}, t)$ is the acceleration value on the interface, and $n_i(\vec{x}, t)$ is the component of unit vector of orientation. Three variables, $P_l(\vec{x}, t)$, $\dot{U}_S(\vec{x}, t)$ and $n_i(\vec{x}, t)$ need to be modeled. The probability $P_l(\vec{x}, t)$ is simulated in lines of statistical universalities of fragmentation under scaling symmetry (Gorokhovski & Saveliev, 2008), and is similar to approach proposed in Gorokhovski *et al.* (2009). The surface orientation $n_i(\vec{x}, t)$ is simulated in the framework of the stochastic

relaxation towards isotropy in the down-stream direction (Gorokhovski *et al.*, 2011). This is done by using the unit sphere on which the Brownian motion is simulated. The expression for $\dot{U}_S(\vec{x},t)$ is based on the increment of the interface convection velocity. The description and assessment of all those stochastic models proposed is given in the next Chapter 3.

In fact, equation (2.42) can be written in the following discrete form:

$$\frac{\langle u_i\rangle^{n+1}-\langle u_i\rangle^{n}}{\Delta t}=\langle RHS_i\rangle+\langle F\rangle \tag{2.43}$$

where

$$\langle RHS_i\rangle=-\frac{\partial\langle u_iu_j\rangle}{\partial x_j}+\frac{1}{\rho_g}\frac{\partial\langle\sigma_{ij}\rangle}{\partial x_j} \tag{2.44}$$

and

$$\langle F_i\rangle=\begin{cases}0, & \text{if} \quad P_l=0\\ -\langle RHS_i\rangle+P_l\dot{U}_Sn_i, & \text{if} \quad P_l\neq 0\end{cases} \tag{2.45}$$

Then (2.43) resembles the well-known formulation of the immersed body force method. Here the difference with this method is that the immersed body has spatially random porous structure $P_l(\vec{x},t)$ simulated dynamically with the flow evolution; thereby the velocity of the immersed body is not constant as in the standard method.

The dispersed phase is assumed to be conditioned by $0<P_l(\vec{x},t)<1$, and is described by liquid drops motion averaged over liquid/liquid collisions. Consequently, the drops are tracked by:

$$\frac{d\overline{v_{p,i}}}{dt}=\frac{\langle u_i\rangle-\overline{v_{p,i}}}{\tau_{st}}-\nabla\frac{T_p}{m_p}, \qquad \text{if} \quad P_l\neq 0 \tag{2.46}$$

where $\overline{v}_p$ is the drops velocity averaged over its collisions, T_p is the statistical temperature of these collisions, and τ_{st} is the Stokes time. The model for the statistical temperature T_p, as well as the expression for the Stokes time τ_{st} are also given in Chapter 3. Out of the immersed body the drop tracking equation takes the usual form:

$$\frac{dv_{p,i}}{dt} = \frac{\langle u_i \rangle - v_{p,i}}{\tau_{st}}, \qquad \text{if} \quad P_l = 0 \tag{2.47}$$

Assuming that blobs are stripped in the zone $0 < P_l(\vec{x}, t) < 1$, their size can be sampled from the simulated spatial distribution $n_i(\vec{x}, t)$, namely by $(\frac{\partial n_j}{\partial x_j})^{-1}$. However in this manuscript, we just presumed exponential distribution of size of formed blobs, which are subject further to the secondary atomization.

Finally, (2.42) is simulated by standard LES approach with the Smagorinsky closure for the eddy-viscosity. The assessments of our code in LES formulation is given in Chapter 4. The main objective of this thesis is to realize and assess formulations (2.43)-(2.46). The computations against measurements, as well as discussion on obtained numerical results are given in Chapter 5. The manuscript is ended up with Conclusion.

Chapter 3

Stochastic model of spray formation in close vicinity of the air-blast atomizer

As it has been mentioned at the end of 2.3.3, the equations of connected phase including composite immersed body are:

$$\frac{\partial \langle u_i \rangle}{\partial t} = \begin{cases} -\frac{\partial \langle u_i u_j \rangle}{\partial x_j} + \frac{1}{\rho_g}\frac{\partial \langle \sigma_{ij} \rangle}{\partial x_j}, & \text{if} \quad P_l = 0 \\ P_l \dot{U}_S n_i, & \text{if} \quad P_l \neq 0 \end{cases}$$

These equations contain three variables: (i) the probability to find the liquid in the vicinity of injector $P_l(\vec{x}, t)$; (ii) the local magnitude of interface acceleration $\dot{U}_S(\vec{x}, t)$; (iii) its stochastic direction $n_i(\vec{x}, t)$; these variables need to be modeled; two different stochastic processes defining $P_l(\vec{x}, t)$ and $n_i(\vec{x}, t)$ are supposed to be independent. This is done by stochastic simulation described hereafter in Sections 3.1-3.3.

Section 3.4 is devoted to formulation of dispersed (non-connected) phase in the composite immersed body. The equations for this phase are:

$$\frac{d\overline{v_{p,i}}}{dt} = \frac{\langle u_i \rangle - \overline{v_{p,i}}}{\tau_{st}} - \frac{\partial}{\partial x_i}\left(\frac{T_p}{m_p}\right)$$

in which $\overline{v_{p,i}}$ is component of the liquid drop velocity averaged over inter-drop collisions; T_p is the statistical temperature due to collisions (activated only in sub-

region $0 < P_l < 1$), and τ_{st} is the expression of the Stokes time. The structure of Section 3.4 is as follows. First, the primary formation of dispersed phase is given in Section 3.4.1: (i) position of primary blob in sub-region $0 < P_l < 1$; (ii) its size; and (iii) its initial direction. The latter is prescribed on the basis of obtained distribution $n_i(\vec{x}, t)$. Then discussion on (2.46), on statistical temperature T_p and on modified expression of the Stokes time are given in Sections 3.4.2 and 3.4.3, respectively.

All those models constitute the stochastic model of spray formation in close vicinity of the air-blast atomizer, which is coupled with LES in Chapter 4 in the framework of the immersed body force approach.

3.1 Stochastic simulation of liquid distribution P_l

3.1.1 Statistical universalities of fragmentation under scaling symmetry; case of the constant breakup frequency

It has long been observed that in a large variety of physical phenomena, where self-similar processes take place, the logarithms of dynamical variables are normally distributed. This holds for example for grain sizes in crust fragmentation (Razumovsky, 1940, Lomnitz, 1994). The theoretical explanation of the appearance of the log-normal distribution in nature was first given by Kolmogorov (1941). A simplified explanation is as follows. Suppose that we have a big rock which crumbles into sand. If the environmental stresses are the same whatever the size of the rock, the probability that a given piece of rock is fragmented into m_i smaller rocks is independent of the stage of the fragmentation process. Therefore if we start out with a single rock ($m_0 = 1$), in the next stage we have m_1 smaller rocks, in the next stage each of these smaller rocks is fragmented into m_2 still-smaller, and so on. As m_i are independent random variables, the number of grains at the $l \sim th$ stage of fragmentation must be:

$$\ln N_l = \sum_{i=1}^{l} \ln m_i \tag{3.1}$$

Applying the central limit theorem, we have the normally distributed logarithms. The grain sizes are inversely proportional to the number of grains N_l. Hence the distribution of grain sizes with growing number of breakup events obtains the log-normal shape:

$$f(r) = \frac{1}{r\sqrt{2\pi\sigma^2}} e^{-\frac{(\ln r - \langle \ln r \rangle)^2}{2\sigma^2}} \tag{3.2}$$

where $r = \frac{r_k}{r_0}$, $\sigma^2 = \langle \ln^2 r \rangle - \langle \ln r \rangle^2$ and r_0 is the reference scale.

For the following, it is necessary to note that in terms of scaling formulation, Kolmogorov's scenario states that each stage of break-up event reduces the typical length of fragments,$r \Rightarrow \alpha r$, by an independent random multiplier α, $0 \leq \alpha \leq 1$. This process is referred to as fragmentation under scaling symmetry.

From one part, it is known that the central limit theorem requires finite second moment when the number of realizations is infinite. From another part, it is also known that the growing number of breakup events characterizes the discrete model, although numerical schemes analysis shows that the continuous evolution in time and the finite difference (discrete) one can give a significant difference in the solution. An alternative to Kolmogorov's discrete stochastic process is described in Gorokhovski & Saveliev (2003) and Gorokhovski & Saveliev (2008). In these papers, the analytical solution of the evolution equation for the size distribution is analyzed at large times (i.e. high frequency of fragmentation) without appealing to the central limit theorem. Briefly, their results are as follows. In fragmentation under scaling symmetry, the kinetic evolution equation for the normalized distribution function of size, $f(r,t)$,$\int_0^\infty f(r)dr$, is

$$\frac{\partial f(r)}{\partial t} = \nu \int_0^1 \frac{1}{\alpha} f(\frac{r}{\alpha}) q(\alpha) d\alpha - \nu f \tag{3.3}$$

where $q(\alpha)$ is the probability that the radius of product fragment occurs within the interval $[\alpha r_1, (\alpha + d\alpha) r_1]$ ($\int_0^1 q(\alpha)d\alpha = 1$) and ν is the breakup frequency assumed here to be constant. In (3.3), the probability $q(\alpha)d\alpha$ is, in principle, unknown function, and since the solution of (3.3) requires knowledge of all moments of $q(\alpha)$,

this equation appears to be useless. However at large times (i.e. high frequency of fragmentation), Gorokhovski & Saveliev (2003) and Gorokhovski & Saveliev (2008) showed that the solution $f(r,t)$ depends solely on the first two logarithmic moments, $\langle \ln \alpha \rangle$ and $\langle \ln^2 \alpha \rangle$, and its expression is:

$$f(r,t) \underset{t\to\infty}{=} \frac{1}{r_0} \frac{1}{\sqrt{2\pi \langle \ln^2 \alpha \rangle \nu t}} \exp(-\frac{\langle \ln \alpha \rangle^2}{2\langle \ln^2 \alpha \rangle} \nu t) \exp[-\frac{(\ln \frac{r}{r_0})^2}{2\langle \ln^2 \alpha \rangle \nu t}] (\frac{r_0}{r})^{1-\frac{\langle \ln \alpha \rangle}{\langle \ln^2 \alpha \rangle}} \tag{3.4}$$

This expression confirms the main result of Kolmogorov (1941) concerning the log-normal asymptotic shape; it is called as the first statistical universality with two parameters: the first and the second logarithmic moments of $q(\alpha)$. Simultaneously, equation (3.4) shows that by further increasing of time, the "log-normal" multiplier in equation (3.4), $exp[-\ln(\frac{r}{r_0})^2/2\langle \ln^2 \alpha \rangle \nu t]$, tends to unity, and the long-time limit particle-size distribution is determined by power law with one universal parameter, $\langle \ln \alpha \rangle / \langle \ln^2 \alpha \rangle$:

$$f(r,t) \underset{t\to\infty}{=} \frac{1}{r_0} \frac{1}{\sqrt{2\pi \langle \ln^2 \alpha \rangle \nu t}} \exp[-\frac{(\ln \frac{r}{r_0})^2}{2\langle \ln^2 \alpha \rangle \nu t}] (\frac{r_0}{r})^{1-\frac{\langle \ln \alpha \rangle}{\langle \ln^2 \alpha \rangle}} \tag{3.5}$$

This shows a stronger universality (fractals) at latest stages of the breakup under scaling symmetry, with a single parameter $\ln \alpha / \ln^2 \alpha$, as the fractal dimension:

$$f(r,t) \underset{t\to\infty}{\sim} (\frac{1}{r})^{1-\frac{\langle \ln \alpha \rangle}{\langle \ln^2 \alpha \rangle}} \tag{3.6}$$

It was also shown that at large times, equation (3.3) reduces exactly to the Fokker-Planck equation:

$$\frac{\partial f(r)}{\partial(\nu t)} = -\langle \ln \alpha \rangle \frac{\partial}{\partial r}(rf) + \frac{\langle \ln^2 \alpha \rangle}{2!} \frac{\partial}{\partial r}[r \frac{\partial}{\partial r}(rf)] \tag{3.7}$$

in which $\ln^2 \alpha / \ln \alpha$ represents a typical length scale proportional to the lower cut-off scale of fragmentation under scaling symmetry:

$$\frac{\langle \ln^2 \alpha \rangle}{\langle \ln \alpha \rangle} = \ln(\frac{r_*}{r_0}) \tag{3.8}$$

This scale should be presumed from the physics of fragmentation, and it plays the role of the global parameter in the stochastic process. In Gorokhovski *et al.* (2009), the following stochastic equation corresponding to (3.7) was derived in the Itô interpretation:

$$\frac{dr}{r} = [\langle \ln \alpha \rangle + \frac{\langle \ln^2 \alpha \rangle}{2}]\nu dt + \sqrt{\frac{\nu \langle \ln^2 \alpha \rangle}{2}} dW(t) \tag{3.9}$$

where $dW(t)$ is the Wiener process and $[dW(t)]^2 = 2dt$.

3.1.2 Method of floating stochastic particles; determination of P_l

This method of simulation of the liquid core simulation was proposed in Gorokhovski *et al.* (2009).

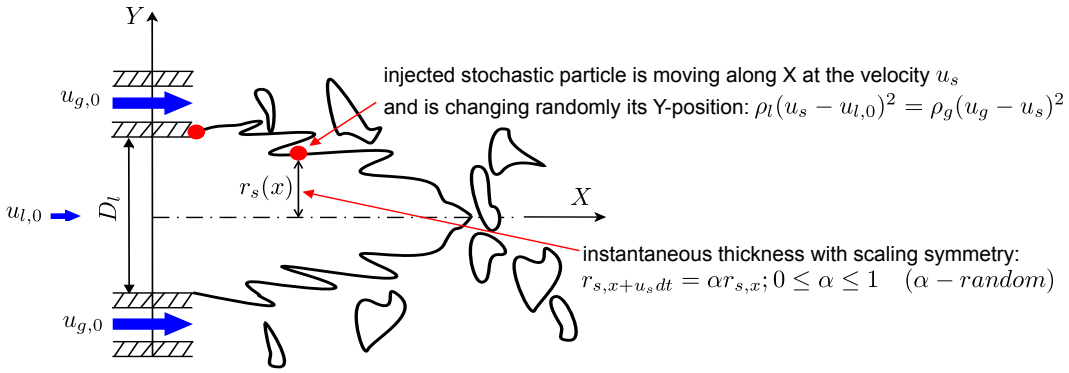

Figure 3.1: Schematic of floating stochastic particles method.

The schematic is presented in Figure 3.1, in which the main assumptions are:

1. At each time, simultaneously with computation of flow in the gas, the liquid non-depleted jet has random geometrical configuration. Each geometrical configuration is determined by spatial trajectory of specific floating stochastic particles with zero mass.

2. At different times, the random configurations of liquid non-depleted jet represent an ensemble of independent realizations in space. The floating

stochastic particles are injected one after another (Figure 3.1); each particle proceeds its own path, which ends up after a length of time referred to as life time of particle. The last one is determined from the dimension analyses. It is assumed that the overall time of the primary air-blast atomization is controlled by three physical values. They include the difference in dynamic pressures in inlet gas and liquid flows, $|\rho_g u_{g,0}^2 - \rho_l u_{l,0}^2|/2$, the inertia of the jet characterized by ρ_l , and the initial diameter of the jet, D_l. The combination of these three values gives:

$$\tau_l^{-1} = \sqrt{\frac{|\rho_g u_{g,0}^2 - \rho_l u_{l,0}^2|}{2\rho_l}} \frac{1}{D_l} = \frac{u_{l,0}}{D_l} \sqrt{\frac{|M-1|}{2}} \tag{3.10}$$

where $u_{g,0}$ is the inlet gas velocity, $u_{l,0}$ is the inlet liquid velocity, and $M = \frac{\rho_g u_{g,0}^2}{\rho_l u_{l,0}^2}$.

After passage of its life time, the stochastic particle is removed from computational domain. The repack procedure is such that rate of particles injection is equal to the rate of their removal.

3. In the down-stream direction x , each stochastic particle is moving with constant axial velocity equal to the convection velocity, given in Introduction.

$$u_s = \frac{\sqrt{\rho_g} u_g + \sqrt{\rho_l} u_l}{\sqrt{\rho_g} + \sqrt{\rho_l}} \tag{3.11}$$

4. Observing vertical ordinates $r_{S,x}$ of a given floating stochastic particle at different axial positions, we assume that $r_{S,x}$ is modified in a step by step manner by a cascade process in which the vertical position $r_{S,x+u_{l,0}\Delta t}$ is produced from the upstream position $r_{S,x}$ by multiplication by a random independent variable α, $0 \leq \alpha \leq 1$:

$$r_{S,x+u_{l,0}\Delta t} = r_{S,x} e^{\ln \alpha} \tag{3.12}$$

Then the stochastic equation (3.9) may be used, which has the following form:

$$\frac{r_{S,x+u_{l,0}\Delta t} - r_{S,x}}{r_{S,x}} = [\langle \ln \alpha \rangle + \frac{\langle \ln^2 \alpha \rangle}{2}]\frac{\Delta t}{\tau_l} + \sqrt{\frac{\langle \ln^2 \alpha \rangle}{2\tau_l}} dW \tag{3.13}$$

with $r_{S,x=0} = D_l/2$.

5. During the particle motion, each position indicates the cell containing the instantaneous interface, separating the liquid non-depleted domain from the gas. This is illustrated in Figure 3.2.

   From ensemble of particles trajectory, the probability of each high of "green" column can be computed. If $\xi(\vec{x}, t)$ is the parametric function characterizing the liquid core interface, then the one-point distribution of the liquid core interface may be characterized by averaged of characteristic function of a small interval $d\xi$ (associated here with size of the mesh cell):

$$P_l(\vec{x}, t) = \langle \delta(\xi(\vec{x}, t) - r_S) d\xi \rangle \tag{3.14}$$

6. The spray around the non-depleted liquid core is assumed to be thin (the droplet around are assumed to be with negligible volume, but with significant mass in comparison to the gas). Thereby the computed distribution $P_l(\vec{x}, t)$ is attributed to all the liquid around the injector, and the position of blobs to be formed in the near-injector region may be sampled from $P_l(\vec{x}, t)$.

3.1.3 Choice of global parameter $\langle \ln^2 \alpha \rangle / \langle \ln \alpha \rangle$; examples of simulation

As it has been described in Chapter 1, the experimental observations in Varga (2002), Hong (2003) and Rayana (2007) suggest the following mechanism. Exiting from the nozzle, the boundary layer interacts with the liquid jet and gives rise to the Kelvin-Helmholtz instability on the free surface (λ_{KH}). Exposed to the gas flow, the crests of produced longitudinal waves are accelerated. This leads to rapid evolution of the Rayleigh-Taylor instability in the transversal direction (λ_{RT}); then the filaments are stripped from the liquid core. Then according to (3.8), it is assumed:

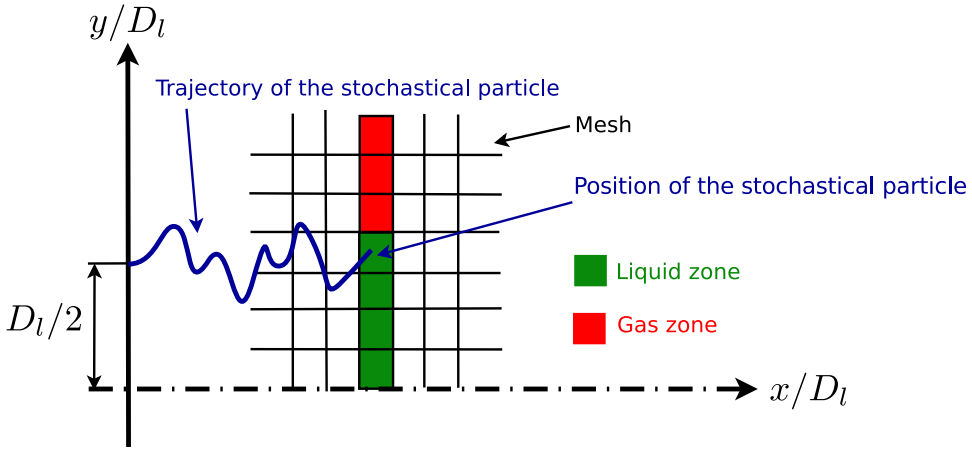

Figure 3.2: Schematic of simulation of the liquid core configuration.

$$\frac{\langle \ln^2 \alpha \rangle}{\langle \ln \alpha \rangle} = \ln(\frac{\lambda_{RT}}{\lambda_{KH}}) \tag{3.15}$$

where expressions for λ_{KH} and λ_{RT} were introduced in Chapter 1. Namely,

$$\lambda_{KH} \approx C_{KH}\sqrt{\frac{\rho_l}{\rho_g}}\delta_g; \quad \delta_g = C_\delta \frac{D_g - D_l}{2\sqrt{Re_g}}; \quad Re_g = \frac{u_{g,0}(D_g - D_l)}{\nu_g}$$

with constants established in experimental studies: $C_{KH} = 2$ and $C_\delta = 5.6$ for plane jet were matched in measurements of (Marmottant, 2001), C_d has an average value 2 in (Varga *et al.*, 2003).

$$\lambda_{RT} = 2\pi(\frac{6C_{KH}}{C_d})^{\frac{1}{2}}(\frac{\rho_l}{\rho_g})^{\frac{1}{4}}\delta_g We_{\delta_g}^{-\frac{1}{2}}(\frac{u_{l,0}}{u_{g,0}})^{\frac{1}{2}}$$

The model (3.13), (3.15) requires one adjustable constant:

$$\langle \ln \alpha \rangle = const \ln(\frac{\lambda_{RT}}{\lambda_{KH}}) \tag{3.16}$$

which was taken equal to 0.03 in Jouanguy (2007), Gorokhovski *et al.* (2009) for all performed computations. This value is also kept in all our computations.

In Chapter 5 of this manuscript, we will compare our simulation with experimental observations of Hong (2003). Examples of sample path of particles according to (3.10), (3.11), (3.13), (3.14), (3.16), with condition from Hong (2003), and $u_{g,0} = 60m/s$, $u_{l,0} = 0.52m/s$, are presented in Figure 3.3.

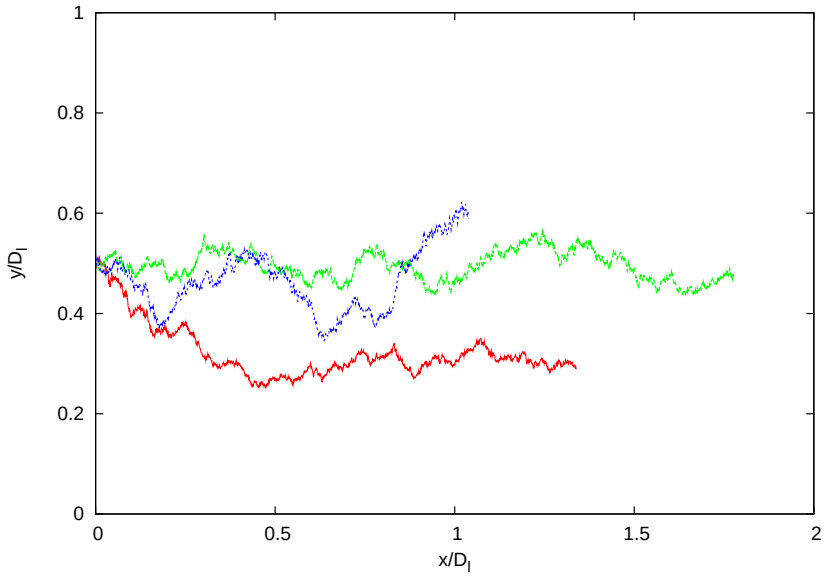

Figure 3.3: Trajectories of different stochastic particles in the condition $u_{g,0} = 60m/s$, $u_{l,0} = 0.52m/s$.

The illustration of distribution of liquid closely to injector P_l, which corresponds to this case ($u_{g,0} = 60m/s$, $u_{l,0} = 0.52m/s$) is given in next figure, Figure 3.4. It is seen that although our simulation is based on very simple ("toy") assumptions, the simulated distribution of liquid closely to injector follows physical intuition.

Demonstration that (3.10), (3.11), (3.13), (3.15) gives also qualitative agreement with others measurements is given in Jouanguy (2007) and Gorokhovski *et al.* (2009). We reproduced their simulation of the liquid core length in Figure 3.5. In the experiment, this length was determined as the length in the downstream direction when the liquid jet rests entirely connected to its injection. In simulation, this length was identified with axial distance from the nozzle where the probability of finding of the non-fragmented liquid is equal to $P_l = 0.95$. It is seen that the stochastic simulation reproduced qualitatively the measurements: with increasing of M , the intact core length is rapidly decreasing, but for $M > 100$, this dependency becomes weak.

We would like to add also to this Section the following remark. In Jouanguy

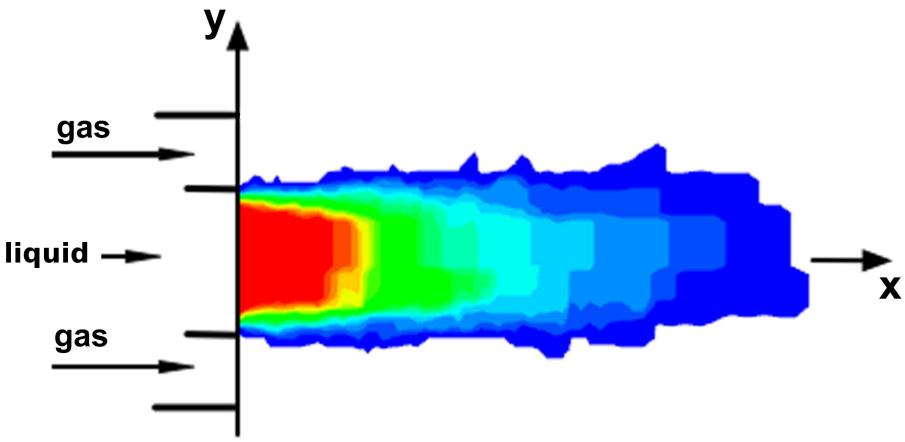

Figure 3.4: Simulation of the liquid distribution closely to injector in the condition $u_{g,0} = 60m/s$, $u_{l,0} = 0.52m/s$ (Hong, 2003).

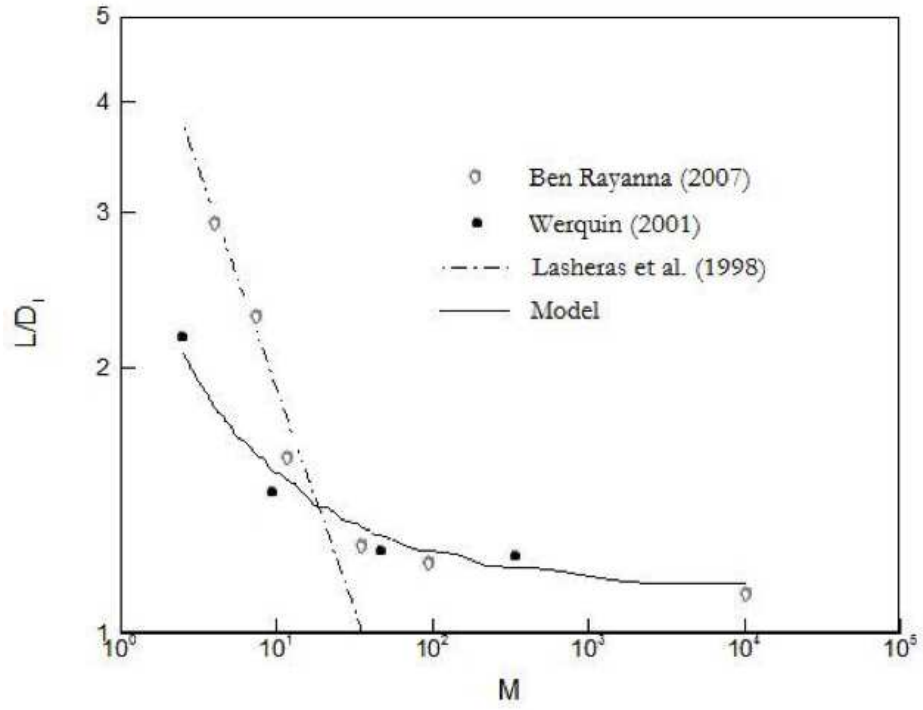

Figure 3.5: Comparison between measured and computed length of the liquid core (Jouanguy, 2007)

(2007) and Gorokhovski *et al.* (2009), the distribution $P_l(\vec{x},t) = \langle \delta(\xi(\vec{x},t) - r_S) d\xi \rangle$ was used in order to change the velocity field computed by LES through $\langle \vec{u}_g | _l \rangle = \vec{u}_g(1 - P_l) + \vec{u}_{l,0} P_l$, and to use the modified velocity field solely for tracking of formed droplets: $\frac{d\vec{u}_d}{dt} = (\langle \vec{u}_g | _l \rangle - \vec{u}_d)/\tau_p$, in which $\vec{u}_d$ is the drops velocity and τ_p is the Stokes time. In the present work, the distribution $P_l(\vec{x},t) = \langle \delta(\xi(\vec{x},t) - r_S) d\xi \rangle$ will be used in definition of immersed body force, in the framework of integration of the filtered Navier-Stokes equations in form of (2.42).

The next step is to simulate the components of local unit normal n_i , which is associated with instantaneous curvature of interface. This direction will be used not only for the immersed body force in the above equation but also for simulation of initial direction of produced blobs; thereby the spray angle may be simulated. The following Section describes simulation of n_i.

3.2 Stochastic model for local outwards normal of interface

To each injected flowing stochastic particle, introduced above in Section 3.1.2, we prescribe the direction. This direction is assumed to be random. Its stochastic behavior is emulated by Brownian random walk on the surface of a unit radius sphere. So far, each flowing stochastic particle is surrounded by unit radius sphere, moving with particle, and characterized by Brownian motion of the unit radius-vector. The physical hypotheses behind this is as follows: the orientation of each flowing particle relaxes stochastically from stream-wise/span-wise alignment (with random azimuth) to full isotropy. In other words, it is assumed that at last stages of the jet depletion, its interface is strongly corrugated, such that its curvature may be approximated by a homogeneous distribution. The diffusion coefficient of such a stochastic relaxation of n_i to isotropy is inversely proportional to the life time of the particle given by (3.10). In realization of this stochastic process, we used the recent work of Zamansky *et al.* (2010).

The schematic representation is given in Figure 3.6. As indicated in this figure, the orientation vector n_i is determined by longitude ϕ and latitude θ:

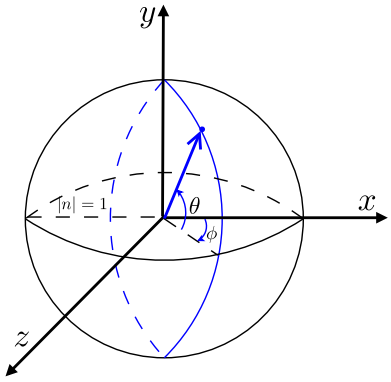

Figure 3.6: Unit sphere on which the Brownian motion is simulated; definition of angles ϕ and θ.

$$n_i = \begin{cases} n_x = \cos(\theta)\cos(\phi) \\ n_y = \sin(\theta) \\ n_z = \cos(\theta)\sin(\phi) \end{cases} \tag{3.17}$$

where $-\pi \leq \phi \leq \pi$ characterizes orientation in the streamwise-spanwise (x, z) plane, and $-\pi/2 \leq \theta \leq \pi/2$ defines orientation relatively to the normal-to-wall direction ($\theta = 0$ and $\theta = \pm\pi/2$ correspond to the direction, which are parallel to the x and y coordinates). The schematic representation is given in Figure 3.6. If ϕ and θ are random, their PDF's corresponding to full isotropy, have the following forms, respectively.

$$P_{isotropic}(\phi) = 1/2\pi \tag{3.18}$$

$$P_{isotropic}(\theta) = \frac{|\cos(\theta)|}{2} \tag{3.19}$$

The mean value for both distributions is zero, and computation of variance yields:

$$< \phi^2 >_{isotropic} = \int_{-\pi}^{\pi} \phi^2 P_{isotropic}(\phi) d\phi = \frac{\pi^2}{3} \tag{3.20}$$

$$< \theta^2 >_{isotropic} = \int_{-\pi/2}^{\pi/2} \theta^2 P_{isotropic}(\theta) d\theta = \frac{\pi^2}{4} - 2 \tag{3.21}$$

Once the unit sphere moves from one point in space to another with the flowing particle, the evolution of the unit vector n_i is defined by the following stochastic process:

$$\begin{cases} \gamma = 2DdW \\ 0 \leq \beta < 2\pi \end{cases} \tag{3.22}$$

where γ is the path length between two successive positions on the sphere and β is the initial direction from one point to another point. β is chosen randomly from the uniform distribution. D is a diffusion coefficient and dW is the standard Wiener process. The rules of this random walk are given by geodesic calculus

$$\begin{cases} \theta_{k+1} = \sin^{-1}(\sin\theta_k \cos\gamma + \cos\theta_k \sin\gamma \cos\beta) \\ \phi_{k+1} = \phi_k + arg(\xi) \\ \Re(\xi) = \sin\beta \sin\gamma \cos\theta_k \\ \Im(\xi) = \cos\gamma - \sin\theta_k \sin\theta_{k+1} \end{cases} \tag{3.23}$$

where θ_k and ϕ_k are two angles corresponding to the node k, and ξ is a complex number, with real and imaginary part $\Re(\xi)$ and $\Im(\xi)$, respectively.

Approaching the life-time along with motion of particle in down-stream, the diffusive equilibrium is attained as a final state, which corresponds to the isotropic PDFs:

$$\begin{cases} P_\theta \rightarrow P_{isotropic}(\theta) \\ P_\phi \rightarrow P_{isotropic}(\phi) \end{cases} \tag{3.24}$$

Figure 3.7 shows one realization of Brownian motion on unit sphere, along with displacement of a floating stochastic particle. The diffusion coefficient D controls the relaxation rate toward isotropy. We compared different diffusion coefficients, as shown in Figures 3.8 and 3.9. It is seen that variance of angles is growing with time (equivalent to growing down-stream position) up to statistically stationary values, which correspond to (3.20) and (3.21). Hereafter in computations, we chose the diffusion coefficient as inversely proportional to the particle life-time (3.10).

In Figure 3.10, a single sample path of stochastic flowing particle is shown with simulation of stochastic outwards normal of interface; its trajectory defines the instantaneous liquid core boundary; its angle defines instantaneous outward normal; Inlet parameters: $u_{g,0} = 60m/s$, $u_{l,0} = 0.52m/s$.

Figure 3.7: Example of sample path on unit sphere; this Brownian trajectory evolves along with displacement of floating stochastic particle (Zamansky *et al.*, 2010).

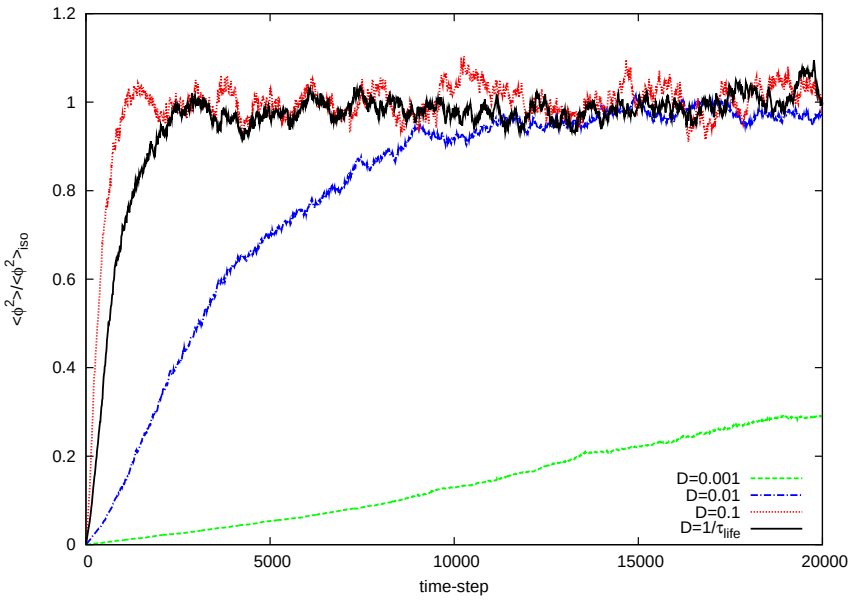

Figure 3.8: Evolution of the variance of ϕ. Comparison with different diffusion coefficient D.

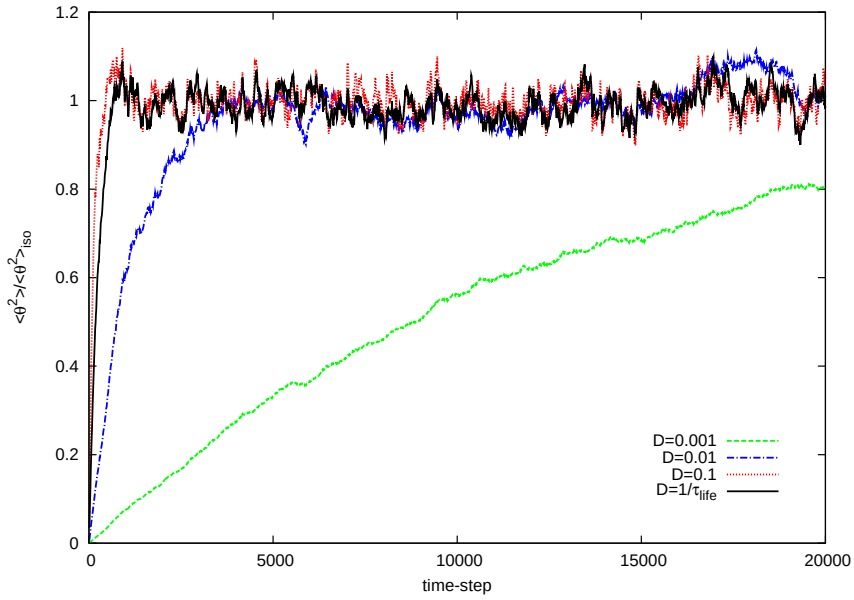

Figure 3.9: Evolution of the variance of θ. Comparison with different diffusion coefficient D.

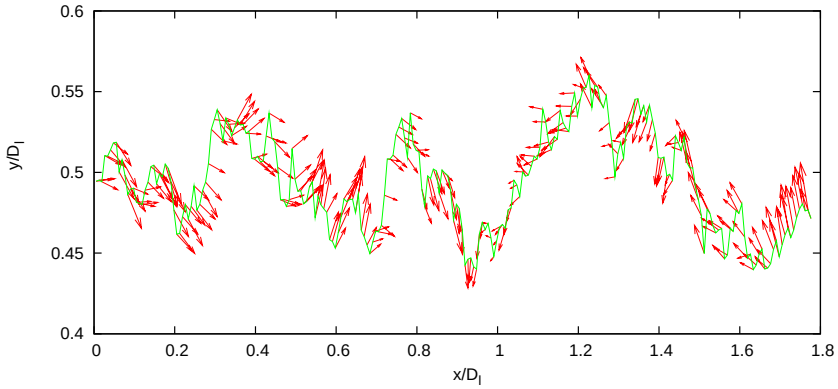

Figure 3.10: Single sample path of stochastic particle with stochastic outwards normal of interface.

3.3 Model for the magnitude of local acceleration $\dot{U}_s$

In the connected phase of immersed composite body, i.e. in the sub-region with $P_l \neq 0$, the instantaneous local acceleration may be either the local acceleration of liquid, if a given point is visited by the liquid, or the local acceleration of gas, if this point is visited by the gas, or the local acceleration of the interface, if the given point is visited by the interface. The last acceleration is dominant: the liquid/gas interaction controls the flow dynamics closely to injector. To this end, in discrete form of (2.42).

Let us assume that

$$\dot{U}_s n_i = \frac{u_s^{n+1} n_i - \langle u_i \rangle^n}{\Delta t} \tag{3.25}$$

where $u_s^{n+1} n_i$ denotes the interface velocity. Then in the sub-region with $0 < P_l < 1$, the above equations are reduced to $\langle u_i \rangle^{n+1} = (1 - P_l)\langle u_i \rangle^n + P_l u_s^{n+1}$; , if $P_l = 1$ then $\langle u_i \rangle^{n+1} = u_s^{n+1} n_i$. In this study, the interface velocity is taken to be constant, and to be equal to the convection velocity (3.11):

3.4 Model of the dispersed (disconnected) phase

3.4.1 Primary liquid blob formation in $0 < P_l < 1$; definition of size and starting angle

Using simulated distribution $P_l(\vec{x}, t) = \langle \delta(\xi(\vec{x}, t) - r_S) d\xi \rangle$, the next step is to sample drop's location in $0 < P_l < 1$. Along with this position, each formed blob need to prescribe its size and initial direction. The last one will control the spray angle. In this study, the size is sampled from the presumed negative exponential distribution function. Such a distribution emerges usually in random processes, when the probability of finding the parent liquid element becomes proportional to the probability of finding of product droplets: $f(r_1 + r_2) \approx f(r_1) f(r_2)$; this functional equation is satisfied if and only if $f(r)$ is exponential. Since according to experimental observation, the drops are stripped from ligaments, which are

raised from Rayleigh-Taylor instability, this distribution is normalized by λ_{RT} according to (1.11). We have:

$$f(r) = \frac{1}{\lambda_{RT}} exp(-\frac{r}{\lambda_{RT}}) \tag{3.26}$$

The moments of (3.26) are defined by $\langle r^m \rangle_f = \lambda_{RT}^m \cdot m!(m = 0, 1, 2...)$. The sampling of drops is organized in such a way that the injected liquid mass is continuously conserved in drops produced by (3.26). This is done by the following procedure.

Supposing a distribution $g(r)$ in such a way that $g(r)dr$ is the probability that a particle has drops with radii in the range $(r, r+dr)$. $g(r)$ should be proportional to the mass distribution $r^3 f(r)$ and the number of drops per particle $f(r)/g(r)$ should be proportional to $1/r^3$. Then the drop-size distribution can be obtained where the values of $g(r)$ are largest. The total droplet mass associated with each particle should be constant, which is determined by dividing the input total spray mass to be injected by the input total number of parcels to be injected. As we selected radius values randomly with the distribution $g(r)$, we first find the cumulative distribution $h(r)$ associated with $g(r)$, and then apply the inverse of $h(r)$ to random numbers uniformly distributed in the interval $(0, 1)$. If XX is a random number in the interval $(0, 1)$, after finding the value of n for which $h(n-1) \leq XX \leq h(n)$, we could get the corresponding drop radius.

To each drop sampled in $0 < P_l < 1$, with size governed by (3.26), one needs to prescribe its initial direction. Then the initial spray angle will represent the statistics of initial directions of formed primary blobs. It is worth to remind that the initial spray angle is an important and easily measurable parameter of the spray, In Villermaux (1998) and Lasheras & Hopfinger (2000), the measurement of the spray angle under air-blast atomization is generalized by the following expression:

$$\theta \approx [45^\circ - \frac{1}{2} \arctan(\frac{M^{\frac{1}{2}}}{6})] \tag{3.27}$$

in which $M = \rho_g u_{g,0}^2 / \rho_l u_{l,0}^2$. In our simulations, we assumed that primary drops are stripped from the interface characterized by simulated outwards normal vector $\mathbf{n}$. The procedure is as follows. Similar to Villermaux (1998), at the moment

when the drop is pinched off, the "so- called" entrainment velocity is characterized by equality of momentum fluxes in the liquid and the gas. Additionally in our simulation, the direction of the entrainment velocity is introduced, and it is defined by $\mathbf{n}$. Using input parameters in expression of the entrainment velocity, we have:

$$\mathbf{u}_e = u_{l,0}\sqrt{\frac{\rho_l}{\rho_g}}\mathbf{n} \tag{3.28}$$

Hence tangent of the initial spray angle may be given by the ratio of the entrainment velocity (3.28) and the convection velocity (3.11):

$$\tan\theta = n_y \frac{u_{l,0}\sqrt{\rho_l/\rho_g}}{u_s} \tag{3.29}$$

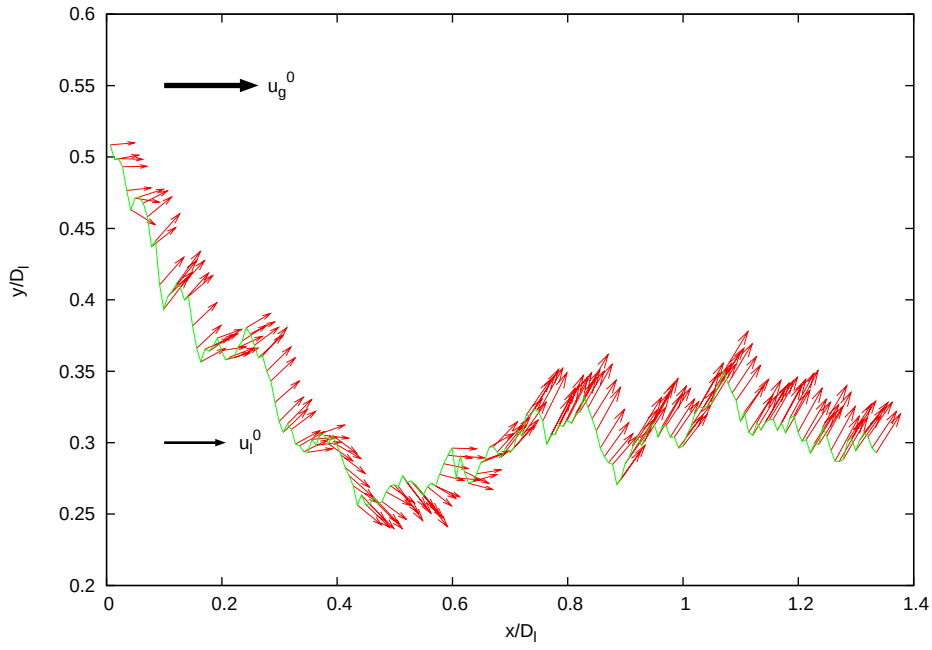

Figure 3.11: Single sample path of stochastic particle; with typical initial angle from (3.29). Inlet parameters:$u_{g,0} = 60m/s$, $u_{l,0} = 0.52m/s$.

Figure 3.11 shows a single sample path of stochastic flowing particle with simulation of direction for produced primary blob according to (3.29). As in Figure 3.10, its trajectory defines the instantaneous liquid core boundary. The statistics

of angle from ensemble of such particles will give the direction distribution at a given control volume. From this distribution, the direction is defined for drop, which has been produced in this control volume. The inlet parameters for shown in this figure particle are: $u_{g,0} = 60m/s$, $u_{l,0} = 0.52m/s$.

So far the size r , the angle θ , and the position in $0 < P_l < 1$ are prescribed to each formed primary blob. Their motion equation is described by equations in next Section.

3.4.2 Motion equation of sampled primary blobs; micro-dynamics averaged over inter- drops collisions

Closely to air-blast injector, the flow dynamics is strongly characterized by collisions between liquid elements (Hopfinger, 2001). Therefore it is necessary to take into account these collisions in the near-to-injector dynamics. However the collision process between liquid fragments in the near-to-injector region is too complicated. Hence it would be interesting to account for such collisions, but in effective, say "outflank" way. Such a way, was proposed in (Chtab & Gorokhovski, 2007). We use here this approach. In this approach, the collisions between particles are viewed as a multiple process, with frequency large enough in order to assume collisions to be isotropic in the sense of classical kinetic approach (Landau & Lifshitz, 2000). Namely, the particle velocity correlation is identified by the particle temperature of ordinary statistical mechanics. Instead of tracking real particles with jumping trajectories due to collisions, the approach of (Chtab & Gorokhovski, 2007) proposed to track hypothetical particles along smoothed trajectories, which are controlled by the motion equation averaged over inter-particle collisions. The statistics of hypothetical and real particles become similar if the collision frequency is very high. Starting by consideration of turbulent two-phase flow, as a system of interacting fluid and solid particles, the following equation was derived:

$$\frac{d\overline{v_{p,i}}}{dt} = -\frac{\partial}{\partial x_i}(\frac{T_p}{m_p}) + \frac{1}{n_p}\int \overline{v_{p,i}} I_{p,g} d^3\overline{v_{p,i}} \tag{3.30}$$

in which $v_{p,i}$ is the instantaneous component of the liquid drop velocity, while $\overline{v_{p,i}}$ is component of the liquid drop velocity but averaged over inter-drop collisions;

$m_p = \rho_l \frac{4}{3}\pi r^3$ is the particle mass (known when size is sampled from (3.26), T_p is the statistical temperature due to collisions, and $I_{p,g}$ is the collision operator characterizing collisions between solid and fluid particles. Instead of a particle in (Chtab & Gorokhovski, 2007), let us use (3.30) for a drop, which has been formed closely to injector. The last term in (3.30), we approximate by the Stokes relaxation. In our case, it writes:

$$\frac{d\overline{v_{p,i}}}{dt} = \begin{cases} -\frac{\partial}{\partial x_i}(\frac{T_p}{m_p}) + \frac{\langle u_i\rangle - \overline{v_{p,i}}}{\tau_{st}}, & \text{if} \quad P_l \neq 0 \\ \frac{\langle u_i\rangle - v_{p,i}}{\tau_{st}}, & \text{if} \quad P_l = 0 \end{cases} \tag{3.31}$$

We need to closure (3.31) by expressions for statistical temperature $\frac{T_p}{m_p}$, and for the Stokes time τ_{st}. The classical expression for the Stokes time is (see Clift *et al.*, 1978, for example):

$$\tau_{st} = \frac{2\rho_l r^2}{9\rho_g \nu_g} \frac{1}{1 + 0.15 Re_p^0.687} \tag{3.32}$$

where Re_p is the Reynolds number of drop. The expression for $\frac{T_p}{m_p}$ is given in next Section.

3.4.3 Expression for statistical temperature of drop

The statistical temperature (per unit mass of drop) $\frac{T_p}{m_p}$ may be approximated by kinetic energy of relative liquid-to-gas motion:

$$\frac{T_p}{m_p} = \overline{U_{rel}^2} \tag{3.33}$$

Two physical variables are assumed to control this energy. The first one is the dissipation of kinetic energy of the gas flow, which is taken here from the resolved velocity field:

$$\varepsilon = \frac{1}{2}\nu_g (\frac{\partial \langle u_i\rangle}{\partial x_j} + \frac{\partial \langle u_j\rangle}{\partial x_i})^2 \tag{3.34}$$

It is seen that this variable will significantly contribute due to velocity gradients introduced by the composite immersed body force. The second variable represents the typical time of drop drag, in which its inertia is accounted; this

time-scale is the Stokes time τ_{st}. Hence the estimation of kinetic energy in the relative liquid-to-gas motion is proposed to be as:

$$\overline{U_{rel}^2} = \varepsilon \tau_{st} \tag{3.35}$$

and

$$\frac{T_p}{m_p} = \frac{1}{2}\nu_g(\frac{\partial\langle u_i\rangle}{\partial x_j} + \frac{\partial\langle u_j\rangle}{\partial x_i})^2\tau_{st} \tag{3.36}$$

Another simple closure is known from Zaichik *et al.* (2003), Zaichik & Alipchenkov (2003), Reeks (1977), Wang & Stock (1993) for the statistically homogeneous and stationary turbulent field laden by heavy particles:

$$\frac{T_p}{m_p} = \overline{\mathbf{u}^2}\frac{T_L}{T_L + \tau_{st}} \tag{3.37}$$

in which $\overline{\mathbf{u}^2}$ is the averaged kinetic energy, and T_L is the Lagrangian turbulent time-scale. In terms of LES, the averaged kinetic energy may be approximated by local sub-grid kinetic energy, as $\overline{\mathbf{u}^2} \sim (\frac{\nu_{eff}}{\Delta})^2$, where $\nu_{eff} = \nu_g + \nu_{tur}$ is the effective viscosity, with the Smagorinsky viscosity ν_{tur}, and the width of filter Δ , and the turbulent time scale is given by the strain rate norm $T_L \sim |S_{ij}|^{-1}$. Then a rough estimation of (3.36) may be written in the following form:

$$\frac{T_p}{m_p} = (\frac{\nu_{eff}}{\Delta})^2\frac{1}{1 + \tau_{st}|S_{ij}|} \tag{3.38}$$

In Chapter 5, we will compare the application of (3.36) and (3.38) in the framework of (3.31).

3.5 Secondary atomization modeling

Two models of secondary atomization are traditional. One is referred to as Taylor analogy breakup (TAB) (O'Rourke & Amsden, 1987), another is referred to as WAVE (Reitz, 1987) model. The TAB model (O'Rourke & Amsden, 1987) is based on the Taylor (1963) analogy between oscillating/distorting droplet and a spring-mass system, in which the spring force, external force and dampening

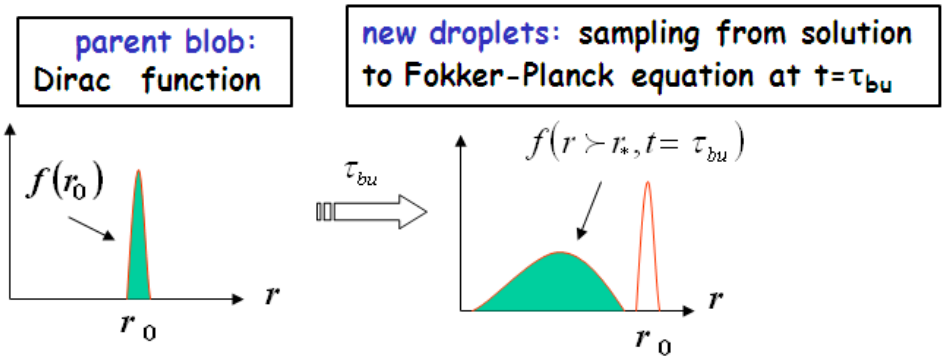

Figure 3.12: Schematic of stochastic modeling of secondary atomization.

are associated to surface tension, aerodynamic forces, and drop viscosity, respectively. Breakup is assumed to occur when the oscillations exceed a critical value. Finally, energy conservation is used to determine the fragment sizes after breakup within presumed χ-squared distribution. In the WAVE model (Reitz, 1987), new droplets are formed proportionally to the growth rate of the fastest wave instability on the parent blobs surface. Both models are deterministic, with "single-scale" production of new droplets. In this study we use the stochastic model of secondary breakup proposed in Gorokhovski (2001), Apte *et al.* (2003) and Gorokhovski & Saveliev (2003). Schematically, this model is illustrated in Figure 3.12. Each parent blobs is characterized by Dirac peak in terms of size distribution. During typical breakup time, this peak evolves in the space of size according to Fokker-Planck differential equation (3.7). For normalized distribution of radius, $f(r;t)$, the solution to (3.7) is given in Gorokhovski & Saveliev (2003)

$$f(r,t) = \frac{1}{r}\int_0^\infty \frac{1}{\sqrt{2\pi\langle \ln^2\alpha\rangle \nu t}} \exp[\frac{-(\ln(r_0/r) + \langle \ln\alpha\rangle \nu t)^2}{2\langle \ln^2\alpha\rangle}\nu t] f_0(r_0) dr_0 \quad (3.39)$$

where $f_0(r_0)$ is the initial distribution of droplet radius before breakup. If $f_0(x) = \delta(r_0 - r)$, this solution, at $\nu t = 1$, has the following form:

$$f(r; \frac{t}{\tau_{bu}=1}) = \frac{1}{\sqrt{2\pi\langle \ln^2\alpha\rangle}} \exp[-\frac{(\ln\frac{r}{r_0} - \langle \ln\alpha\rangle)^2}{2\langle \ln^2\alpha\rangle}] \quad (3.40)$$

From (3.40) new droplets are sampled after passage of breakup time, with such number of parcels that the mass in parent and produced droplets is conserved. The breakup model is activated whenever radius of parent drop is greater than critical radius $r > r_{cr}$, which was described in Introduction. The choice of breakup time was taken by dimensional analysis. Three typical variables may control this typical time: the surface tension, the liquid density, and the viscous dissipation rate. From these three variables, only one combination is:

$$\tau_{bu} = const(\frac{\sigma^2}{\rho_l^2 \varepsilon^3})^{\frac{1}{5}} \tag{3.41}$$

where the constant is supposed to 1.

Chapter 4

Numerical Methods and Mesh Resolution

In this chapter, the details of numerical procedure for LES are provided. Three approaches for turbulence modeling are introduced briefly in Appendix B. Fundamental steps involved in deriving LES equations are SGS modeling and filtering. Some issues with filtering are also explained in Appendix B. Some turbulent scales in Appendix C.

4.1 Numerical Methods

4.1.1 Spatial Integration Method

The numerical method was developed by Stanley *et al.* (2002) to perform direct numerical simulation of a plane jet. It is based on their earlier studies and is summarized below. The spatial derivatives are computed using a non-uniform fourth-order compact scheme based on the uniform scheme of Lele (1992). The idea of compact schemes is to approximate the derivatives not only from the values at neighboring points but also from the derivatives at neighboring points. Details on compact scheme on uniform meshes and on non-uniform meshes can be found in Appendix D.

4.1.2 Time Integration Method

The fourth-order Runge-Kutta scheme of Carpenter *et al.* (1993) is used for the time integration of the convective terms. It is a five-stage scheme for which the fifth stage is added to improve the stability. To save computational time, the viscous terms are advanced using a first-order scheme. It is implemented by advancing the Euler terms using the fourth-order Runge-Kutta scheme and then evaluating and advancing the viscous terms in time using a first-order scheme.

4.1.3 Boundary conditions

Non-reflecting boundary conditions to take into account all the information passing inward and outward across the boundaries while minimizing spurious reflections have been proposed by Thompson (1987) and Giles (1990).

At the inflow boundary, the time variation of the incoming characteristic variables is specified while the equation for the outgoing characteristic variable is solved using internal biased derivatives. This approach allows the proper specification of the incoming characteristic waves at this boundary.

Moreover, to isolate the interior of the domain from the effects of the boundary conditions, a buffer zone based on the approach of Hu (1996) is used on the non-reflecting boundaries. The buffer zone is a numerical construct that consists of a stretched grid with additional nodes placed around the computational domain where exponential damping terms are added to the governing equations.

For the outflow as well as the upper and lower sidewall boundaries, the non-reflecting conditions of Thompson (1987), based on the characteristic equations, are used. These boundary conditions are allowed to switch between inflow and outflow at each point depending on the instantaneous local normal velocity. The corner points are treated as non-reflecting in planes 45 degrees from the adjacent boundaries. At the non-reflecting outflow points an additional pressure correction term, proposed by Rudy & Strikwerda (1980), is used to maintain the pressure near a specified free-stream pressure.

Periodic boundary conditions are used in the z direction.

4.2 Gas inflow condition

The longitudinal mean velocity profile at the inflow is a top-hat profile with smooth edges. A hyperbolic tangent profile is used:

$$U = \frac{U_1 + U_2}{2} + \frac{U_1 + U_2}{2} \tanh(\frac{y}{2\theta}) \tag{4.1}$$

where θ is the momentum thickness. U_1 designates the longitudinal velocity in the middle of the jet and U_2 is the co-flow velocity. The co-flow velocity is small, $U_2/\Delta U = 0.1$, so that, for the streamwise distances considered here, the evolution is similar to that of a jet with no co-flow. The mean lateral velocity is initialized as $V = 0$ while the density and the pressure are uniform.

A broadband forcing representative of isotropic turbulence is utilized at the inflow. The three-dimensional energy spectra of the velocity fluctuations at the inflow is

$$E(k) = \frac{k^4}{16} \exp[-2(-k/k_0)^2] \tag{4.2}$$

where the peak frequency k_0 is set to the most unstable mode for the hyperbolic tangent shear layer. The lateral shape, across the jet, is such that the fluctuation intensity peaks in the shear layers on either side of the jet.

4.2.1 Computation conditions

The summary of conditions used for the simulations are presented in the Table 4.1. To compare the results with experiment (Hong, 2003),the computational conditions are: the gas jet width is $D_g = 0.04m$ while the injected liquid width is $D_l = 0.02m$. The Reynolds number for the jet, Re_g^0 based on the gas jet width and the injected velocity of gas $u_{g,0}$ is $Re_g^0 = u_{g,0} D_g/\nu_g$. The Reynolds number based on the initial shear layer momentum thickness is $Re_\theta = 150$.

The composition of the gas phase is that of a standard air. The liquid injected is water. The boundary conditions that are of a serious concern in LES are dealt here with by using a closed domain. Initially the gas phase is stationary with a low, residual level of turbulence. The turbulence generation throughout the

Table 4.1: Computational Conditions

	Injected Velocity of Gas (m/s)	Injected Velocity of Liquid (m/s)	$M = \frac{\rho_g u_{g,0}^2}{\rho_l u_{l,0}^2}$
Case 1	60	0.52	16
Case 2	20	0.17	16
Case 3	30	0.26	16
Case 4	40	0.34	16
Case 5	50	0.43	16
Case 6	70	0.61	16
Case 7	80	0.69	16
Case 8	90	0.78	16

simulation can then be attributed exclusively to the injection of the liquid and subsequent two-phase interactions.

4.3 Mesh resolution for LES

For large eddy simulations, the computational grid must be chosen such that the separation of the resolved and the subgrid-scales occurs in the inertial subrange of the energy spectrum. Accordingly, the smallest grid size has been chosen to be one order of magnitude larger than that of the smallest scales (Kolmogorov scale). According to (C.6) and ϵ estimated as Standard $k-\epsilon$ Model:

$$\epsilon = [\frac{C_\mu}{Pr_\epsilon(C_{\epsilon 2} - C_{\epsilon 1})}]^{\frac{1}{2}} \frac{k^{\frac{3}{2}}}{(D_g - D_l)} \tag{4.3}$$

$$k = \frac{3}{2}u'^2 \tag{4.4}$$

where u' is 0.05, the constants are $C_\mu = 0.09$, $Pr_\epsilon = 1.3$, $C_{\epsilon 1} = 1.44$ and $C_{\epsilon 2} = 1.92$, Kolmogorov scale η is approximately 0.002. The smallest grid length in the computational domain was chosen to be 0.066 in the y direction.

In reality we do not used either very coarse or very dense meshing because of the following reasons:

- Coarse mesh is unable to capture important turbulent structures and causes the subgrid model to account for too high a percentage of the turbulent kinetic energy of the flow.

- Very dense mesh is reserved for DNS simulations and in this region benefits of LES clearly vanish.

A $96 \times 121 \times 16$ computational grid (Figure 4.1 and 4.2) has been constructed. The physical domain has the following dimensions: $L_x = 7$, $L_y = 15$ and $L_z = 2$. All the meshes have been nondimensionalized by the liquid jet width D_g. These dimensions do not include the additional buffer zones at the jet exit and sides. In the x direction, the grid is relatively fine between 0 and 1 with $h_x = 0.066$ in order to have adequate numerical resolution of the inflow region. Between $x = 2$ to $x = 7$ the grid is uniform with a grid spacing $h_x = 0.25$ and a short transition zone between $x = 1$ and $x = 2$. In the y direction, it is uniform in the center of the jet from $y = 7.5$ to $y = 8.5$, where $y = 7.5$ represents the center of the jet, with a grid spacing $h_y = 0.066$ in order to solve the initial shear layer and then is slightly stretched until the side buffer zones. The mesh is mirrored across the centerline of the domain. In the z direction, the mesh is uniform with $h_z = 0.25$.

4.3.1 Grid Sensitivity

The grid sensitivity of the LES results can be estimated from solutions on a sequence of refined grids. The grid described above and three other fine grids are taken account. For the fine grid '$96 \times 245 \times 16$', the minimum gridlength for the fine grid in the y direction of the flow field is half that for the grids '$96 \times 121 \times 16$', and in the region of $y = 7.5$ to $y = 8.5$ with $h_y = 0.033$. The fine grid $96 \times 245 \times 32$' has the same grids number in the y direction as '$96 \times 245 \times 16$', but 2 times for the z direction. The last grids '$133 \times 245 \times 32$' is based on '$96 \times 245 \times 32$' and 2 times of the grid number between $x = 0$ and $x = 1$, $h_x = 0.033$.

In Figures 4.3 - 4.6, the solutions on various grids for the average and RMS of the gas velocity along the y coordinate in the far-field downstream are compared. It is observed that the jet spreads with distance along the stream-wise direction. It is also observed that jet tends to become symmetric as the distance from the

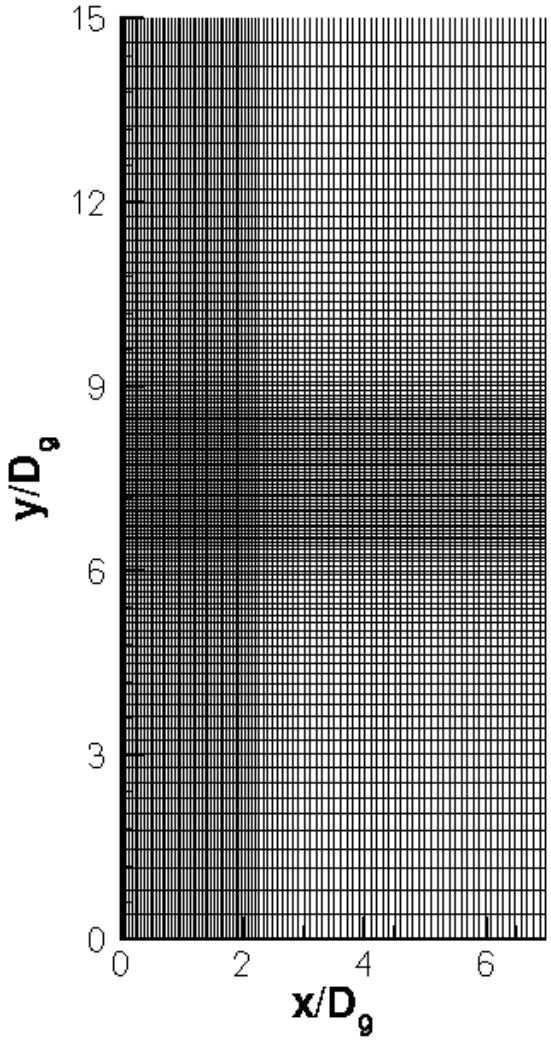

Figure 4.1: Computational grid on a $x - y$ section.

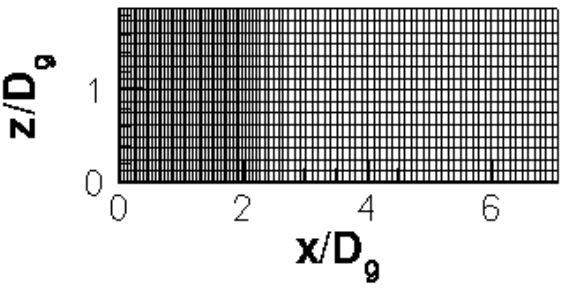

Figure 4.2: Computational grid on a $x - z$ section.

jet source increases and the spreading rate is depressed in the outer portion of the jet. The RMS profiles have peaks where the averages have large gradients.

Compared to the '96×121×16' grids, it can be seen that with the refinement of mesh, the improvement in the prediction by refining the mesh is not big whereas leading to increase computational times.

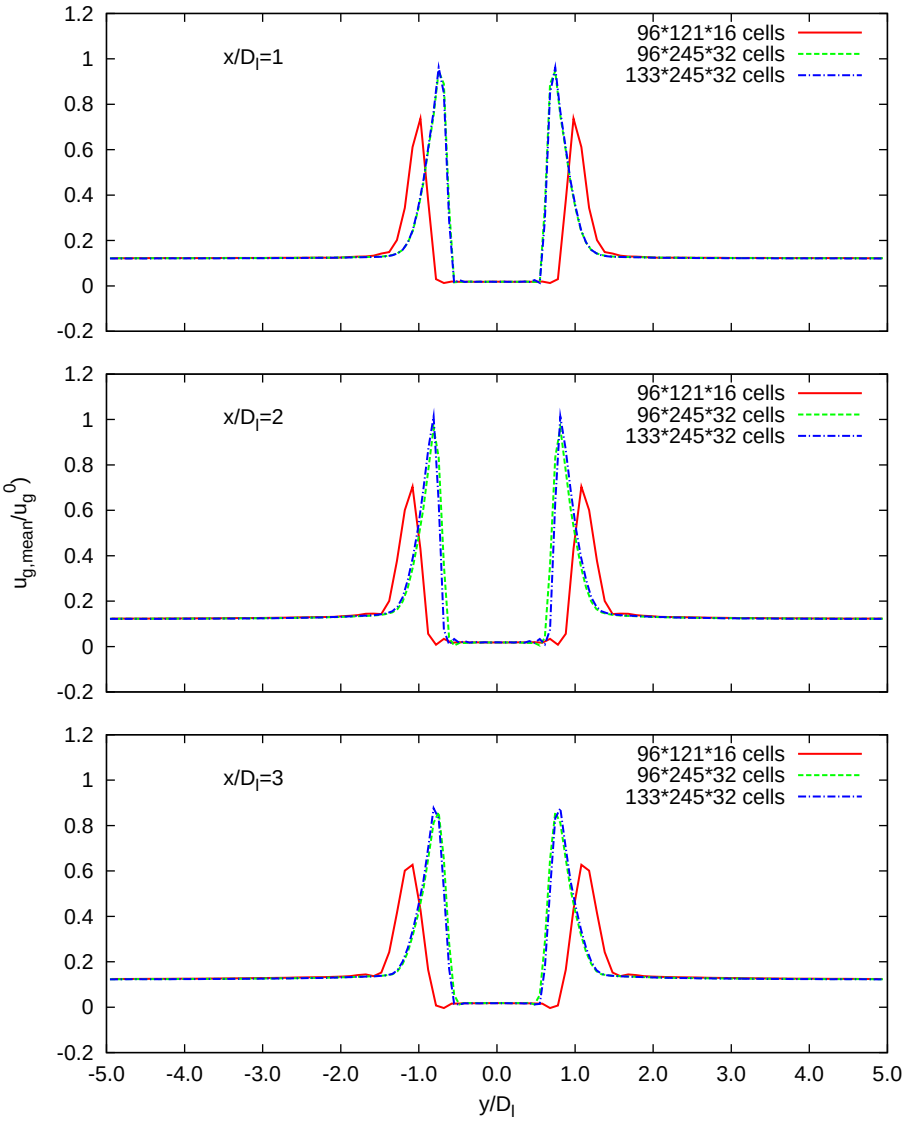

Figure 4.3: Mean u velocity of gas at different sections.

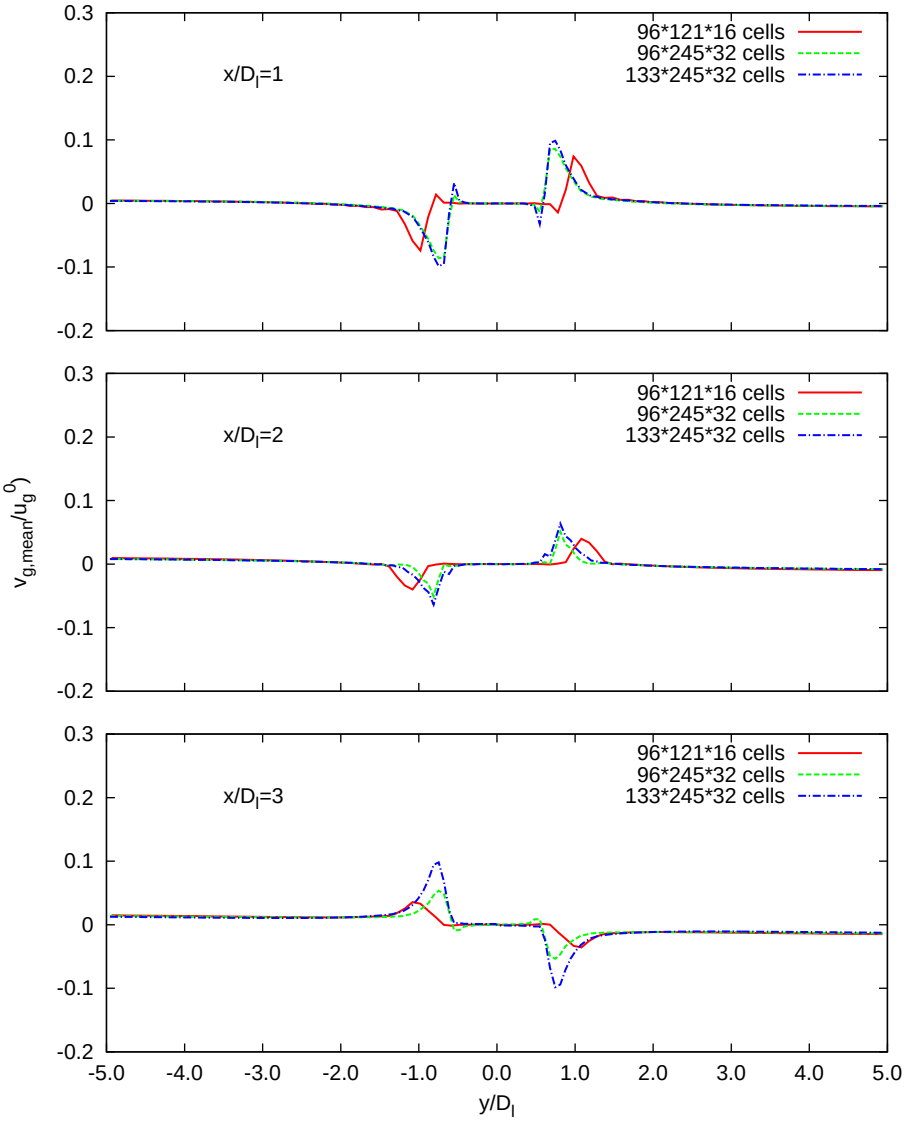

Figure 4.4: Mean v velocity of gas at different sections.

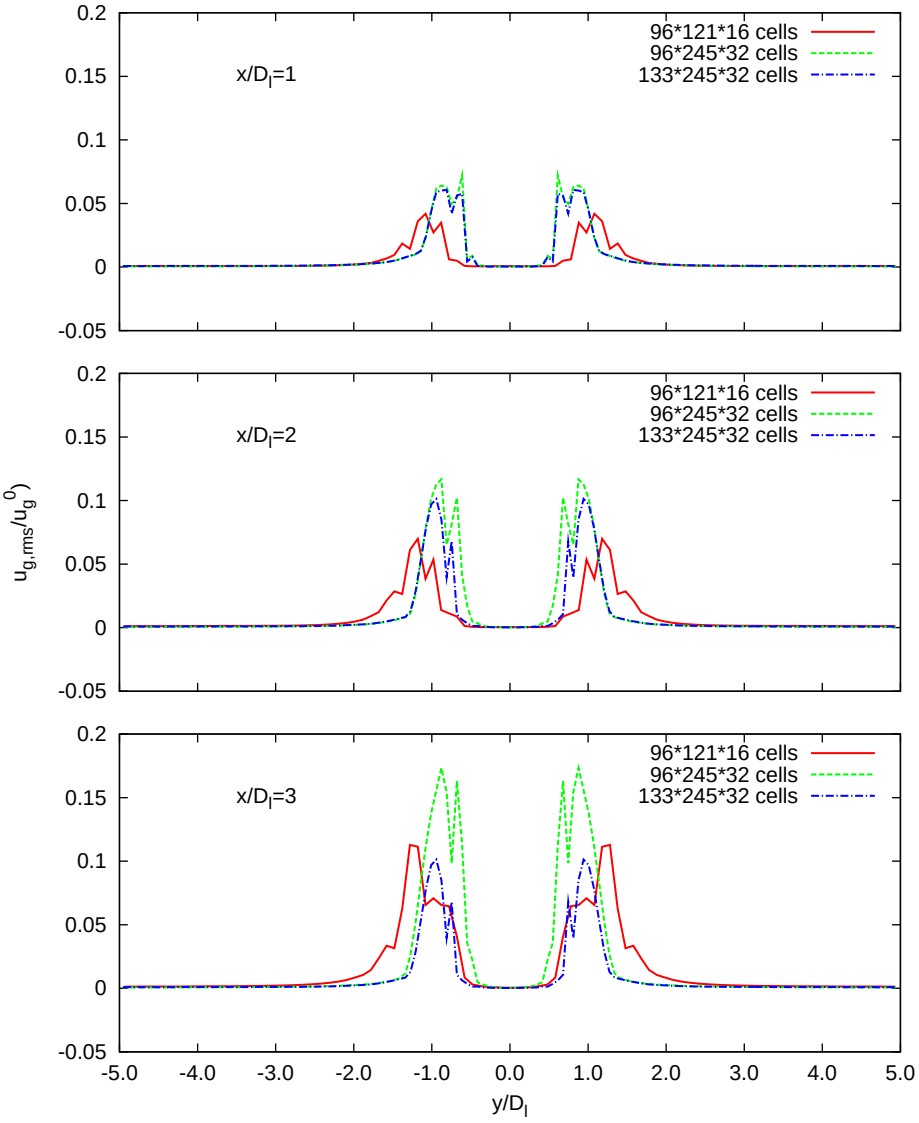

Figure 4.5: u_{RMS} of gas at different sections.

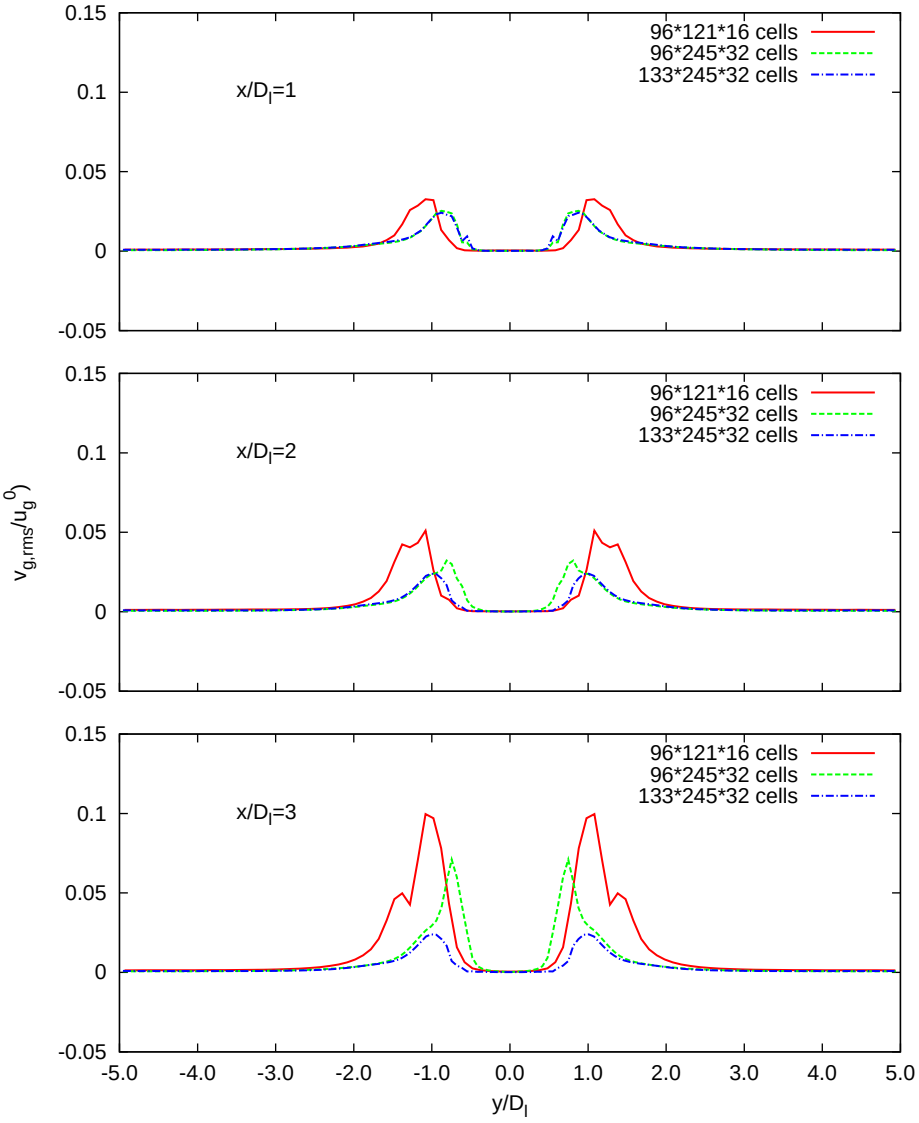

Figure 4.6: v_{RMS} of gas at different sections.

Chapter 5

Assessment and simulation of spray formation and flow closely to air-blast atomization

This Chapter represents our results of numerical integration of equations (2.42) and (2.46) which were closed by stochastic models described in Chapter 3: (3.9)-(3.15), (3.22), (3.25). The assessment of numerical results is given by comparison of simulation with experimental study from Hong (2003) (experimental setup and inlet conditions are given in Chapter 1. The numerical method is described in Chapter 4, and essentially, in Appendix.

5.1 Setup of experimental system of Hong (2003)

In this section, the experimental system used to simulate the spray formation and flow closely to air-blast atomization is presented. The experimental results mentioned in this thesis are from the plane jet experiment by Hong (2003).

The scheme of the plane jet is as Figure 5.1. The injector includes one planar convergent nozzle that produces the liquid jet in the lower part of the facility, and the other converging nozzle, located above the first one, and which generates a gas jet. In the experiments, the lower part is supplied with water, the flow velocity, u_l, can vary between 0.1 to $1m/s$. The upper part is supplied with air, the flow velocity, u_g, can be modulated from 10 to $100m/s$. Both outputs are elongated

rectangle $100mm$ wide. The jets are of the same height $H = 10mm$, which means the outlet of liquid is $D_l = 0.02m$ and the outlet of gas is $D_g = 0.04m$. The plate separator has a thickness of less than $0.1mm$ at its end. Moreover, beyond the exit of the jets, a strong horizontal plate is located in the lower zone of the liquid jet. The origin of the abscissa x corresponds to the output section of the injector, and height y is counted from the lower horizontal plate. The Reynolds number based on thickness of canal, $Re_l = \frac{\rho_l u_l D_l}{\mu_l}$, has order of $10^{3\sim4}$. The Weber number, $We = \frac{\rho_g u_g^2 D_l}{\sigma}$, varies from 33 to 3300. The Froude number ($Fr = \frac{u_l}{gH}$) calculated with the velocity interfacial $u_i \approx \sqrt{\rho_g/\rho_l} u_g(1 + 1/\sqrt{M})$ (M is the momentum ratio $M = \rho_g u_g^2/\rho_l u_l^2$) and the wave amplitude δ is $\gg 1$.

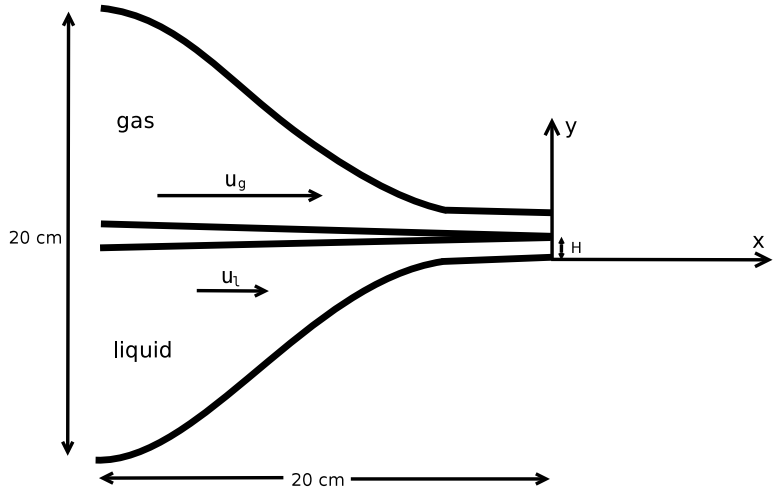

Figure 5.1: The scheme of the plane jet (Hong, 2003).

In a first series of tests, it was to access the evolution of speeds and drop sizes as a function of air velocity in the primary atomization zone. For this, the measuring point was kept fixed, at $x/D_l = 1.5$ and $y/D_l = 0.5$ (that is to say, right to the end of the liquid nozzle), and u_g has ranged from 20 to $90m/s$ while maintaining the ratio of quantities of constant motion ($M = 16$).

A second series of tests was conducted to measure the two-phase field, and appreciate the spatial evolution of various quantities in the area near the injectors. These measurements were made over a hundred positions for a gas velocity $u_g = 60m/s$ maintaining M constant ($M = 16$). The space extends scans of $x/D_l = 0.5$

to 5 and $y/D_l = 0.5$ to 1 depending on the downstream distance. The areas near the dividing wall $y/D_l \leq 0.5$ have not been examined because the latter leads to the formation of a continuous liquid film that is not representative of a situation coaxial atomization.

5.2 Flow field and droplets in the vicinity of the injector

For the same set of input conditions ($u_{g,0} = 60m/s$, $u_{l,0} = 0.52m/s$, which correspond to momentum ratio $M = 16$), two snapshots of filtered velocity field in the gas flow and spatial distribution of droplets position-and-size are shown in Figures 5.2 and 5.3. The impact of liquid core on the gas flow, as a flapping zone of dragged gas flow, the recirculation zone in front of the liquid core, and the large spectrum of produced droplets, from $10\mu m$ to $200\mu m$, at each spray position, is seen in this figure. It is also seen that the gas flow is characterized by strong velocity gradients around the liquid core, and by large scale vortical structures in the down-stream zone beyond the liquid core. It is seen that the region closely to injector is populated mostly by large liquid elements (drops in our simulation), along with the presence of mist of small stripped droplets. Such properties were emphasized in experimental observations of Hong (2003). For higher magnitude of the momentum ratio, $M = \rho_g u_{g,0}^2/\rho_l u_{l,0}^2$, $M = 70$ and $M = 220$ (same inlet gas-stream velocity, but different inlet velocity of the liquid), two snapshots of filtered velocity field in the gas flow and of spatial distribution of droplets position-and-size are shown in Figures 5.4 to 5.5. On can observe that with increasing momentum ratio M , the computed flow is characterized by less steepened velocity gradients around simulated liquid core, despite the increasing difference in inlet velocities between the gas and the liquid. This implies the stronger drag of the gas flow, with stronger cross-flow exchange of momentum, simulating more intensive atomization process. In our model, the increasing momentum ratio leads to more intensive impact of the immersed body force: with increasing M, the region of $P_l(s,t) \neq 0$ is getting shortened, $\dot{U}_s$ becomes higher, and in the down-stream direction, $n_i(\vec{x},t)$ is characterized by

faster relaxation to isotropy. Besides those observation, Figures 5.2 - 5.5, shows production of smaller droplets closely to injector with increasing momentum ratio M. Consequently with increasing momentum ratio M, finer-grained droplets are easy entrained into vertical motion in front of the liquid core: formation of "milky way" filaments is seen in Figures 5.4 and 5.5 when the momentum ratio M is high: $M = 70$ and $M = 220$.

5.3 Assesment of Mean Sauter diameter and mean kinetic energy of droplet; different axial positions and distances from the center-plane

Here we assess our statistics of droplet diameter and velocity in the near-field of the spray, $0 < x/D_l < 5$. Three different expressions for the drops statistical temperature (3.36) and (3.38), as well as standard approach with Lagrangian tracking without accounting for collisions, were used in computation. In the Figures 5.6 to 5.9, "simplified collision I" is corresponding to the fomula (3.36) and "simplified collision II" is corresponding to (3.38). For these three approaches, the mean Sauter diameter d_{32}, and the mean kinetic energy $\sqrt{u_p^2 + v_p^2 + w_p^2}$ are compared with measurements of Hong (2003) at different center-plane positions x from injector, and for each down-stream position, at different distances from the center-plane: $y/D_l = 0.5; 0.75; 1$. First, Figures 5.6 and 5.7 give this comparison, against measurements (Hong, 2003), using experimental expression (3.27), $\theta \approx [45^\circ - 0.5 \arctan(\frac{M^{\frac{1}{2}}}{6})]$, for primary formed blobs: this initial angle was randomly sampled in the range $0^\circ < \theta < [45^\circ - 0.5 \arctan(\frac{M^{\frac{1}{2}}}{6})]$. Figure 5.6 shows the mean kinetic energy of droplets, and Figure 5.7 shows the mean Sauter diameter. In Figure 5.6, it is seen that accounting for collisions in motion of blobs in the composite immersed body region may improve fairly the prediction of the drop kinetic energy along with evolution of spray closely to injector. This is seen specifically for $y/D_l = 1$, when expression (3.38) is used for the statistical temperature of droplets. The same conclusion may be made for prediction of the mean Sauter diameter, when collisions in the blob's dynamics are accounted. Figure 5.7 shows this comparison for the mean Sauter diameter of numerically

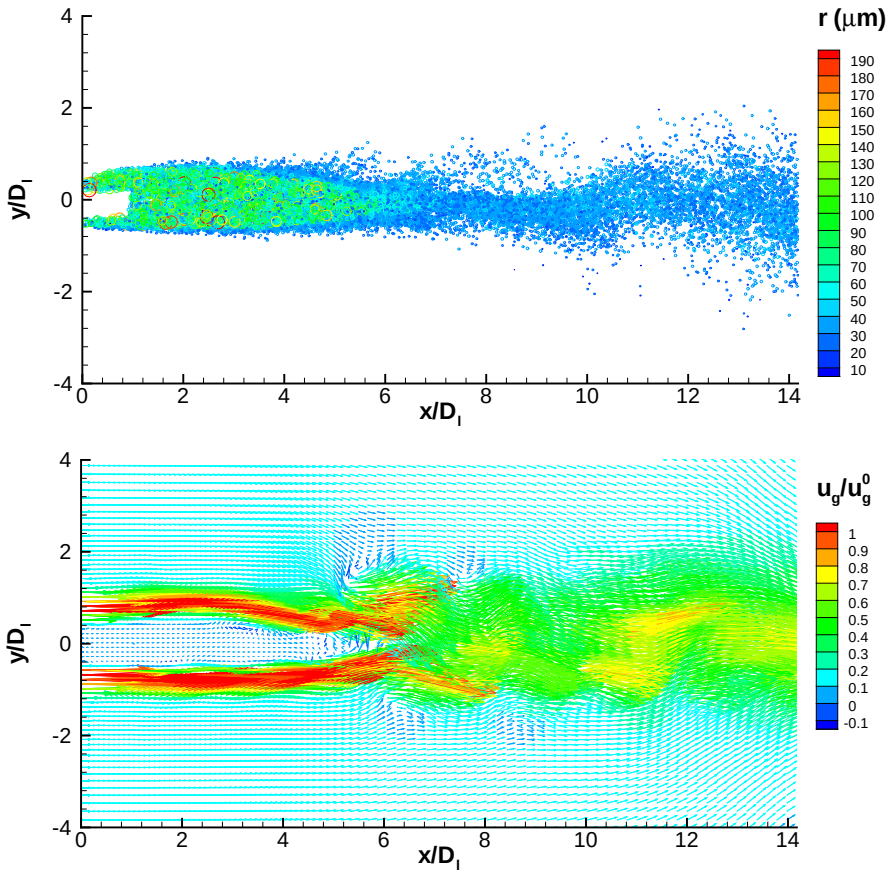

Figure 5.2: Snapshot of the droplet's position-and-size distribution, and the filtered velocity field in the gas flow. Inlet parameters: $u_{g,0} = 60m/s$, $u_{l,0} = 0.52m/s$, corresponding to $M = 16$.

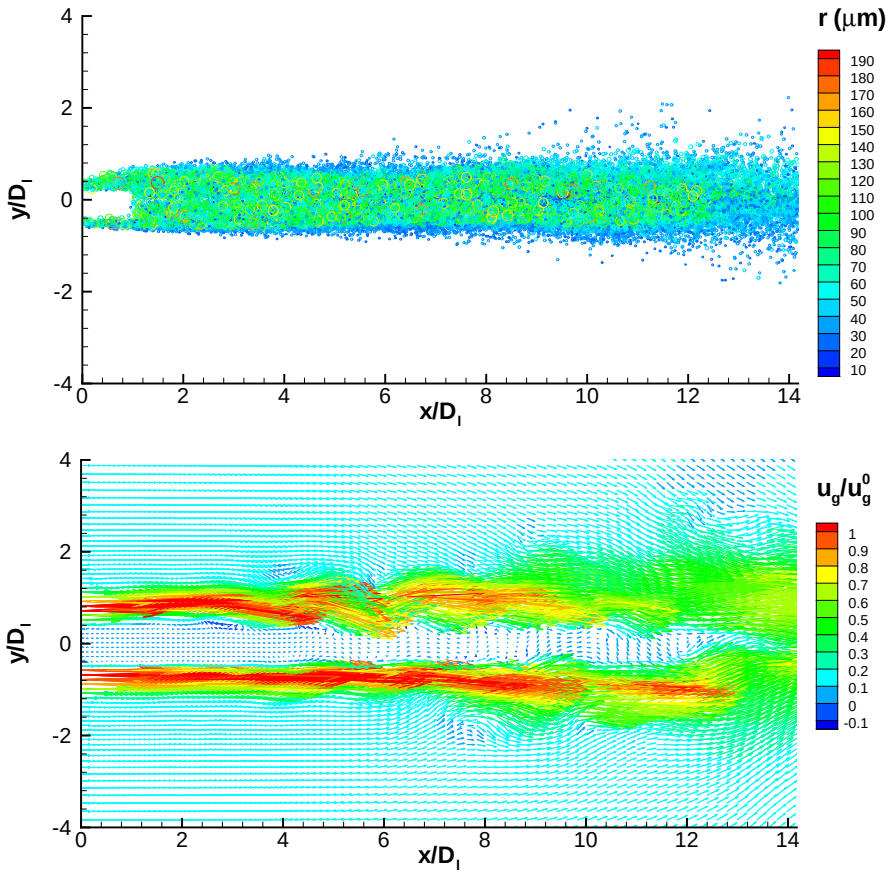

Figure 5.3: Snapshot of the droplet's position-and-size distribution, and the filtered velocity field in the gas flow. Inlet parameters: $u_{g,0} = 60m/s$, $u_{l,0} = 0.52m/s$, corresponding to $M = 16$.

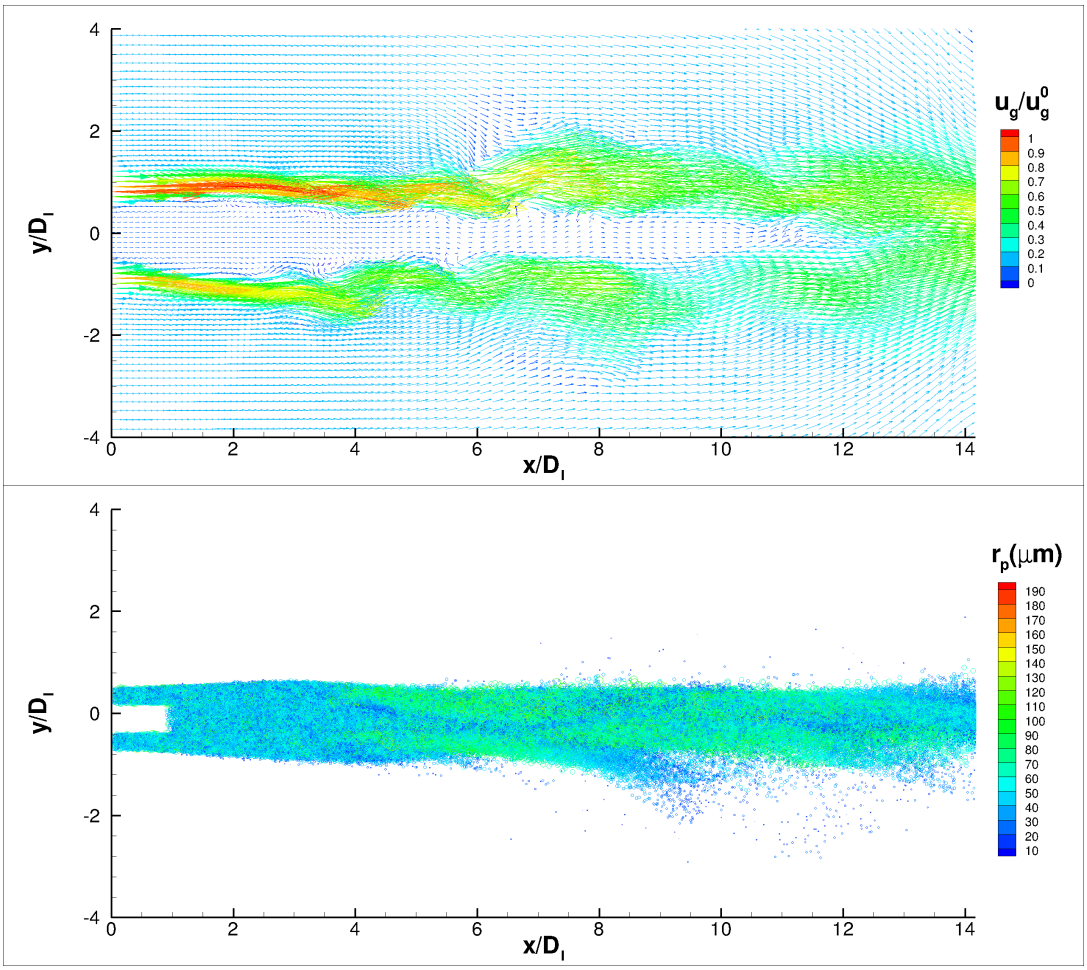

Figure 5.4: Snapshot of the filtered velocity field in the gas flow and the droplet's position-and-size distribution, $M = 70$.

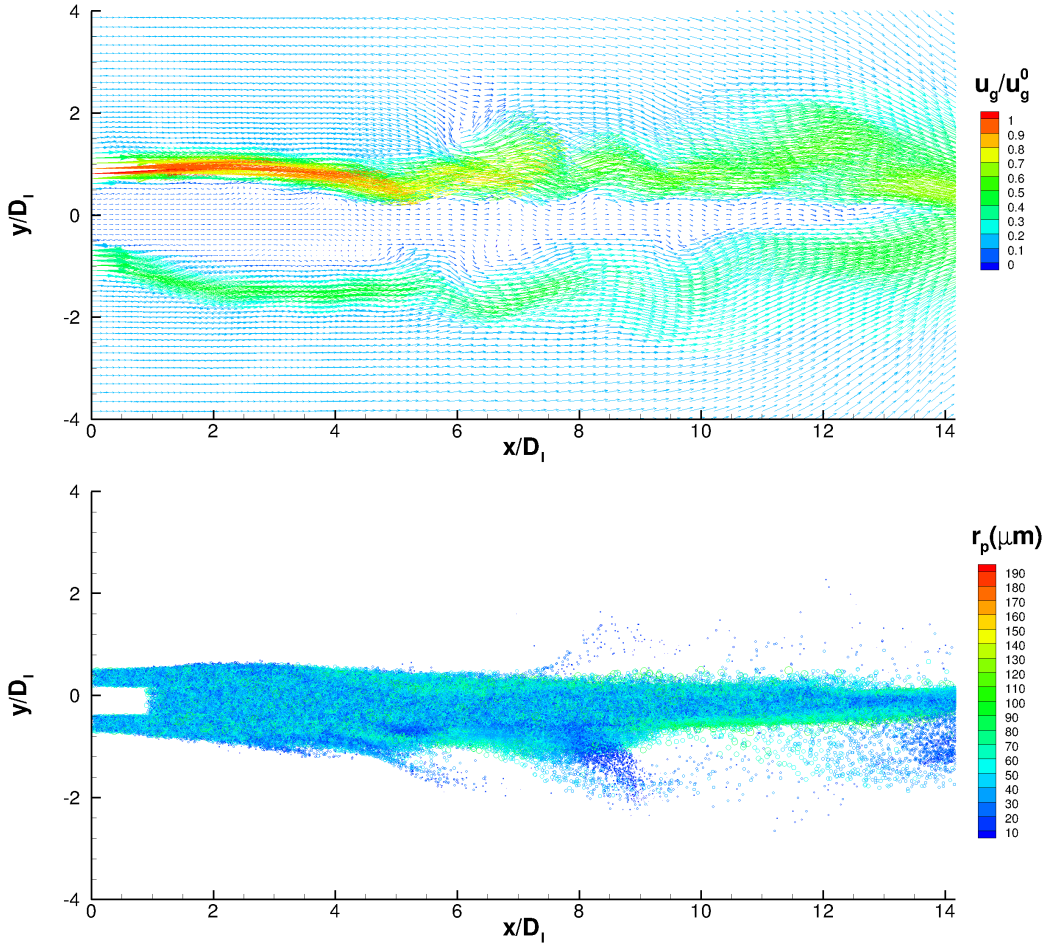

Figure 5.5: Snapshot of the filtered velocity field in the gas flow and the droplet's position-and-size distribution, $M = 220$.

produced droplets. It is seen that although along the line $y/D_l = 0.5$, predictions may underestimate measurements of diameter on approximately $50\mu m$, the predictions along $y/D_l = 0.75$ and $y/D_l = 1$ are fairly good, if expression (3.38) is used for the statistical temperature of droplets. Next comparison concerns the same case but with simulated initial angle for primary formed blobs instead of its presumed value from (3.27); the angle is given now directly from simulation of local outwards normal $n_i(\vec{x}, t)$ by using (3.29), $\tan\theta = n_y \frac{u_{l,0}\sqrt{\rho_l/\rho_g}}{u_s}$. Figure 5.8 shows the mean kinetic energy of droplets, and Figure 5.9 shows the mean Sauter diameter. Comparing the mean kinetic energy of droplets in Figure 5.8, it is seen again that approach of "smoothed" micro-dynamics of blobs allows explicit improving of numerical predictions by both formulation of the drops statistical temperature, by (3.36) and (3.38). Making use (3.38), the better prediction is clearly seen for all experimental points: $y/D_l = 0.5$; 0.75; 1. Comparing the mean Sauter diameter in Figure 5.9, here again the prediction for $y/D_l = 0.5$ is not very good, except $3 < x/D_l < 5$ with (3.36). However along $y/D_l = 0.75$ and $y/D_l = 1$, the numerical results are close to measurements. One may conclude, that the composite immersed body approach, with stochastic models introduced in Chapter 3, allow to predict the typical size and velocity statistics of liquid relatively well in the near-to-injector region. The better prediction is obtained when (3.38) is used, and the initial spray angle is simulated by (3.29). Figures 5.10 and 5.11 confirm this conclusion. In 5.10, the mean diameter d_{10} is compared with measurements of Hong (2003), at $y/D_l = 1.5$ and $y/D_l = 0.5$, for different inlet velocities of the gas-stream, and for such injection velocities that the momentum ratio M holds the same magnitude: $M = 16$. Surprisingly, although the approach proposed is very simplified, and previous comparison was less successful namely on $y/D_l = 0.5$, it is seen that starting with significant gas-stream velocities $u_{g,0} > 40m/s$, the mean diameter is still relatively well predicted. The qualitative agreement with measurements is also seen for the mean Sauter diameter, shown in Figure 5.11. Both diameters, d_{10} and d_{32}, are decreasing significantly with increasing the inlet gas velocity, while the momentum ratio M holds the same magnitude.

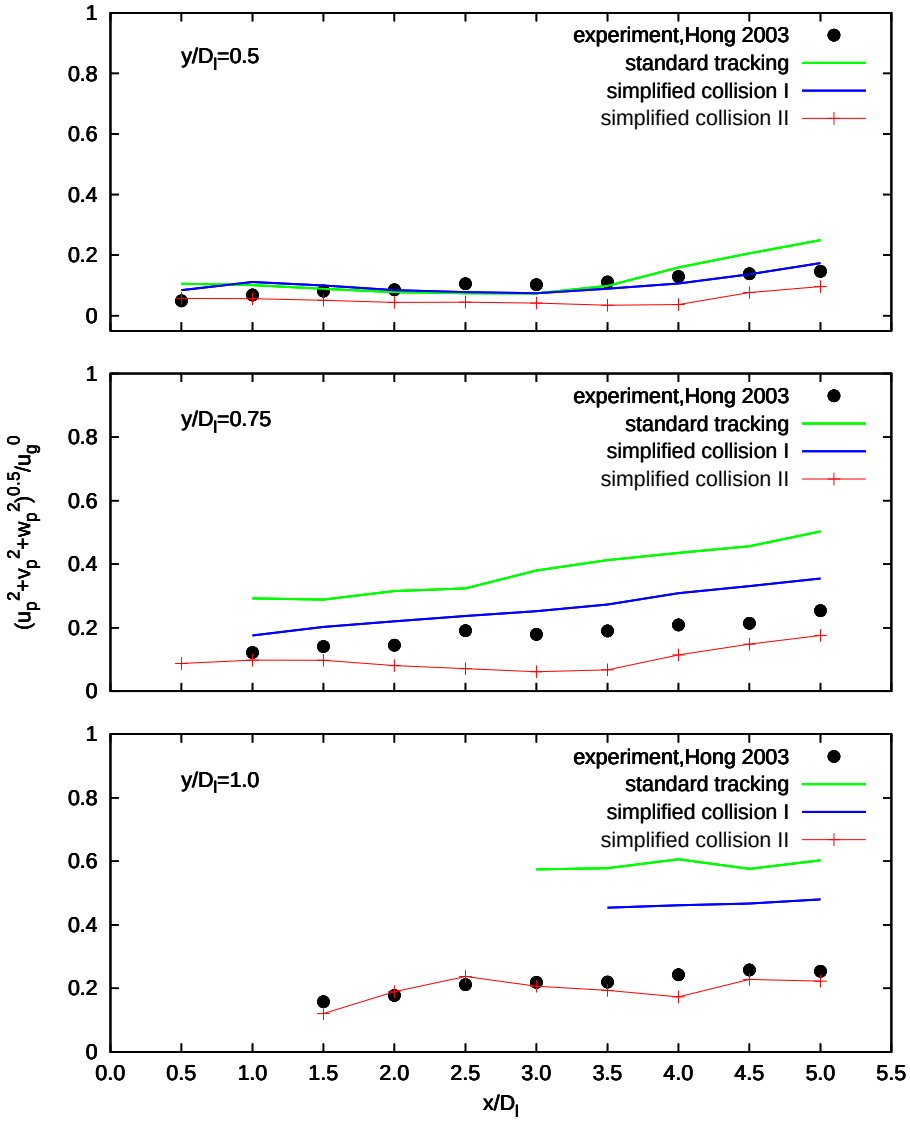

Figure 5.6: Comparison of velocity of droplets (presumed spray angle) with measurements (Hong, 2003) at different height's along the spray. Inlet parameters: $u_{g,0} = 60m/s$, $u_{l,0} = 0.52m/s$.

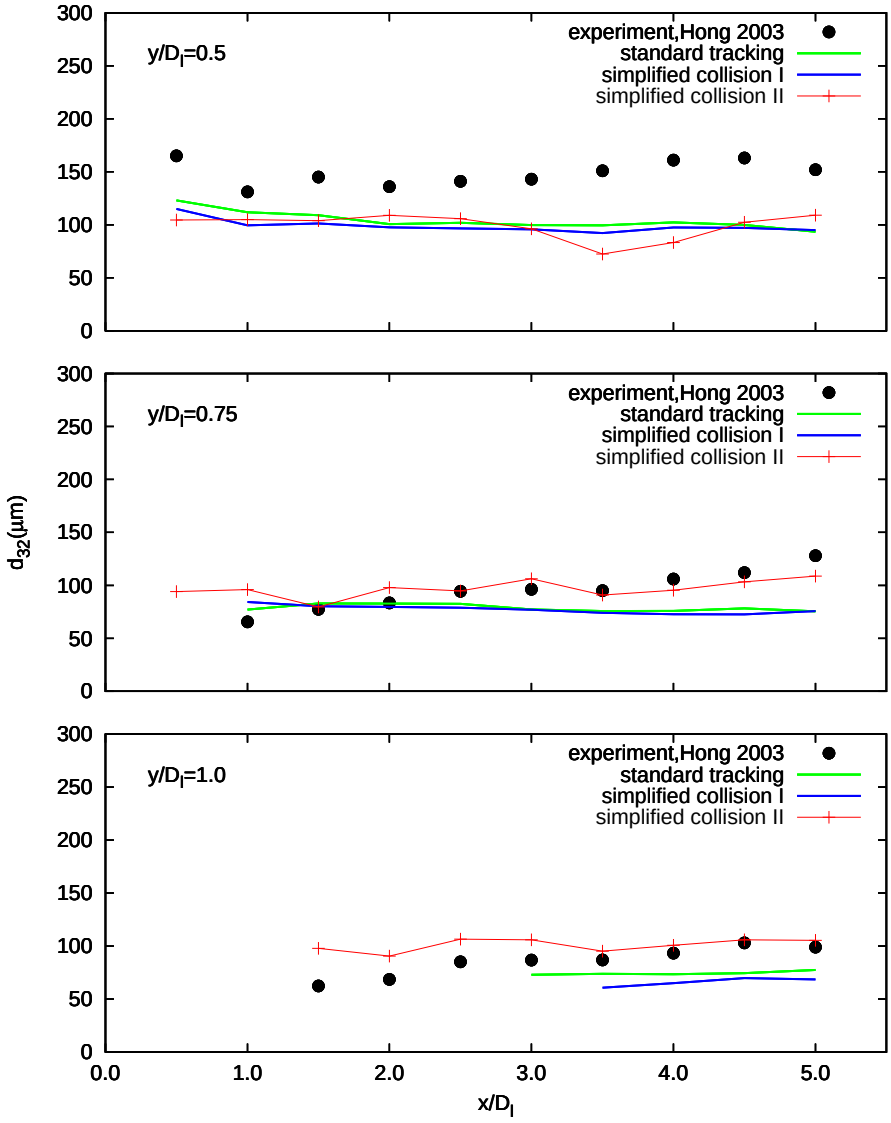

Figure 5.7: Comparison of mean Sauter diameter of produced droplets (presumed spray angle) with measurements (Hong, 2003) at different height's along the spray. Inlet parameters: $u_{g,0} = 60m/s$, $u_{l,0} = 0.52m/s$.

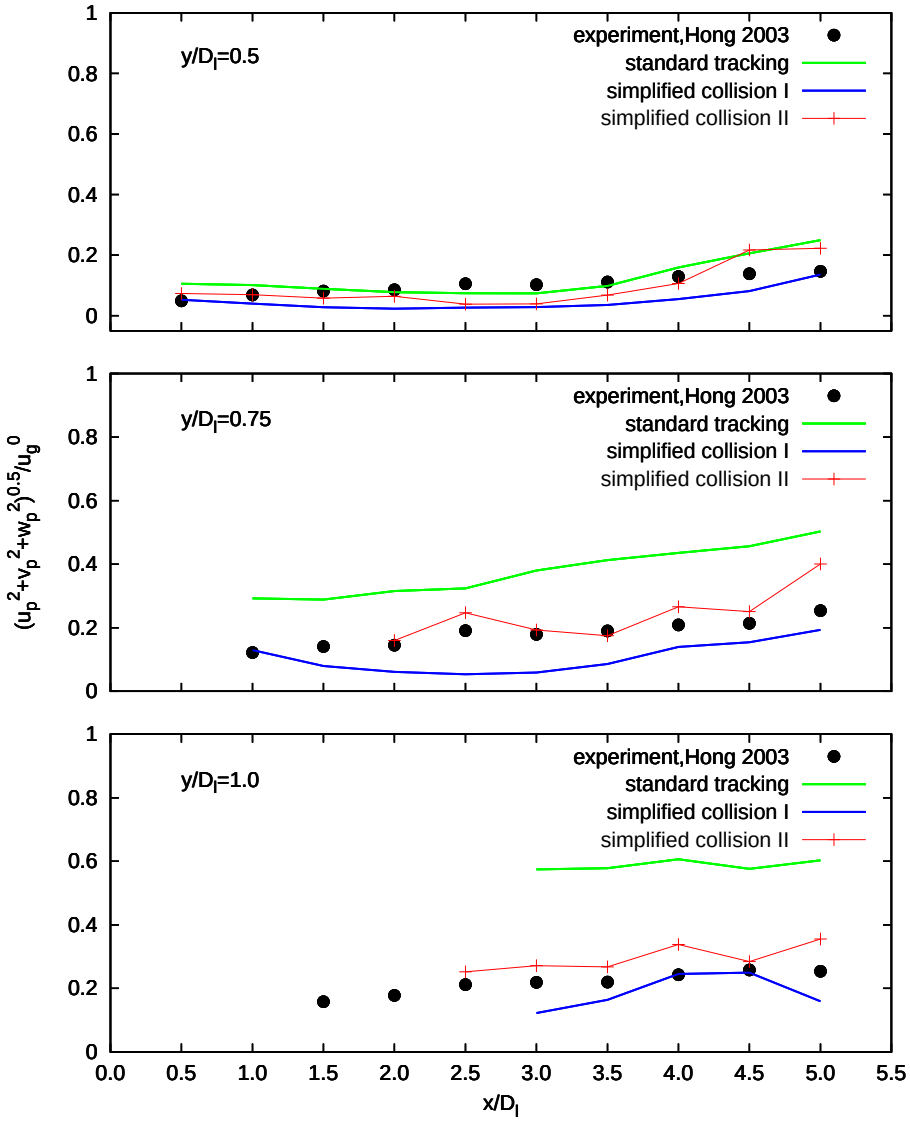

Figure 5.8: Comparison of velocity of droplets (simulated spray angle) with measurements (Hong, 2003) at different height's along the spray. Inlet parameters: $u_{g,0} = 60m/s$, $u_{l,0} = 0.52m/s$.

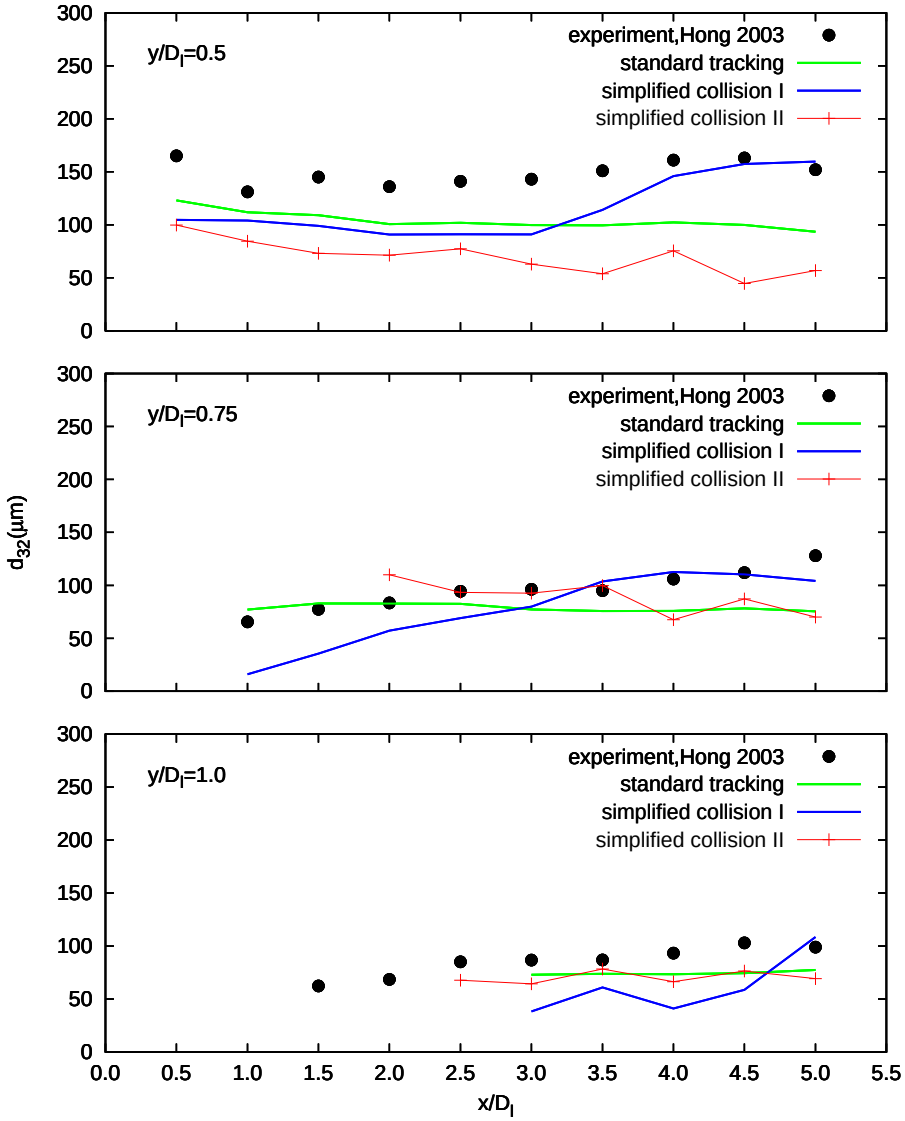

Figure 5.9: Comparison of mean Sauter diameter of produced droplets (simulated spray angle) with measurements (Hong, 2003) at different height's along the spray. Inlet parameters: $u_{g,0} = 60m/s$, $u_{l,0} = 0.52m/s$.

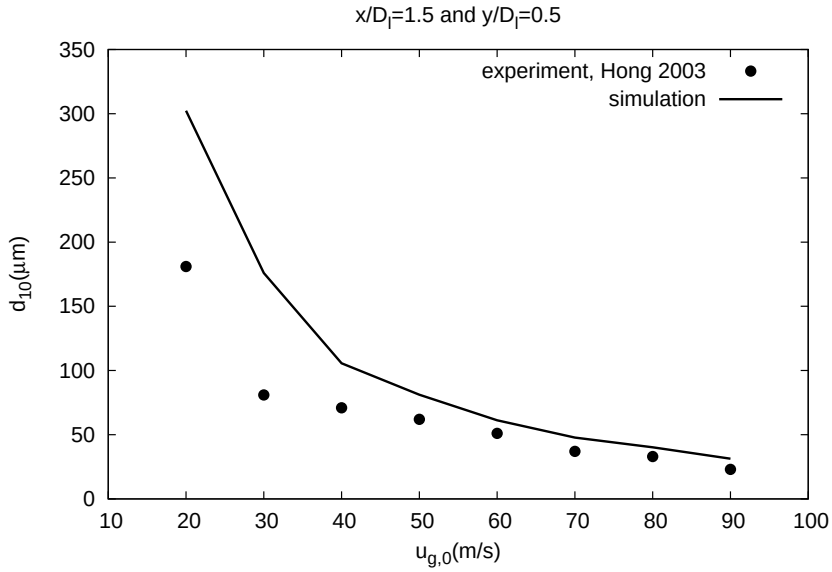

Figure 5.10: Comparison of mean diameter d_{10} at $x/D_l = 1.5$ and $y/D_l = 0.5$ ($M = 16$) with measurements (Hong, 2003).

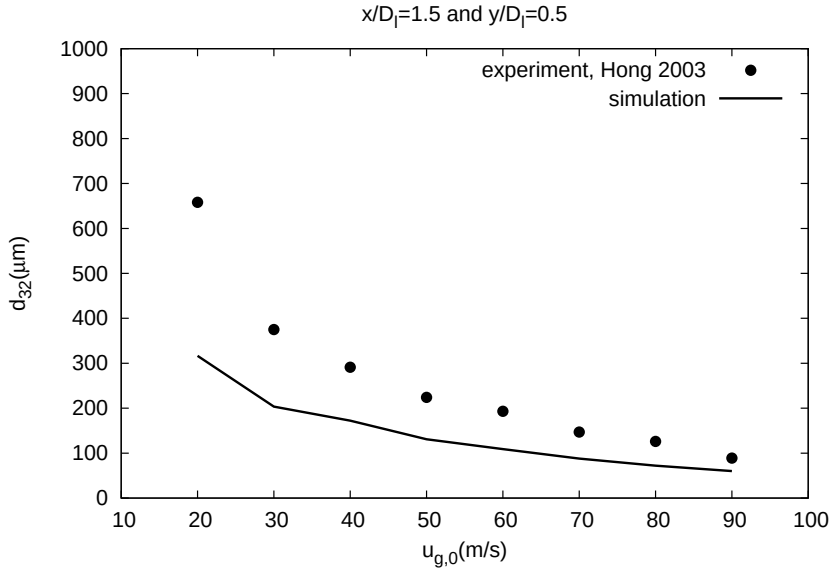

Figure 5.11: Comparison of mean Sauter diameter d_{32} at $x/D_l = 1.5$ and $y/D_l = 0.5$ ($M = 16$) with measurements (Hong, 2003).

5.3.1 Spray angle

The statistics of drop position and size allow computing spatial distribution of mean liquid volume fraction in the dispersed medium. The marginal level of this distribution say $X_l = 0.05$ may characterize the mean initial spray angle, resulting from simulation of initial orientation of primary produced blobs. Illustration is given in Figures 5.12 and 5.13 for two different values of the momentum ratio M: $M = 220$ and $M = 1200$. The gas velocity was taken the same for both momentum ratios and equal to $130 m/s$, while the liquid inlet velocity was changed according to the presumed magnitude of M. Angles calculated with the help of experimental expression (3.27), $\theta \approx [45° - 0.5 \arctan(\frac{M^{\frac{1}{2}}}{6})]$, and by our model (3.29), $\tan\theta = n_y \frac{u_{l,0}\sqrt{\rho_l/\rho_g}}{u_s}$, are indicated as well in these figures. The values are listed in Table 5.1. These values and simulations in figures show that increasing the momentum ratio leads to decreasing of the initial spray angle. This was observed experimentally in Lasheras & Hopfinger (2000), and Mansour & Chigier (1991). One would expect an inverse tendency in simulation of the initial spray angle: higher magnitude of M may result in stronger dispersion of detached drops, and thereby in bigger initial spray angle. However with higher magnitude of M, the liquid core becomes shorter. Then since drops are dragged by the high-speed stream, the opening angle of the spray is getting more confined by the gas flow. As illustration in Figure 5.14, we also compare measurements of the mean Sauter diameters by Hong 2003 with two computations: one using simulated angle (3.29), another one using sampling from experimental expression (3.27) for presumed initial angle. Both computations are based on expression (3.38) for statistical temperature of the drop. The results by presumed from experiment expression give slightly better agreement with measurement, although by both methods of initial spray angle simulation, the mean Sauter diameter is relatively well predicted.

5.4 Velocity profiles in the gas flow

In Figures 5.15 and 5.16 the profiles of mean filtered velocity and of its variance are plotted at different section for two different momentum ratio, $M = \rho_g u_{g,0}^2 / \rho_l u_{l,0}^2$,

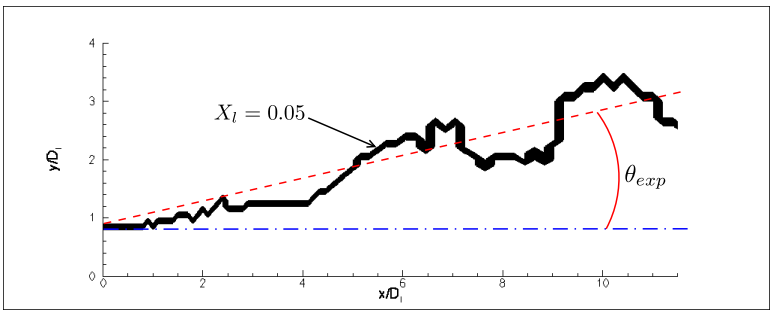

Figure 5.12: Comparison of spray angle with the expression (Lasheras & Hopfinger, 2000) ($M = 220$).

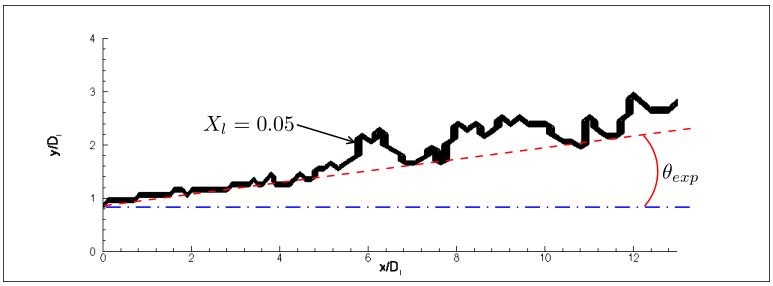

Figure 5.13: Comparison of spray angle with the expression (Lasheras & Hopfinger, 2000) ($M = 1200$).

Table 5.1: Spray angle obtained by the expressions and simulation.

$u_g(m/s)$	$u_l(m/s)$	M	θ (3.27)	$\bar{\theta}(simulation)$
130	0.3	220	11.01	8.53
130	0.13	1200	4.91	5.49

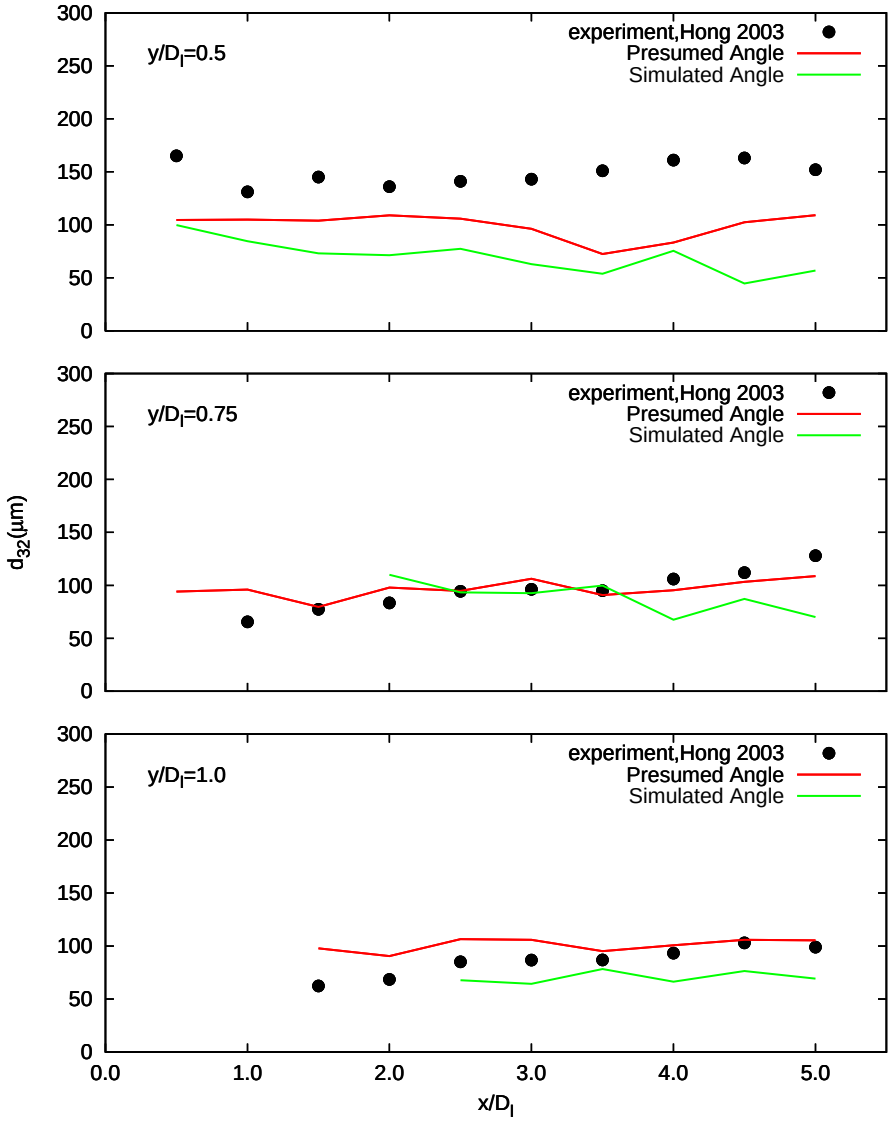

Figure 5.14: Comparison with measurements (Hong, 2003) of mean Sauter diameter of produced droplets; simulated and presumed initial spray angle; $u_{g,0} = 60m/s$, $u_{l,0} = 0.52m/s$.

$M = 70$ and $M = 220$ (same inlet gas-stream velocity, but different inlet velocity of the liquid). As it was mentioned in observation in Figures 5.2 to 5.5, it is seen in Figures 5.15 and 5.16 that with increasing momentum ratio M, the computed flow is characterized by larger gas flow jet around the liquid core and decreasing of the mean maximum of velocity (less steepened velocity gradients). This implies that greater M corresponds to stronger drag of the gas flow, with stronger cross-flow exchange of momentum, thereby simulating more intensive atomization process. This leads also slightly lower level of turbulent velocity fluctuation energy, when the momentum ratio is increased. One can also observe that displayed profiles may be not smooth (see $x/D_l = 2; 4$), as it would be in the case of one-phase jet flow. Such a "non-regularity" of the velocity profile, at $x/D_l = 2$ and $x/D_l = 4$, is difficult to interpret physically because of too complex interactions between phases in the considered flow. From other side, insufficiency of performed statistics, or numerical oscillations, may be the reason. This should be verified in the future work.

5.5 Conclusions

The main results of our simulations in this Chapter are as follows:

- The composite immersed body method (2.42) and (2.46) combined with stochastic models described in Chapter 3: (3.9)-(3.15), (3.22), (3.25) was assessed by comparison with measurements of Hong (2003) in his PhD. The results presented in Figures 5.6-5.11, 5.14 showed that stochastic models for liquid distribution closely to injector, and for the stochastic normal to interface, along with introduction of effective collision model (3.36) in motion of detached blobs, allow to predict relatively well statistics of velocity and size in the spray, as well as its initial opening angle.

- The simulation of flow in the vicinity of injector showed clearly the impact of liquid core on the gas flow, as a flapping zone of a dragged gas flow, with recirculation zone in front of the liquid core, with strong velocity gradients around the liquid core, and with large-scale vortical structures in the

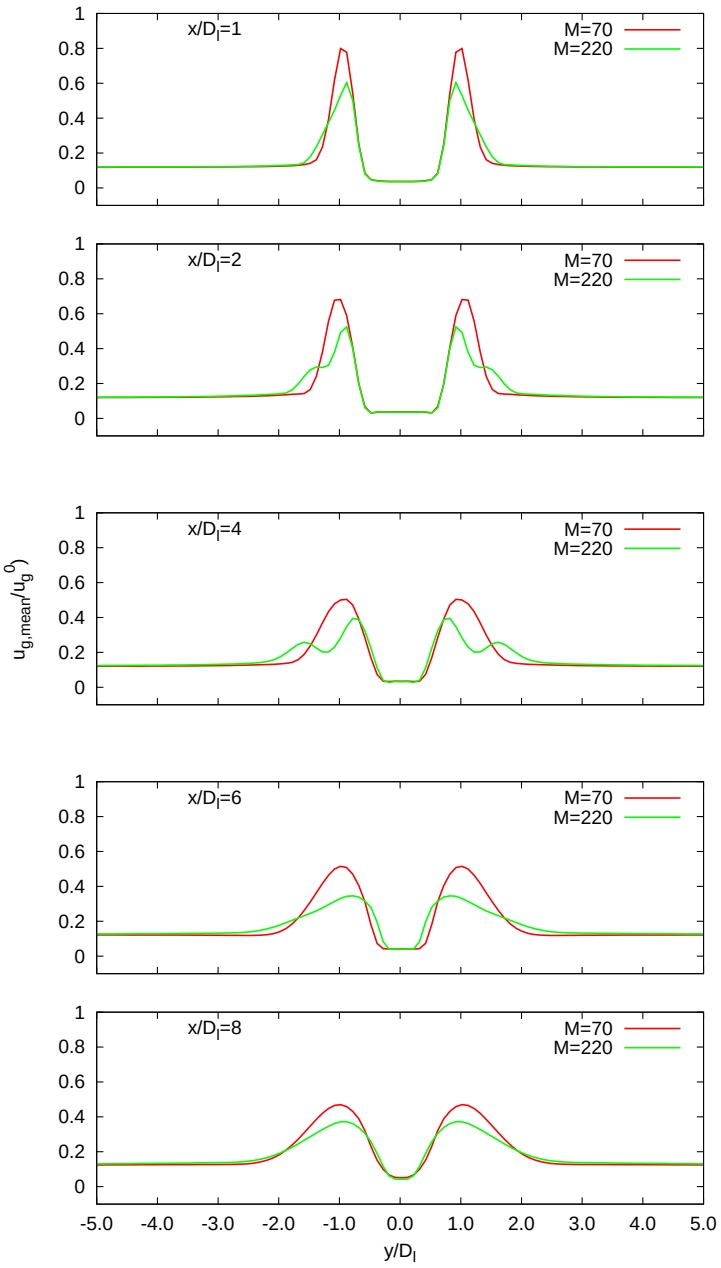

Figure 5.15: Comparison of mean velocity of gas u_{mean} at different sections between $M = 70$ and $M = 220$.

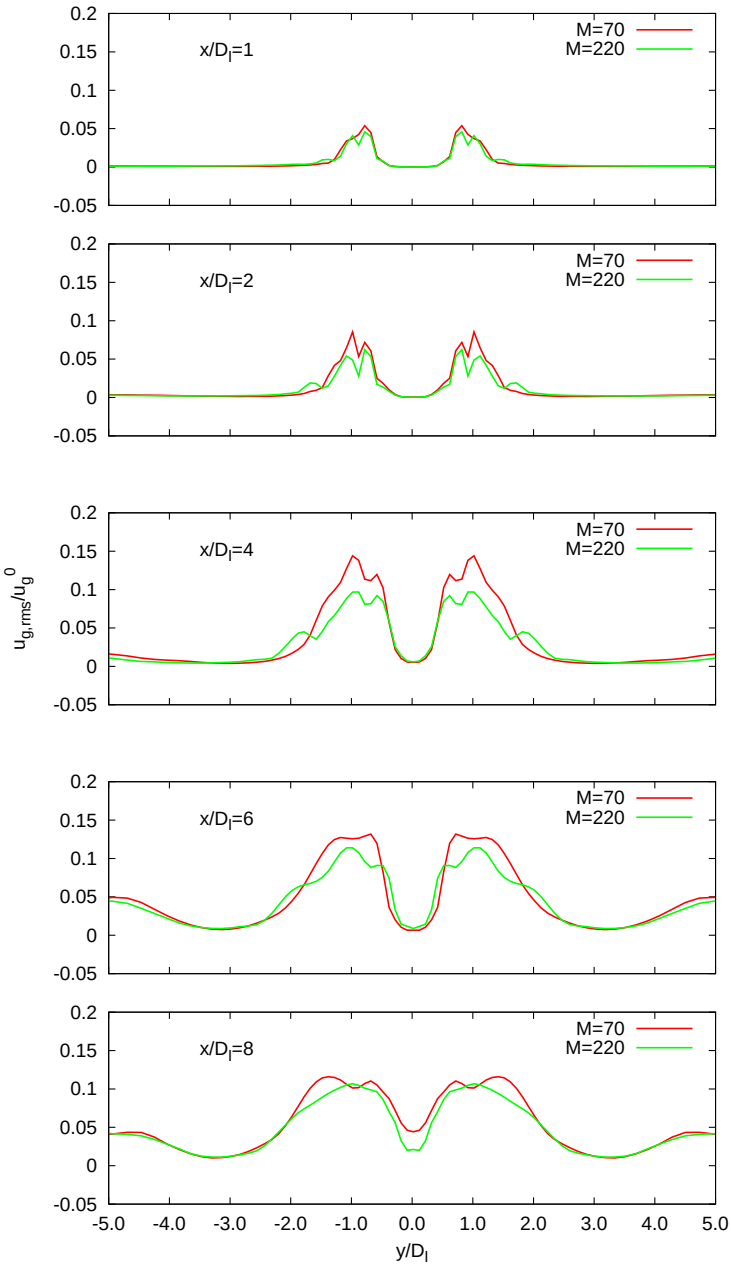

Figure 5.16: Comparison of root mean square velocity of gas u_{rms} at different sections between $M = 70$ and $M = 220$.

down-stream zone beyond the liquid core. The large spectrum of produced droplets, from $10\mu m$ to $200\mu m$, is obtained at each spray position.

- With increasing the momentum ratio, $M = \rho_g u_{g,0}^2 / \rho_l u_{l,0}^2$, the region closely to injector is populated mostly by smaller liquid elements (drops in our simulation). With increasing the momentum ratio M, the computed flow is characterized by larger jet flow, with less steepened velocity gradients around simulated liquid core. This implies that increased momentum ratio leads to stronger drag of the gas flow, with stronger cross-flow exchange of momentum, thereby simulating more intensive atomization process in model proposed.

- It was shown that with increasing the momentum ratio M , the initial spray angle may be reduced due shortening, in mean, the liquid core.

Chapter 6

Conclusion

In view of practical importance, this work is devoted to numerical simulation of spray formation in the vicinity of air-blast atomizer in conditions of experimental study performed in LEGI Grenoble during PHD of Hong (2003). The modern numerical approaches developed for two-phase flow simulation are described in Chapter 2. In this work, the numerical approach is new. This approach was described in Chapter 3, realized and assessed in Chapter 4 and Chapter 5. This approach is based on stochastic simulation, in which global parameters are presumed from the main physics of breakup suggested by experimental studies.

I. The main ideas of this approach are as follows.

In the close vicinity of air-blast atomizer, we consider a flowing turbulent connected media, with an immersed composite body. This immersed body is bordered by the fragmentation zone, and contains the connected (continuous) phase, and the not connected (dispersed) phase. In the composite immersed body, two processes are assumed to be fast comparing to the large (resolved) turbulent time-scale: it is the frequency of filament network formation, and the frequency of collisions between detached liquid elements. Another physical assumption is that the local acceleration/deceleration in the immersed composite body is controlled by its value on the interface. Then the connected phase is assumed to be governed by the filtered LES equations with the immerse body force:

$$\frac{\langle u_i\rangle^{n+1} - \langle u_i\rangle^n}{\Delta t} = \langle RHS_i\rangle + \langle F\rangle; \quad \frac{\partial\langle u_j\rangle}{\partial x_j} = 0$$

Here $\langle RHS_i \rangle = -\frac{\partial \langle u_i u_j \rangle}{\partial x_j} + \frac{1}{\rho_g} \frac{\partial \langle \sigma_{ij} \rangle}{\partial x_j}$, and

$$\langle F_i \rangle = \begin{cases} 0, & \text{if} \quad P_l = 0 \\ -\langle RHS_i \rangle + P_l \dot{U}_S n_i, & \text{if} \quad P_l \neq 0 \end{cases}$$

Three unknown variables are: (i) the probability to find the liquid in the vicinity of injector $P_l(\vec{x}, t)$; (ii) the outwards stochastic direction of interface $n_i(\vec{x}, t)$, which may be associated with the instantaneous curvature; (iii) the local magnitude of interface acceleration $\dot{U}_S(\vec{x}, t)$. The following stochastic models are proposed for modeling of those variables:

1. probability to find the liquid in the vicinity of injector $P_l(\vec{x}, t)$ is linked to the random configuration of the liquid core, and is simulated by spatial trajectories of specifically introduced stochastic particles. These particles are injected from the inlet orifice and are moving with the liquid flow, changing randomly their vertical position. The stochastic process is based on assumption that due to a high Weber number, the exiting continuous liquid jet is depleted in the framework of statistical universalities of a cascade fragmentation under scaling symmetry. The parameters of the stochastic process have been determined according to observations from Lasheras's, Hopfinger's and Villermaux's scientific groups.

2. to each injected flowing stochastic particle, we prescribe the outwards random direction of interface $n_i(\vec{x}, t)$. Its stochastic behavior is emulated by Brownian random walk on the surface of a unit radius sphere. The orientation of each flowing particle relaxes stochastically from streamwise/spanwise alignment (with random azimuth) to full isotropy. The diffusion coefficient of such a stochastic relaxation to isotropy is supposed to be inversely proportional to the life time of each injected particle, introduced from dimensional analysis, including dynamic pressures in inlet gas and liquid flows, the inertia of the jet characterized by liquid density, and the initial diameter of the jet.

3. local magnitude of interface acceleration $\dot{U}_S(\vec{x}, t)$ is computed by the local increment of the gaseous velocity relatively to the interface convection velocity, controlled here by inlet conditions.

In sub-region $0 < P_l < 1$, the primary blobs are sampled. These primary blobs constitute the dispersed phase. The mass is conserved from the inlet mass-flow to the global mass in dispersed phase. The motion equation for each primary drop is:

$$\frac{d\overline{v_{p,i}}}{dt} = \begin{cases} -\frac{\partial}{\partial x_i}(\frac{T_p}{m_p}) + \frac{\langle u_i \rangle - \overline{v_{p,i}}}{\tau_{st}} & \text{if} \quad P_l \neq 0 \\ \frac{\langle u_i \rangle - v_{p,i}}{\tau_{st}} & \text{if} \quad P_l = 0 \end{cases}$$

in which $v_{p,i}$ is the instantaneous component of the liquid drop velocity, while $\overline{v_{p,i}}$ is component of the liquid drop velocity but averaged over inter-drop collisions, T_p is the statistical temperature due to collisions. Several models for T_p were assessed. Two different stochastic processes defining $P_l(\vec{x}, t)$ and $n_i(\vec{x}, t)$ are supposed to be independent. The following model was retained:

$$\frac{T_p}{m_p} = \frac{1}{2}\nu_g(\frac{\partial \langle u_i \rangle}{\partial x_j} + \frac{\partial \langle u_j \rangle}{\partial x_i})^2 \tau_{st} \tag{6.1}$$

where τ_{st} is the Stokes time, m_p is the drop mass, and ν_g is the viscosity in the gas.

The composite immersed body method combined with stochastic models was assessed by comparison with measurements of Hong (2003). The results showed that statistics of the velocity and of the size in the spray at different distances from the center plane, at different distances from the nozzle orifice, at different inlet conditions (different gas velocity at constant momentum ratio $M = \rho_g u_{g,0}^2 / \rho_l u_{l,0}^2$, different momentum ratio M) have been predicted surprisingly well. The following observations are reported.

- The simulation of flow in the vicinity of injector showed clearly the impact of liquid core on the gas flow, as a flapping zone of a dragged gas flow, with recirculation zone in front of the liquid core, with strong velocity gradients around the liquid core, and with large-scale vortical structures in the down-stream zone beyond the liquid core. The large spectrum of produced droplets, from $10\mu m$ to $200\mu m$, is obtained at each spray position.

- With increasing the momentum ratio, M , the region closely to injector is populated mostly by smaller liquid elements (droplets in our simulation). With increasing the momentum ratio , the computed flow is characterized by larger zone of jet flow, with less steepened velocity gradients around simulated liquid core. This implies that increased momentum ratio leads to stronger drag of the gas flow, with stronger cross-flow exchange of momentum, thereby simulating more intensive atomization process in model proposed.

- It was also shown that with increasing the momentum ratio M, the initial spray angle may be reduced due shortening, in mean, the liquid core.

Appendix A

Kelvin-Helmholtz and Rayleigh-Taylor Instabilities

Most of the proposed models are based on instability analysis. The corresponding wave length is related to the drop diameter. Many successful descriptions were obtained with these methods, among them the most famous example is the fragmentation of a round liquid jet at low speed, known as the Rayleigh-Plateau instability (Plateau, 1873; Rayleigh, 1878). Various works repeat instability theory applied to fluid mechanics such as Chandrasekhar (1961).

In the case of a liquid / gas flow, it is assumed that there is a shift infinitesimal of the liquid / gas interface in the form:

$$\eta = \eta_0 \exp(i\underline{\omega}t - i\underline{k}z) \tag{A.1}$$

In this expression, η_0 is the amplitude of the initial disturbance. The quantities $\underline{\omega}$ and $\underline{k}$ are complex and are defined by

$$\begin{aligned} \underline{k} &= k + ik_i \\ \underline{\omega} &= \omega + i\omega_i \end{aligned} \tag{A.2}$$

The real parts are characteristic of the instabilities. k is the wave number and can be connected to the wavelength λ with $\lambda = 2\pi/k$ and ω is the pulse that

can be related to the frequency f. The imaginary parts describe the growth of disturbances for spatial k_i and for temporal w_i.

The infinitesimal displacement of the interface generates pressure disturbances and speed. These disturbances are analyzed in the form of waves characterized by $\underline{k}$ and $\underline{\omega}$. Depending on the chosen configuration, the movement equations can be written by introducing the infinitesimal perturbation for each variables. For example, if the speed is denoted u, it is expressed as:

$$\begin{aligned} u &= U + \delta u \\ \delta u &= \delta u_0 \exp(i\underline{\omega}t - i\underline{k}z) \end{aligned} \tag{A.3}$$

This provides a so called "dispersion relation" between $\underline{k}$ and $\underline{\omega}$. According to boundary conditions and configuration of the problem, this relationship takes different forms. For example, when it involves the surface tension, we use the Laplace relationship expressed on a surface dS by:

$$dP = \sigma(\frac{1}{R_1} + \frac{1}{R_2}) \tag{A.4}$$

where R_1 and R_2 are the two principal radius of curvature of the surface dS and dP is the difference in pressure on the interface.

There are so many ways to perform the stability analysis: either by studying the spatial growth of the disturbance, either by studying its growth time.

In many cases, it is not possible to consider that droplets are directly obtained through the first instability. To complete the description, subsequent instabilities have to be considered. According to the initial conditions of the problem, the dispersion equation takes different forms. This leads to instability of different types. For example, if $\delta\rho = 0$, it is called Kelvin-Helmholtz instability due to the relative motion in the same fluid. In case $\delta u = 0$, it is called Rayleigh-Taylor instability induced by the difference in mass volume between the two fluids or acceleration of one relative to another.

According to Chandrasekhar (1961), expanding the liquid-gas interfacial disturbance in Fourier modes as $\xi \sim \exp(ikx - i\omega t)$, the dispersion relation, neglecting gravity (high-Froude-number limit), is

$$(\rho_l + \rho_g)\frac{\omega}{k} = \rho_l u_l + \rho_g u_g \pm \sqrt{(\rho_l + \rho_g)\sigma k - \rho_l \rho_g (u_g - u_l)^2} \tag{A.5}$$

where σ stands for the surface tension of the liquid, ρ_l and ρ_g are the densities of liquid and gas, respectively, and u_g, u_l are the velocities of gas and liquid.

The flow is unstable when $\omega_i > 0$. There are several limiting cases:

Kelvin-Helmholtz instability

When $\Delta\rho \neq 0$, neglecting gravity and surface tension, $\sigma = 0$ and $g = 0$, the growth rate (A.6) is always positive regardless of the wavenumber k_r. The system is unstable since $\Delta u = u_g - u_l$ is large.

$$\omega_i = k_r \frac{\sqrt{\rho_g \rho_l}(u_g - u_l)}{\rho_g + \rho_l} \sim k_r \sqrt{\frac{\rho_g}{\rho_l}}(u_g - u_l) \quad \rho_g \ll \rho_l \tag{A.6}$$

Isodensity flow

Neglecting gravity and surface tension, $\Delta\rho = 0$, $g = 0$ and $\sigma = 0$, the system is unstable with temporal growth rate:

$$\omega_i = k_r \frac{u_g - u_l}{2} \tag{A.7}$$

Flows with different densities,considering gravity but neglecting sufrace tension

Neglecting only the surface tension effects, $\Delta\rho \neq 0$, $\sigma = 0$ and $g \neq 0$, the system is unstable for wavelengths less than $2\pi/k_{min}$, with k_{min} given by:

$$k_{min} = \frac{g(\rho_l^2 - \rho_g^2)}{\rho_l \rho_g (u_l + u_g)^2} \tag{A.8}$$

and the growth rate is

$$\omega_i = k_r \frac{\sqrt{\rho_g \rho_l}}{\rho_g + \rho_l}(u_g - u_l) \tag{A.9}$$

Flows with different densities, surface tension and considering gravity

In this situation, $\Delta\rho \neq 0$, $\sigma \neq 0$ and $g \neq 0$, the system is unstable when the wavelength is bigger than $2\pi/k_{max}$, k_{max} is given by:

$$k_{max} = \frac{\rho_l \rho_g (u_l + u_g)^2}{\sigma(\rho_l - \rho_g)} \tag{A.10}$$

Taking into account the gravity and surface tension, the system is stable as the difference of velocities $\Delta u = u_g - u_l$ is small:

$$\Delta u^2 \leq \frac{2g}{k_c} \frac{\rho_l^2 - \rho_g^2}{\rho_l \rho_g} \tag{A.11}$$

and the wave number k_c corresponding to the smallest difference of velocities Δu is as follows:

$$k_c = \frac{g(\rho_l - \rho_g)}{\sigma} \tag{A.12}$$

The classic linear stability analysis of the Rayleigh-Taylor problem, including the effects of surface tension (Chandrasekhar, 1961), yields the following expression for the wave with the maximal growth rate:

$$\lambda_{RT} = 2\pi \sqrt{\frac{3\sigma}{\rho_l a}} \tag{A.13}$$

where a is the acceleration of the liquid tongues.

Appendix B

Turbulence Modeling

Turbulent flows are governed by the Navier-Stokes equations. When the Reynolds number increases, the size of the small scales decreases. That brings up a problem. To solve the entire spectrum of turbulent scales, increasing Reynolds number requires computer power, proportional to the Reynolds number. Due to the wide range of scales in turbulent flows, averaging methods may be necessary if the computer power is insufficient. In the following, three different approaches are discussed.

B.1 Direct Numerical Simulation

In DNS, all the scales of the flow are resolved on spatial and temporal meshes and hence there is no need using any kind of closure approximation or turbulence model. The information obtained by such simulations is enormous and has led to understanding the turbulence physics and modeling issues with greater insight.

However, the Kolmogorov length- and time scales are resolved and that implies that the numerical (spatial) resolution is higher than that of the Kolmogorov length scale. The number of computational nodes N can be estimated by $N \sim (l/\eta)^3 \sim Re_T^{9/4}$. Further, since the time step size is proportional to the cell size (for equal Courant number), the required number of time steps also scales as $Re_T^{3/4}$. Thus, the computation time scales as Re_T^3. It is now possible to perform the Direct Numerical Simulation (DNS) of simple turbulent flows at moderate Reynolds numbers. The computational requirements for DNS of complex turbulent flows

at high Reynolds number are beyond the capabilities of supercomputers. In applications related to air-blast atomization, the Reynolds number is clearly too high for DNS. Moreover, most of the energy is contained in a few low wavenumber or frequency modes. Therefore, it is beneficial from computation cost as well as engineering point of view to resolve only the energy containing low wavenumbers or frequencies.

B.2 Reynolds-Averaged Navier-Stokes Approach

In the Reynolds-averaged Navier-Stokes (RANS) approach, the governing equations are *a priori* time- or ensemble-averaged. This has the advantage that time-averaged solutions can be computed fast. Since turbulence length scales are not resolved, the grid resolution is given by the length scales of the mean flow. As the governing equations are averaged, dynamic phenomena on time scales which are on the same order as turbulence time scales cannot be computed. Averaging also brings about the closure problem. New terms appear in the averaged momentum equations. The principal term, the Reynolds stresses τ_{ij}, arises from Reynolds-averaging the convective terms (B.1).

$$\tau_{ij} = -\overline{u_i' u_j'} \tag{B.1}$$

The correlations of fluctuation velocities are unknown and have to be closed. These models, as a rule, lack resolution information. The Navier-Stokes equations are not recovered as the resolution in space approaches zero. Hence, RANS modeling must be classified as a model, and not as an approximation. A widespread closure hypothesis is Boussinesqs hypothesis, an assumed analogy between molecular diffusion and turbulent diffusion. The viscosity is argued to depend on turbulence time scales and length scales which are computed from the solution of additional transport equations, e.g. for the turbulent kinetic energy and its dissipation rate. The Boussinesq hypothesis is not accurate for certain kind of flow, e.g. flow with streamline curvature, anisotropy, flow separation, unfavorable pressure gradient, system rotation (Wilcox, 1993).

For two-phases flows in air-blast atomization, one important deficiency of RANS models is that they are already conceptually not able to capture dynamic phenomena on turbulence time scales as time-averaged equations are solved.

B.3 Large Eddy Simulation

Direct Numerical Simulation of turbulent flows are inefficient and prohibitively expensive since a significant amount of computational resources is expended at capturing the small scale motions which contain negligible amount of turbulent kinetic energy. RANS modeling has several shortcomings. Large Eddy Simulation (LES) of turbulent flows is an approach intermediate to DNS and RANS and increasingly used as a tool for studying the dynamics of turbulence in engineering flows. In LES, the large scales that are dependent on the boundary conditions and contains most of the kinetic energy of the flow are simulated. The small scales or SubGrid Scales (SGS) are expected to be more universal and isotropic in nature. Since, the small scales are problem independent and contain small fraction of energy, modeling these scales would yield more universal and accurate turbulence models. To achieve decomposition in terms of resolved fields and subgrid fields, one generally applies a spatial filtering operation.

It was shown among others by Apte *et al.* (2003) that LES can be very promising in spray computation area. Very good agreement with experimental data regarding spray tip penetration was achieved. Study regarding turbulent mixing in diesel spray using LES by Kimura *et al.* (2004) also showed good agreement with experiment. One of the most useful publications concerning abilities of the LES model is by Sone & Menon (2003). In their work, LES scheme was implemented into the KIVA code along with sophisticated linear eddy model to account for subgrid mixing. Again, encouraging results were obtained. The field of the evaporated fuel was significantly less diffused than the one predicted by the reference RANS simulation. Although the work concentrated on spark ignition engines and the formulation was non-reacting, it nevertheless showed LES as a promising method for simulation of complex flows.

LES of turbulent flow can be split into four conceptual steps (Pope, 2000):

1. Spatial Filtering
2. Obtaining the filtered Navier-Stokes equations
3. Modeling the unresolved motions
4. Numerical solution

B.3.1 Spatial Filtering

At large Reynolds numbers, the turbulent flow might be visualized as a mean flow field superposed by fluctuations of different wavenumbers. Since the flow field can be expressed as the sum of contributions from fluctuations at all wavenumbers, large eddy motions can be defined to be the contributions from wavenumbers below a certain cut-off in the inertial subrange ('low-pass filtering'). This is accomplished through Spatial Filtering. Velocity can be decomposed between a spatially filtered contribution (denoted using an overbar) and a fluctuation about the spatially filtered value (denoted using a prime). For example,

$$u_i = \bar{u}_i + u_i' \tag{B.2}$$

For a field $\phi(x)$ defined in the domain $(-\infty, \infty)$, the filtered value is defined as (Ghosal & Moin, 1995):

$$\widetilde{\phi}(\mathbf{x}_0, t) = \int_{-\infty}^{\infty} G(\mathbf{x} - \mathbf{x}_0)\phi(\mathbf{x}, t)d\mathbf{x} \tag{B.3}$$

where G is the filter function satisfying the following properties:

1. $G(-x) = G(x)$;
2. $\int_{-\infty}^{+\infty} G(x)dx = 1.0$;
3. $G(x) \to 0$ as $|x| \to \infty$ sufficiently fast so that all moments $\int_{-\infty}^{+\infty} x^n dx (n \geq 0)$ exist;
4. $G(x)$ is localized (in some suitably defined sense) in $(-\frac{1}{2}, \frac{1}{2})$.

Three classical filters discussed most in existing literature are:

- **Box or Top-Hat Filter**

$$G(x) = \begin{cases} \frac{1}{\Delta} & \text{if} \quad |x| \leq \frac{\Delta}{2} \\ 0 & \text{otherwise} \end{cases} \tag{B.4}$$

- **Gaussian Filter**

$$G(x) = \sqrt{\frac{6}{\pi\Delta}} exp(-\frac{6x^2}{\Delta^2}) \tag{B.5}$$

- **Sharp Spectral Filter**

$$G(x) = \frac{\sin(\pi x/\Delta)}{\pi x} \tag{B.6}$$

Further discussion on various types of filters, and their performance is provided in (Pope, 2000; Piomelli, 1999; Germano, 1992).

B.3.2 Filtered Navier-Stokes Equations

In the LES procedure, after operation of filtering with function $G(x)$ (B.3)(In this thesis, the top-hat filter with a filter width $\Delta = 2h$ is used.), the numerical scheme is then responsible for solution of the filtered Navier-Stokes equations (2.42), with the unknown terms closed by subgrid modeling.

B.3.3 Subgrid Scale Models

The unresolved or subgrid scales affect the dynamics of the resolved flow filed through the subgrid stress (SGS) tensor q_{ij}. Usually the numerical grid is the only filter (an implicit filter), and hence the term SGS is appropriate. As in the RANS framework, a closure hypothesis has to be introduced. The modeling of the SGS tensor in the filtered equations and appropriate treatment of the source terms in the governing equations represent the most challenging and important task for LES. As the Reynolds number increases, the fraction of the total field that is unresolved also increases, the model is required to represent a larger range of turbulence scales, and the accuracy of a simulation becomes more sensitive to the quality of the SGS model.

Smagorinsky Model

The Smagorinsky model (Smagorinsky, 1963) is an eddy-viscosity type model given by:

$$q_{ij} - \frac{1}{3}q_{ll}\delta_{ij} = -C_s^2\Delta^2|\overline{S}|\overline{S_{ij}} \quad \text{with} \quad |\overline{S}|^2 = \frac{1}{2}\overline{S_{pq}S_{pq}} \tag{B.7a}$$

$$S_{ij} = \frac{1}{2}(\frac{\partial u_i}{\partial x_j} + \frac{\partial u_j}{\partial x_i}) - \frac{1}{3}\frac{\partial u_l}{\partial x_l}\delta_{ij} \tag{B.7b}$$

S_{ij} is the deviatoric part of the rate of strain tensor. The constant C_s depends on the particular flow and different values have been proposed. Although simple, the Smagorinsky model is known to be excessively dissipative in transitional flows as well as flows with strong coherent structures and to have poor correlation with the exact subgrid stress tensor in a priori studies. The gradient of the term, $q_{ll}\delta_{ij}/3$, is absorbed in the pressure gradient for incompressible flows.

Dynamic Smagorinsky Model

Dynamic Smagorinsky Model which has been used in this thesis is a modification of the Smagorinsky model. It has been proposed by Germano *et al.* (1991) to correct the excessive dissipation of this model and avoid *ad hoc* flow-dependent changes to the coefficient. The square of the constant C_s^2 is replaced by a coefficient C_d which is dynamically computed and depends on the local structure of the flow. The Smagorinsky eddy-viscosity formulation is retained:

$$q_{ll} - \frac{1}{3}q_{ll}\delta_{ij} = -C_d\Delta^2|\overline{S}|\overline{S_{ij}} \tag{B.8}$$

In order to compute C_d, a test filter, denoted by a hat and corresponding to a filter width larger than that of the LES, is introduced. The consecutive $\hat{\Delta}$ application of these two filters defines a filter with a filter width of $\kappa\Delta$. For the top-hat filter, the optimum value $\kappa = \sqrt{5}$, which corresponds to a test filter width of 2Δ, was found in a recent study of the mixing layer (Vreman *et al.*, 1996) The dynamic constant is calculated with a least squares approach according to:

$$C_d = \frac{< M_{ij}L_{ij} >}{< M_{ij}M_{ij} >} \tag{B.9a}$$

$$L_{ij} = \widehat{\overline{u}_i\overline{u}_j} - \widehat{\overline{u}}_i\widehat{\overline{u}}_j \tag{B.9b}$$

$$M_{ij} = -(\kappa\Delta)^2|\widehat{\widetilde{S}}|\widehat{\widetilde{S_{ij}}} + \Delta^2\widehat{|\widetilde{S}|\widetilde{S_{ij}}} \tag{B.9c}$$

To prevent numerical instability caused by negative values of C_d, the numerator and denominator are averaged in the homogeneous directions. The constant C_d is artificially set to zero during the few instances when it is still negative.

Appendix C

Turbulence Scales

Turbulent flows are characterized by a wide range of length scales due to eddies of different sizes. These characteristic scales interact in complex ways, governed by the Navier-Stokes equations. The energy spectrum (Figure C.1) shows the distribution of kinetic energy over the wavenumber of these eddies for a fully developed turbulent flow. The various wavenumbers in the energy spectrum can be divided with respect to their sizes. The large-scale eddies are driven by characteristic velocity and length scales of the flow field, and hence are heavily influenced in character by the details of the flow field. The spatial scales of the largest eddies are limited by the flow geometry (diameter of a tube, the thickness of the boundary layer, the thickness of a jet ...). Those large eddies contain most of the kinetic energy. The other part of the spectrum can be subdivided into inertial subrange and dissipation subrange, depending on whether inertial or dissipative effects are dominant. The dimension of the smallest eddies is typically related to viscous dissipation of kinetic energy into thermal energy of molecules. The smaller eddies make up the universal equilibrium range which is according to Kolmogorov (Kolmogorov, 1941) hypotheses statistically similar or universal for all high Reynolds number flows. In the view of the energy cascade, energy is continuously transfered from large to small eddies where it is dissipated. The inertial range is in equilibrium as the energy transfer from large to small eddies is thought to be independent of the scale of the eddy, i.e. the energy flux from the large eddies equals the energy flux to the small eddies for any particular eddy size in this range. It follows that there exist a range of length scales that are much larger

than the smallest scales, but small in comparison to the largest scales. In this zone, the statistics of motion are unaffected by the details of the flow field (unlike the large-scale motions) and the coefficient of viscosity (unlike the small-scale motions). They only depend on the dissipation of energy ϵ that determines the energy transfer across these scales (Kolmogorov, 1941). The energy of motions in the Inertial Subrange is shown in Figure C.1 and can be expressed as (C.1) where k is the wavenumber associated with a length scale in this range, and $E(k)$ is the turbulent kinetic energy at that length scale.

$$E(k) \propto \epsilon^{2/3} k^{-5/3} \tag{C.1}$$

Two important ranges of scales have emerged in the discussion about turbulence: the integral scales and the Kolmogorov scales. The largest eddies are of the size of the integral length scale, and the smallest eddies are of the size of the Kolmogorov length scales.

The mean distance for which the velocity fluctuations are correlated gives an estimate for the integral length scales. The autocorrelation function $R_{u'u'}$ is:

$$R_{u'u'}(r, x) = \frac{\overline{u'(x)u'(x+r)}}{\overline{u'(x)u'(x)}} \tag{C.2}$$

where $u'(x)$ is the velocity fluctuation at point x, $u'(x+r)$ is the velocity fluctuation at a distance r from x. The overbar represents a time-average. The integral length scales l_0 can be estimated as:

$$l_0 = \int_0^\infty R_{u'u'}(r) dr \tag{C.3}$$

The autocorrelation function and an estimate for the integral length scale are plotted in Figure C.2. The integral velocity scale u'_0 can be estimated as the RMS of u. The integral time scale τ_0 is then:

$$\tau_0 = \frac{l_0}{u'_0} \tag{C.4}$$

A turbulence Reynolds number Re_T is defined based on the integral scales:

$$Re_T = \frac{u'_0 l_0}{\nu} \tag{C.5}$$

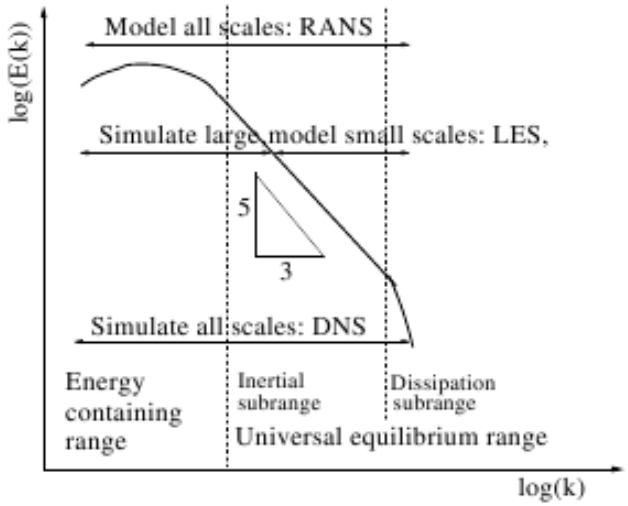

Figure C.1: Energy Spectrum in a turbulent flow.

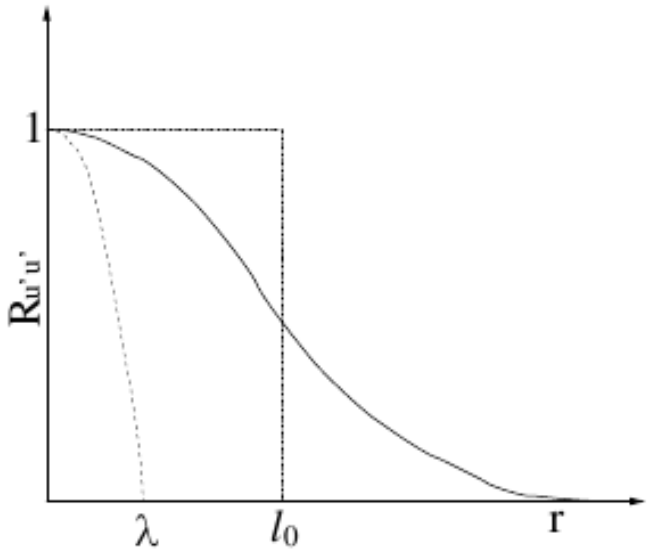

Figure C.2: Autocorrelation Function over the distance.

The integral length and velocity scales are on the same order of magnitude as the characteristic length and velocity scales of the particular problem (or somewhat less), and therefore the turbulence Reynolds number Re_T is large if the Reynolds number is large.

The smallest scales are the Kolmogorov scales. According to Kolmogorovs first hypothesis, if the turbulence Reynolds number is large, they only depend on dissipation ϵ and viscosity ν. The dimensions of ϵ and ν are m^2s^{-3} and m^2s^{-1}. The only possible combinations which have the dimensions of length, time, and velocity are, respectively:

$$\eta \sim (\frac{\nu^3}{\epsilon})^{\frac{1}{4}} \tag{C.6a}$$

$$\tau_\eta \sim (\frac{\nu}{\epsilon})^{\frac{1}{2}} \tag{C.6b}$$

$$u_\eta \sim (\nu\epsilon)^{\frac{1}{4}} \tag{C.6c}$$

They represent the Kolmogorov length scale η, the Kolmogorov time scale τ_η, and the Kolmogorov velocity scale u_η. It follows immediately that the Reynolds number based on the Kolmogorov scales is on the order of unity:

$$Re_\eta = \frac{u_\eta \eta}{\nu} \sim 1 \tag{C.7}$$

Appendix D

Compact Schemes

D.1 Compact scheme on uniform meshes

Lele (1992) proposed a generalization of the classical Pade schemes. The schemes discussed in Lele (1992) represent a family of high-order finite difference compact schemes, which can be used not only for the evaluation of derivatives, but also for filtering and interpolation applications. Algorithms based on such schemes can provide numerical solutions with spectral-like resolution and very low numerical dissipation.

Consider a one-dimensional mesh with node coordinates x_i, where $1 \leq i \leq N$ is the node index, and a function with given values $\phi_i = \phi(x_i)$ at the nodes. A uniform mesh with equal nodes spacings $h = x_i - x_{i-1}$ will first be considered. A sixth-order tridiagonal approximation ϕ'_i of the first derivative $(\frac{d\phi}{dx})_{x_i}$ can then be obtained:

$$\frac{1}{3}\phi'_{i-1} + \phi'_i + \frac{1}{3}\phi'_{i+1} = \frac{14}{9}\frac{\phi_{i+1} - \phi_{i-1}}{2h} + \frac{1}{9}\frac{\phi_{i+2} - \phi_{i-2}}{4h} \tag{D.1}$$

Similarly, a sixth-order tridiagonal approximation ϕ''_i of the second derivative $(\frac{d^2\phi}{dx^2})_{x_i}$ is given by

$$\frac{2}{11}\phi''_{i-1} + \phi''_i + \frac{2}{11}\phi''_{i+1} = \frac{12}{11}\frac{\phi_{i+1} - 2\phi_i + \phi_{i-1}}{h^2} + \frac{3}{11}\frac{\phi_{i+2} - 2\phi_i + \phi_{i-2}}{4h^2} \tag{D.2}$$

For non-periodic boundary problems, non-centered boundary schemes are required at points close to the boundaries, i.e. at nodes 1, 2, $N1$ and N. Classical

fourth-order Pade schemes and third-order compact relations can be used respectively, at nodes 2 and $N1$ and at nodes 1 and N for both derivatives. In practice, the boundary formulation at nodes 1 and 2 for the first derivative is given by:

$$i = 1, \quad \phi_1\prime + 2\phi_2' = \frac{1}{h}(-\frac{5}{2}\phi_1 + 2\phi_2 + \frac{1}{2}\phi_3) \tag{D.3a}$$

$$i = 2, \quad \frac{1}{4}\phi_1' + \phi_2' + \frac{1}{4}\phi_3' = \frac{3}{4h}(\phi_3 - \phi_1) \tag{D.3b}$$

with similar relations at nodes $N1$ and N; while the boundary formulation for the second derivative is taken under the form:

$$i = 1, \quad \phi_1'' + 11\phi_2'' = \frac{1}{h^2}(13\phi_1 - 27\phi_2 + 15\phi_3 - \phi_4) \tag{D.4a}$$

$$i = 2, \quad \frac{1}{10}\phi_1'' + \phi_2'' + \frac{1}{10}\phi_3'' = \frac{6}{5h^2}(\phi_3 - 2\phi_2 + \phi_1) \tag{D.4b}$$

with similar relations at nodes $N1$ and N.

D.2 Compact scheme on non-uniform meshes

The main constraint imposed is that the obtained scheme for non-uniform meshes must reduce exactly to the scheme for uniform meshes, in the case of a uniformly spaced grid.

For an irregular mesh, the approximation to the first derivative may be rewritten in a more general way

$$\alpha_i\phi_{i-2}' + \phi_i' + \beta_i\phi_{i+1}' = A_i\phi_{i+1} + B_i\phi_{i-1} + C_i\phi_{i+2} + D_i\phi_{i-2} + E_i\phi_i \tag{D.5}$$

where the coefficients α_i, β_i, A_i, B_i, C_i, D_i and E_i are functions of the non-uniform mesh spacings $h_k = x_k - x_{k-1}$. Following Lele (1992), relations between the former coefficients can be derived by matching the Taylor series of various orders. All derivatives are linearly independent. The leading-order truncation error of the resulting scheme is determined by the first unmatched coefficient in the Taylor series. Here, the following relations are obtained:

$$
\begin{aligned}
A_i + B_i + C_i + D_i + E_i &= 0 && \text{(order0)}\\
h_{i+1}A_i - h_iB_i + (h_{i+2}+h_{i+1})C_i - (h_i+h_{i-1})D_i &= 1+\alpha_i+\beta_i && \text{(order1)}\\
h_{i+1}^2A_i + h_i^2B_i + (h_{i+2}+h_{i+1})^2C_i + (h_i+h_{i-1})^2D_i &= \frac{2!}{1!}(h_{i+1}\beta_i - h_i\alpha_i) && \text{(order2)}\\
h_{i+1}^3A_i - h_i^3B_i + (h_{i+2}+h_{i+1})^3C_i - (h_i+h_{i-1})^3D_i &= \frac{3!}{2!}(h_{i+1}^2\beta_i - h_i^2\alpha_i) && \text{(order3)}\\
h_{i+1}^4A_i + h_i^4B_i + (h_{i+2}+h_{i+1})^4C_i + (h_i+h_{i-1})^4D_i &= \frac{4!}{3!}(h_{i+1}^3\beta_i - h_i^3\alpha_i) && \text{(order4)}\\
h_{i+1}^5A_i - h_i^5B_i + (h_{i+2}+h_{i+1})^5C_i - (h_i+h_{i-1})^5D_i &= \frac{5!}{4!}(h_{i+1}^4\beta_i - h_i^4\alpha_i) && \text{(order5)}\\
h_{i+1}^6A_i + h_i^6B_i + (h_{i+2}+h_{i+1})^6C_i + (h_i+h_{i-1})^6D_i &= \frac{6!}{5!}(h_{i+1}^5\beta_i - h_i^5\alpha_i) && \text{(order6)}
\end{aligned}
\tag{D.6}
$$

For non-periodic boundaries, Equation (D.5) can no longer be applied to points close to the boundary, so that boundary schemes at nodes 1, 2, $N1$ and N are required. The first derivative at boundary point $i = 1$ is calculated from:

$$\phi_1' + \alpha\phi_2' = A\phi_1 + B\phi_2 + C\phi_3 \tag{D.7}$$

This relation can formally be third-order. A solution in terms of α, A, B and C is shown in Appendix F. At boundary point $i = 2$, the first derivative is obtained from the relation:

$$\alpha\phi_1' + \phi_2' + \beta\phi_3' = A\phi_1 + B\phi_2 + C\phi_3 \tag{D.8}$$

This relation can formally be fourth-order. The solution coefficients are shown in Appendix F.

Similarly, the approximation to the second derivative is rewritten under the form:

$$\alpha_i\phi_{i-2}'' + \phi_i'' + \beta_i\phi_{i+1}'' = A_i\phi_{i+1} + B_i\phi_{i-1} + C_i\phi_{i+2} + D_i\phi_{i-2} + E_i\phi_i \tag{D.9}$$

Matching the Taylor series coefficients, the second set of unknowns α_i, β_i, A_i, B_i, C_i, D_i and E_i are the solution of the system:

$$
\begin{aligned}
A_i + B_i + C_i + D_i + E_i &= 0 && \text{(order0)}\\
h_{i+1}A_i - h_iB_i + (h_{i+2}+h_{i+1})C_i - (h_i+h_{i-1})D_i &= 0 && \text{(order1)}\\
h_{i+1}^2A_i + h_i^2B_i + (h_{i+2}+h_{i+1})^2C_i + (h_i+h_{i-1})^2D_i &= \frac{2!}{0!}(1+\beta_i+\alpha_i+\beta_i) && \text{(order2)}\\
h_{i+1}^3A_i - h_i^3B_i + (h_{i+2}+h_{i+1})^3C_i - (h_i+h_{i-1})^3D_i &= \frac{3!}{1!}(h_{i+1}\beta_i - h_i\alpha_i) && \text{(order3)}\\
h_{i+1}^4A_i + h_i^4B_i + (h_{i+2}+h_{i+1})^4C_i + (h_i+h_{i-1})^4D_i &= \frac{4!}{2!}(h_{i+1}^2\beta_i - h_i^2\alpha_i) && \text{(order4)}\\
h_{i+1}^5A_i - h_i^5B_i + (h_{i+2}+h_{i+1})^5C_i - (h_i+h_{i-1})^5D_i &= \frac{5!}{3!}(h_{i+1}^3\beta_i - h_i^3\alpha_i) && \text{(order5)}\\
h_{i+1}^6A_i + h_i^6B_i + (h_{i+2}+h_{i+1})^6C_i + (h_i+h_{i-1})^6D_i &= \frac{6!}{4!}(h_{i+1}^4\beta_i - h_i^4\alpha_i) && \text{(order6)}
\end{aligned}
\tag{D.10}
$$

Here, it was decided to limit this thesis to a third-order scheme. The general solution shown in Appendix E is given in terms of a linear system of the five first equations in (D.10), where A_i, B_i, C_i, D_i and E_i are the unknowns. As in the first derivative case, the parameters α_i and β_i are considered constants, equal to their value for uniform meshes, i.e. $\alpha_i = \beta_i = 2/11$. The final scheme for the second derivative will reduce exactly to the scheme given by Equation (D.2), for uniformly spaced grids. The leading truncation error term for the second derivative approximation can formally be written as:

$$
\epsilon_1 = [h_{i+1}^5A_i - h_i^5B_i + (h_{i+2}+h_{i+1})^5C_i - (h_i+h_{i-1})^5D_i - \frac{5!}{3!}(h_{i+1}^4\beta_i - h_i^4\alpha_i)]\frac{\phi_i^{(V)}}{5!} \tag{D.11}
$$

and is of order $O(h_i^3)$.

For non-periodic boundaries, Equation (D.9) is no longer valid at nodes 1, 2, $N1$ and N. The second derivative at boundary point $i = 1$ is then calculated from:

$$
\phi_1' + \alpha\phi_2' = A\phi_1 + B\phi_2 + C\phi_3 + D\phi_4 \tag{D.12}
$$

If α is considered a parameter, this relation can formally be second-order. Solutions for A, B, C, D are shown in Appendix F. At boundary point $i = 2$, the second derivative is obtained from the relation:

$$\alpha\phi'_1 + \phi'_2 + \beta\phi'_3 = A\phi_1 + B\phi_2 + C\phi_3 + D\phi_4 \tag{D.13}$$

If α and β are considered parameters, this relation can formally be second-order. Solutions for A, B, C, D are shown in Appendix F. In this thesis, in order to damp the high wave number spurious oscillations created at the boundaries, a fourth-order nonuniform compact filter is applied to the field at each iteration. The solution is then given in terms of a linear system of the first five equations in (D.6), where A_i, B_i, C_i, D_i and E_i are the unknowns. This leads to the general expressions shown in Appendix E. In these expressions, the right-hand side parameters α_i and β_i are considered constants, equal to their value for uniform meshes, i.e. $\alpha_i = \beta_i = 1/3$. For grids where the spacing does not vary smoothly, fourth-order accuracy will still be obtained. The leading truncation error term can formally be written as:

$$\epsilon_1 = [h_{i+1}^5 A_i - h_i^5 B_i + (h_{i+2} + h_{i+1})^5 C_i - (h_i + h_{i-1})^5 D_i - \frac{5!}{4!}(h_{i+1}^4 \beta_i - h_i^4 \alpha_i)]\frac{\phi_i^{(V)}}{5!} \tag{D.14}$$

and is of the order $O(h_i^4)$. The parameter α of the filter is optimized in order to keep the influence of the filter as weak as possible and is set equal to 0.4983. The value $\alpha = 0.5$ corresponds to no filtering. The resulting scheme has overall fourth-order spatial accuracy on stretched grids.

Appendix E

Approximation of Derivatives

The general solution for fourth-order, first derivative scheme on non-uniform meshes, with α_i and β_i parameters, is given by:

$$A_i = \frac{\begin{bmatrix} h_{i-1}h_ih_{i+1} + h_i^2h_{i+1} + h_{i-1}h_ih_{i+2} + h_i^2h_{i+2} - h_{i-1}h_i^2\alpha_i - h_{i-1}h_ih_{i+1}\alpha_i \\ -h_{i-1}h_ih_{i+2}\alpha_i - h_{i-1}h_ih_{i+1}\beta_i - h_i^2h_{i+1}\beta_i - h_{i-1}h_{i+1}^2\beta_i - 2h_ih_{i+1}^2\beta_i - h_{i+1}^3\beta_i \\ h_{i-1}h_ih_{i+2}\beta_i + h_i^2h_{i+2}\beta i + 2h_{i-1}h_{i+1}h_{i+2}\beta_i + 4h_ih_{i+1}h_{i+2}\beta_i + 3h_{i+1}^2h_{i+2}\beta_i \end{bmatrix}}{h_{i+1}(h_i + h_{i+1})(h_{i-1} + h_i + h_{i+1})h_{i+2}} \tag{E.1}$$

$$B_i = \frac{\begin{bmatrix} -h_{i-1}h_{i+1}^2 - h_ih_{i+1}^2 - h_{i-1}h_{i+1}h_{i+2} - h_ih_{i+1}h_{i+2} - 3h_{i-1}h_i^2\alpha_i - 4h_{i-1}h_ih_{i+1}\alpha_i \\ h_i^3\alpha_i + 2h_i^2h_{i+1}\alpha_i - h_{i-1}h_{i+1}^2\alpha_i + h_ih_{i+1}^2\alpha_i - 2h_{i-1}h_ih_{i+2}\alpha_i - h_{i-1}h_{i+1}h_{i+2}\alpha_i \\ h_i^2h_{i+2}\alpha_i + h_ih_{i+1}h_{i+2}\alpha_i + h_{i-1}h_{i+1}h_{i+2}\beta_i + h_ih_{i+1}h_{i+2}\beta_i + h_{i+1}^2h_{i+2}\beta_i \end{bmatrix}}{h_{i-1}h_i(h_i + h_{i+1})(h_i + h_{i+1} + h_{i+2})} \tag{E.2}$$

$$C_i = \frac{\begin{bmatrix} -h_{i-1}h_ih_{i+1} - h_i^2h_{i+1} + h_{i-1}h_i^2\alpha_i + h_{i-1}h_ih_{i+1}\alpha_i + h_{i-1}h_ih_{i+1}\beta_i + h_i^2h_{i+1}\beta_i \\ h_{i-1}h_{i+1}^2\beta_i + 2h_ih_{i+1}^2\beta_i + h_{i+1}^3\beta_i \end{bmatrix}}{h_{i+2}(h_{i+1} + h_{i+2})(h_i + h_{i+1} + h_{i+2})(h_{i-1} + h_i + h_{i+1} + h_{i+2})} \tag{E.3}$$

$$D_i = \frac{\begin{bmatrix} h_ih_{i+1}^2 + h_ih_{i+1}h_{i+2} - h_i^3\alpha_i - 2h_i^2h_{i+1}\alpha_i - h_ih_{i+1}^2\alpha_i - h_i^2h_{i+2}\alpha_i - h_ih_{i+1}h_{i+2}\alpha_i \\ -h_ih_{i+1}h_{i+2}\beta_i - h_{i+1}^2h_{i+2}\beta_i \end{bmatrix}}{h_{i-1}(h_{i-1} + h_i)(h_{i-1} + h_i + h_{i+1})(h_{i-1} + h_i + h_{i+1} + h_{i+2})} \tag{E.4}$$

$$E_i = -(A_i + B_i + C_i + D_i) \tag{E.5}$$

For the first derivative, it is noticed that A_i, B_i, C_i, D_i and E_i are of the order $O(1/h_i)$.

The general solution for third-order second derivative, with α_i and β_i parameters, is given by:

$$A_i = \frac{2 \times \begin{bmatrix} -h_{i-1}h_i - h_i^2 + h_{i-1}h_{i+1} + 2h_ih_{i+1} + h_{i-1}h_{i+2} + 2h_ih_{i+2} + 2h_{i-1}h_i\alpha_i - h_i^2\alpha_i \\ h_{i-1}h_{i+1}\alpha_i - h_ih_{i+1}\alpha_i + h_{i-1}h_{i+2}\alpha_i - h_ih_{i+2}\alpha_i - h_{i-1}h_i\beta_i - h_i^2\beta_i \\ -2h_{i-1}h_{i+1}\beta_i - 4h_ih_{i+1}\beta_i - 3h_{i+1}^2\beta_i + h_{i-1}h_{i+2}\beta_i + 2h_ih_{i+2}\beta_i + 3h_{i+1}h_{i+2}\beta_i \end{bmatrix}}{h_{i+1}h_{i+2}(h_i + h_{i+1})(h_{i-1} + h_i + h_{i+1})} \tag{E.6}$$

$$B_i = \frac{2 \times \begin{bmatrix} 2h_{i-1}h_{i+1} + 2h_ih_{i+1} - h_{i+1}^2 + h_{i-1}h_{i+2} + h_ih_{i+2} - h_{i+1}h_{i+2} + 2h_{i-1}h_{i+1}\alpha_i \\ -3h_i^2\alpha_i + 3h_{i-1}h_i\alpha_i - 4h_ih_{i+1}\alpha_i - h_{i+1}^2\alpha_i + h_{i-1}h_{i+2}\alpha_i - 2h_ih_{i+2}\alpha_i - h_ih_{i+1}\beta_i \\ -h_{i-1}h_{i+1}\beta_i - h_{i+1}h_{i+2}\alpha_i - h_{i+1}^2\beta_i + h_{i-1}h_{i+2}\beta_i + h_ih_{i+2}\beta_i + 2h_{i+1}h_{i+2}\beta_i \end{bmatrix}}{h_{i-1}h_i(h_i + h_{i+1})(h_i + h_{i+1} + h_{i+2})} \tag{E.7}$$

$$C_i = \frac{2 \times \begin{bmatrix} h_{i-1}h_i + h_i^2 - h_{i-1}h_{i+1} - 2h_ih_{i+1} - 2h_{i-1}h_i\alpha_i + h_i^2\alpha_i - h_{i-1}h_{i+1}\alpha_i \\ h_ih_{i+1}\alpha_i + h_{i-1}h_i\beta_i + h_i^2\beta_i + 2h_{i-1}h_{i+1}\beta_i + 4h_ih_{i+1}\beta_i + 3h_{i+1}^2\beta_i \end{bmatrix}}{h_{i+2}(h_{i+1} + h_{i+2})(h_i + h_{i+1} + h_{i+2})(h_{i-1} + h_i + h_{i+1} + h_{i+2})} \tag{E.8}$$

$$D_i = \frac{2 \times \begin{bmatrix} -2h_ih_{i+1} + h_{i+1}^2 - h_ih_{i+2} + h_{i+1}h_{i+2} + 3h_i^2\alpha_i + 4h_ih_{i+1}\alpha_i + h_{i+1}^2\alpha_i \\ 2h_ih_{i+2}\alpha_i + h_{i+1}h_{i+2}\alpha_i + h_ih_{i+1}\alpha_i + h_{i+1}^2\beta_i - h_ih_{i+2}\beta_i - 2h_{i+1}h_{i+2}\beta_i \end{bmatrix}}{h_{i-1}(h_{i-1} + h_i)(h_{i-1} + h_i + h_{i+1})(h_{i-1} + h_i + h_{i+1} + h_{i+2})} \tag{E.9}$$

$$E_i = -(A_i + B_i + C_i + D_i) \tag{E.10}$$

For the second derivative, it is noted that A_i, B_i, C_i, D_i and E_i are proportional to $O(1/h_i^2)$.

For non-periodic boundaries, the above formule are no longer valid for points close to the boundaries. Non-centered approximations of lower-order developed in Appendix F must be applied instead.

Appendix F

Boundary Scheme for Non-uniform Meshes

The first derivative at boundary point $i = 1$ is calculated from Equation (D.7). Equalizing the Taylor series coefficients up to third-order leads to a linear system of equations, from which α, A, B and C at $i = 1$ can be obtained:

$$\begin{aligned} A &= -\frac{3h_2 + 2h_3}{h_2(h_2 + h_3)} \\ B &= \frac{(h_2 + h_3)(2h_3 - h_2)}{h_2 h_3^2} \\ C &= \frac{h_2^2}{h_3^2(h_2 + h_3)} \\ \alpha &= \frac{h_2 + h_3}{h_3} \end{aligned} \tag{F.1}$$

At boundary point $i = 2$, a fourth-order matching in Equation (D.8) gives

$$
\begin{aligned}
A &= -\frac{2h_3^2(2h_2+h_3)}{h_2(h_2+h_3)^3} \\
B &= \frac{2(h_3-h_2)}{h_2h_3} \\
C &= \frac{2h_2^2(h_2+2h_3)}{h_3(h_2+h_3)^3} \\
\alpha &= \frac{h_3^2}{(h_2+h_3)^2} \\
\beta &= \frac{h_2^2}{(h_2+h_3)^2}
\end{aligned} \tag{F.2}
$$

The second derivative at boundary point $i = 1$ is calculated from Equation (D.12). Equalizing the Taylor series coefficients up to second-order leads to a linear system of equations, from which A, B, C and D at $i = 1$ can be obtained:

$$
\begin{aligned}
A &= \frac{2(3h_2+2h_3+h_4+2h_3\alpha+h_4\alpha)}{h_2(h_2+h_3)(h_2+h_3+h_4} \\
B &= -\frac{2(2h_2+2h_3+h_4-h_2\alpha+2h_3\alpha+h_4\alpha)}{h_2h_3(h_3+h_4)} \\
C &= \frac{2(2h_2+h_3+h_4-h_2\alpha+h_3\alpha+h_4\alpha)}{h_3(h_2+h_3)h_4} \\
D &= -\frac{2(2h_2+h_3-h_2\alpha+h_3\alpha)}{h_4(h_3+h_4)(h_2+h_3+h_4)}
\end{aligned} \tag{F.3}
$$

At boundary point $i = 2$, a second-order matching in Equation (D.13) gives

$$
\begin{aligned}
A &= \frac{2(2h_3+h_4+3h_2\alpha+2h_3\alpha+h_4\alpha-h_3\beta+h_4\beta)}{h_2(h_2+h_3)(h_2+h_3+h_4)} \\
B &= \frac{2(2h_3-h_2+h_4+2h_2\alpha+2h_3\alpha+h_4\alpha-h_2\beta-h_3\beta+h_4\beta)}{h_2h_3(h_3+h_4)} \\
C &= \frac{2(-h_2+h_3+h_4-2h_2\alpha+h_3\alpha+h_4\alpha-h_2\beta-2h_3\beta+h_4\beta)}{} \\
D &= \frac{2(h_2-h_3-2h_2\alpha-h_3\alpha+h_2\beta+2h_3\beta)}{h_4(h_3+h_4)(h_2+h_3+h_4)}
\end{aligned} \tag{F.4}
$$

References

Apte, S., Gorokhovski, M. & Moin, P. (2003). Les of atomizing spray with stochastic modeling of secondary break-up. *Int. J. of Multiphase Flow*, **29**, 1503–1522. vi, 23, 24, 55, 98

Arcoumanis, C. & Gavaises, M. (1998). Linking nozzle flow with spray characteristics in a diesel fuel injection systems. *Atom. Sprays*, **8**, 307–347. 23

Arcoumanis, C., Gavaises, M. & French, B. (1997). Effect of fuel injection processes on the structure of diesel sprays. *SAE paper*. 23

Baev, V., Gorokhovskii, M. & Spil'berg, I. (1987). Turbulent diffusional flames in the presence of an external pressure gradient. *J. Combustion, Explosion and Shock Waves*, 266–274. 26

Bazarov, I.P. (1964). *Thermodynamics*. Oxford: Pergamon. 13

Beale, J.C. & Reitz, R.D. (1999). Modeling spray atomization with the kelvin-helmholtz/ rayleigh-taylor hybrid model. *Atomization Sprays*, **9**, 623–650. 23

Beau, P.A. (2006). *Modélisation de l'atomisation d'un jet liquid. Application aux sprays Diesel*. Ph.D. thesis, Université de Rouen. 26

Bonamy, D., Santucci, S. & Ponson, L. (2008). Crackling dynamics in material failure as a signature of a self-organized dynamic phase transition. *Phys. Rev. Lett.*, **101**. vii, 28

Carpenter, M.H., Gottlieb, D. & Abarbanel, S. (1993). The stability of numerical boundary treatments for compact high-order finite-difference schemes. *Journal of Computational Physics*, **108**, 272–295. 58

Chandrasekhar, S. (1961). *Hydrodynamic and hydromagnetic stability*. Oxford, Clarendon Press. 6, 92, 93, 95

Chigier, N.A. (1991). *Measurements in Combustion Systems, Chapter 1, Combustion Measurements*. Hemisphere Publishing Company. 1

Chtab, A. & Gorokhovski, M. (2007). Large-eddy simulation with simplified collisional microdynamics in a high reynolds number particle-laden channel flow. *Journal of Fluids Engineering*, **129**, 613–620. 52, 53

Clift, R., Grace, G. & Weber, M. (1978). *Bubbles, Drops and Particles*. Academic Press. 53

Couderc, F. (2007). *Développement d'un code de calcul pour la simulation découlements de fluides non miscibles. Application à la désintégration assistée d'un jet liquide par un courant gazeux.*. Ph.D. thesis, Ecole nationale superieure de l'aeronautique et de l'espace. 20

Daly, B.J. & Pracht., A.E. (1967). Numerical study of density current surges. *Physics of Fluids*, **11**, 15–30. 17

De Villiers, E., Gosman, A. & Weller, H. (2004). Large eddy simulation of primary diesel spray atomization. *SAE Technical paper*. 22

Desjardins, O. & Pitsch, H. (2009). A spectrally refined interface approach for simulating multiphase flows. *J. of Computational Phys.*, **228**, 1658–1677. vi, 20, 21

Dimotakis, P.E. (1986). Two-dimensional shear layer entrainment. *AIAA Journal*, **24**, 1791–1796. 7

Eggers, J. & Villermaux, E. (2008). Physics of liquid jets. *Rep. Prog. Phys.*, **71**, 79. 1, 14

Engelbert, C., Hardalupas, Y. & Whitelaw, J.H. (1995). Breakup phenomena in coaxial airblast atomizers. vol. 451 of *Issue 1941*, 189–229, Mathematical and Physical Sciences. 1, 3

Eroglu, H., Chigier, N. & Farago, Z. (1991). Coaxial atomizer liquid intact lengths. *Physics of Fluids*, **3**. 4

Farago, Z. & Chigier, N.A. (1992). Morphological classification of disintegration of round liquid jets in a coaxial air stream. *Atomization and Sprays*, **2**, 137–153. 1

Gao, D., Morley, N. & Dhir, V. (2003). Numerical simulation of wavy falling film flow using vof method. *Journal of Computational Physics*, **192**, 624–642. 22

Gel'fand, B.E., Gubin, S.A., Kogarko, S.M. & Komar, S.P. (1975). Singularities of the breakup of viscous liquid droplets in shock waves. *Journal of engineering physics and thermophysics*, **25**, 1140–1142. 8

Germano, M. (1992). Turbulence: the filtering approach. *Journal of Fluid Mechanics*, **238**, 325–336. 100

Germano, M., Piomelli, U., Moin, P. & Cabot, W.H. (1991). American institute of aeronautics and astronautics. *Physics of Fluids*, **3**, 1760–1765. 101

Ghosal, S. & Moin, P. (1995). The basic equations for the large eddy simulation of turbulent flows in complex geometry. *Journal of Computational Physics*, **118**, 24–37. 99

Gibbs, J.W. (1876). On the equilibrium of heterogeneous substances. *Trans. Connect. Acad. Sci.*, **3**, 108–248, 343–524. 13

Giles, M.B. (1990). Nonreflecting boundary conditions for euler equation calculations. *AIAA Journal*, **28**, 2050–2058. 58

Gorokhovski, M. (2001). The stochastic sub-grid-scale approach for spray atomization. *Atom. Sprays*, 505–519. 8, 9, 23, 55

Gorokhovski, M. (2010). http://www.ilasseurope2010.org/index.php?page=plenary. In *Plenary lecture, ILASS*. 11

Gorokhovski, M. (2011). Primary atomization: main approaches in modeling, comments and fragmentation. *submitted to J. New Physics*. 12

Gorokhovski, M. & Herrmann, M. (2008). Modeling primary atomization. *Annual Review of Fluid Mechanics*, **40**, 343–366. 1, 12

Gorokhovski, M. & Saveliev, V. (2008). Statistical universalities in fragmentation under scaling symmetry with a constant frequency of fragmentation. *J. Phys., D. Appl. Phys.*, **41**. 31, 36, 37

Gorokhovski, M., Jouanguy, J. & Chtab-Desportes, A. (2009). Stochastic model of the near-to-injector spray formation assistedby a high-speed coaxial gas jet. *Fluid Dynamics Research*, **41**. 7, 31, 38, 41, 42, 44

Gorokhovski, M., Deng, T. & Ribault, C.L. (2011). Simulation of air-blast atomization closely to injector: stochastic immersed body approach. *Submitted to Phys. Fluids*. 32

Gorokhovski, M.A. & Saveliev, V.L. (2003). Analyses of kolmogorov's model of breakup and its application into lagrangian computation of liquid sprays under air-blast atomization. *Physics of Fluids*, **15**, 184–192. 23, 36, 37, 55

Gueyffier, D., Li, J., Nadim, A., Scardovelli, R. & Zaleski, S. (1999). Volume-of-fluid interface tracking with smoothed surface stress methods for three-dimensional flows. *Journal of Computational Physics*, **152**. 22

Habchi, C. & Baritaud, T. (1997). Modeling atomization and break-up in high pressure diesel sprays. *SAE Pap.*. 23

Harlow, F. & Welch, J. (1965). Numerical calculation of time-dependent viscous incompressible flow of fluid with free surface. *Physics of Fluids*, **8**, 2182–2189. 17

Herrmann, M. & Gorokhovski, M. (2008). An outline of a les subgrid model for liquid/gas phase interface dynamics. In *Center for Turbulence Research, Proceedings of the Summer Program*. 20

Hirt, C. & Nichols, B. (1981). Volume of fluid (vof) methods for the dynamics of free boundaries. *Journal of Computational Physics*, **39**, 201–225. 21

Hong, M. (2003). *Atomisation et mélange dans les jets coaxiaux liquid-gaz*. Ph.D. thesis, INPG. iv, vi, vii, viii, ix, 3, 5, 6, 7, 8, 11, 40, 41, 43, 59, 67, 68, 69, 70, 75, 76, 77, 78, 79, 80, 83, 84, 88, 90

Hong, M., Cartellier, A. & Hopfinger, E. (2002). Atomisation and mixing in coaxial injection. In *Proc. 4th Int. Conf. on launcher Technology Space launcher Liquid Propulsion*, Liège, Belgium. 3

Hopfinger, E.J. (2001). In *Combustion dans les moteurs fusée Acte du Colloque de Synthèse du groupe de Recherche CNES/CNRS/ONERA/SNECMA*, 34–47. 2, 52

Hu, F.Q. (1996). On absorbing boundary conditions for linearized euler equations by a perfectly matched layer. *Journal of Computational Physics*, **129**, 201–219. 58

Huh, K. & Gosman, A. (1991). A phenomenological model of diesel spray atomization. In *Proceedings of ICMF*, Tsukuba, Japan. 23

Jay, S., Lacas, F. & Candel, S. (2006). Combined surface density concepts for dense spray combustion. *Combustion and Flame*, **144**, 558–577. vii, 26, 27

Joseph, D. & Lundgren, T. (1990). Ensemble averaged and mixture theory equations for incompressible fluid-particle suspension. *Int. J. Multiphase Flow*, **16**, 35–42. 25

Jouanguy, J. (2007). *Modélisation phénomenologique de pulvérisation de sprays couplée à une approche LES pour la phase gazeuse*. Ph.D. thesis, Université de Rouen. vii, 41, 42, 43

Juniper, M., Tripathi, A., Scouflaire, P., Rolon, J.C. & Candel, S. (2001). The structure of cryogenic flames and subcritical and supercritical pressures, in combustion dans les moteurs fusees. In *Proc. Combust. Inst.*, vol. 28, 1103–1109. vii, 26, 27

Kimura, S., Kosaka, H., Matsui, Y. & Himeno, R. (2004). A numerical simulation of turbulent mixing in transient spray by les (comparison between numerical and experimental results of transient particle laden jets). *SAE Transactions*, **113**, 1492–1500. 98

Kolmogorov, A.N. (1941). Dissipation of energy in the locally isotropic turbulence. *Doklady Akad, Nauk SSSR*, **32**, 16–18. 8, 35, 37, 103, 104

Kong, S., Senecal, P. & Reitz, R. (1999). Developments in spray modelling in diesel and direct-injection gasoline engines. *Oil and Gas Science and Technology – Rev. IFP*, **54**, 197–204. 23

Kuznetsov, V. & Sabel'nikov, V. (1990). *Turbulence and Combustion*. Hemisphere. 8

Lalo, M., Cartellier, A., Gajan, P. & Strzelecki, A. (2006). Use of faraday instabilities to enhance fuel pulverization in airblast atomizers. In *ICLASS-2006*, Kyoto, Japan. vi, 2

Landau, L.D. & Lifshitz, E.M. (1975). *The classical theory of fields (Course of theoretical physics)*. Butterworth-Heinemann. 19

Landau, L.D. & Lifshitz, E.M. (2000). *Fluid Mechanics, Second Edition: Volume 6 (Course of Theoretical Physics)*. Butterworth-Heinemann. 15, 17, 52

Lasheras, J.C. & Hopfinger, E.J. (2000). Liquid jet instability and atomization in a coaxial gas stream. *Annual Review of Fluid Mechanics*, **32**, 275–308. ix, 1, 6, 50, 81, 82

Lasheras, J.C., Villermaux, E. & Hopfinger, E.J. (1998). Break-up and atomization of a round water jet by a high-speed annular air jet. *Journal of Fluid Mechanics*, **357**, 351–379. vii, 4, 29, 30

Lebas, R. (2007). *Modelisation eulerienne de l'atomisation haute pression*. Ph.D. thesis, Université de Rouen. 26

Lele, S.K. (1992). Compact finite difference schemes with spectral-like resolution. *Journal of Computational Physics*, **103**, 16–42. 57, 107, 108

Lomnitz, C. (1994). *Fondamentals of Earthquake Predictions*. Wiley, New York. 35

Ludgren, T. (1972). Slow flow through stationary random beds and suspensions of spheres. *J. Fluid Mech.*, **51**, 273–299. 25

Måløy, K., Santucci, S., Schmittbuhl, J. & Toussaint, R. (2006). Local waiting time fluctuations along a randomly pinned crack front. *Phys. Rev. Lett.*, **96**. 28

Mansour, A. & Chigier, N. (1991). Dynamic behavior of liquid sheets. *Phys. Fluids A*, **3**, 2972–2980. 81

Marmottant, P. (2001). *Atomisation d'un liquide par un courant gazeux*. Ph.D. thesis, Institut National Polytechnique de Grenoble. 3, 5, 41

Marmottant, P. & Villermaux, E. (2004). On spray formation. *Journal of Fluid Mechanics*, **498**, 73–111. 3

Mayer, W.O.H. & Branam, R. (2004). Atomization characteristics on the surface of a round liquid jet. *Experiments in Fluids*, **36**, 528–539. 4

Ménard, T., Tanguy, S. & Berlemont, A. (2007). Coupling level set/vof/ghost fluid methods: Validation and application to 3d simulation of the primary break-up of a liquid jet. *International Journal of Multiphase Flow*, **33**, 510–524. 20

O'Rourke, P. & Amsden, A. (1987). The tab method for numerical calculation of spray droplet breakup. *SAE Paper*. 54

Osher, S. & Sethian, J. (1988). Fronts propagating with curvature dependent speed: algorithms based on hamilton-jacobi formulations. *J. Comp. Phys.*, **79**. 19

Patterson, M. & Reitz, R. (1998). Modeling the effects of fuel spray characteristics on diesel engine combustion and emissions. *SAE Pap.*. 23

Peskin, C.S. (1977). Numerical analysis of blood flow in the heart. *Journal of Computational Physics*, **25**, 220–252. 16, 17

Peskin, C.S. (2007). The immersed boundary method (handwritten lecture notes). 16

Pilch, M. & Erdman, C.A. (1987). Use of breakup time data and velocity history data to predict the maximum size of stable fragments for acceleration-induced breakup of a liquid drop. *International Journal of Multiphase Flow*, **13**, 741–757. 8

Piomelli, U. (1999). Large-eddy simulation: achievements and challenges. *Progress in Aerospace Sciences*, **35**, 335–362. 100

Plateau, J. (1873). *Statique expérimentale et théorique des liquides soumis aux seules forces moléculaires*. Gauthier-Villars, Paris. 14, 92

Pope, S. (2000). *Turbulent Flows*. Cambridge University Press. 98, 100

Rayana, M.B. (2007). *Contribution à l'étude des instabilités interfaciales liquid-gaz en atomisation assistée et tailles de gouttestude des instabilités interfaciales liquid-gaz en atomisation assistée et tailles de gouttes*. Ph.D. thesis, INPG. vi, 3, 6, 20, 21, 40

Rayleigh, L. (1878). On the instability of jets. In *Proceedings London Mathematical Society*. 92

Raynal, L. (1997). *Instabilité et entraînement à l'interface d'une couche de mélange liquid-gaz*. Ph.D. thesis, UJF. 3, 5

Razumovsky, N. (1940). On a distribution character of metals contents in ore fields. *DAN SSSR*, **28**. 35

Reeks, M. (1977). On the dispersion of small particles suspended in an isotropic turbulent fluid. *J. Fluid Mech.*, **83**, 529. 54

Rehab, H. (1997). *Structure de l'écoulement et mélange dans le champs proche des jets coaxiaux*. Ph.D. thesis, UJF. 3

Rehab, H., Villermaux, E. & Hopfinger, E.J. (1997). Flow regimes of large velocity ratio coaxial jets. *Journal of Fluid Mechanics*, **345**, 357–81. 3

Reitz, R.D. (1987). Modeling atomization processes in high-pressure vaporizing sprays. *Atomisation and Spray Technology*, **3**, 309–337. 23, 54, 55

Rodi, W. (1976). A new algebraic relation for calculating the reynolds stresses. *ZAMM*, **56**, 219–221. 26

Rudy, D.H. & Strikwerda, J.C. (1980). A nonreflecting outflow boundary condition for subsonic navier-stokes calculations. *Journal of Computational Physics*, **36**, 55–70. 58

Saffman, P. (1971). On the boundary condition at the surface of a porous medium. *Stud. Appl. Math.*, **93**. 25

Smagorinsky, J. (1963). General circulation experiments with the primitive equations. *Monthly Weather Review*, **91**, 99–164. 101

Smereka, P. (2003). Lecture notes for inria short course on level set methods for incompressible two phase flow. 18, 19

Sone, K. & Menon, S. (2003). The effect of subgrid modeling on the in-cylinder unsteady mixing process in a direct injection engine. *ASME Journal of Engineering for Gas Turbines and Power*, **125**, 435–443. 98

Sornette, D. (2000). *Critical Phenomena in Natural Science*, 81. Springer, Berlin, Heidelberg, New York. 29

Stanley, S.A., Sarkar, S. & Mellado, J.P. (2002). A study of the flow-field evolution and mixing in a planar turbulent jet using direct numerical simulation. *J. Fluid Mech.*, **450**, 377–407. 57

Sussman, M. (1994). *A level set approach for computing solutions to incompressible two-phase flow*. Ph.D. thesis, PhD dissertation Department of Mathematics, University of California. 19

Sussman, M. & Puckett, E. (2000). A coupled level set and volume-of-fluid method for computing 3d and axisymmetric incompressible two-phase flows. *Journal of Computational Physics*, **162**, 301–337. 22

Sussman, M. & Smereka, P. (1997). Axisymmetric free boundary problems. *J. Fluid Mech.*, **341**, 269–294. 19

Sussman, M., Smereka, P. & Osher, S. (1994). A level set approach to computing solutions to incompressible two-phase flow. *J. Comp. Phys.*, **114**, 146. 19

Sussman, M., Fatemi, E., Smereka, P. & Osher, S. (1996). An improved level set method for incompressible two-fluid flows. *Computers and Fluids*. 19

Tanguy, S. (2004). *Développement d'une methode de suivi d'interface. Applications aux écoulements diphasiques.*. Ph.D. thesis, Université Rouen. 20

Tanner, F.X. (2004). Development and validation of a cascade atomization and drop breakup model for high-velocity dense sprays. *Atomisation and Sprays*, **14**, 211–242. 23

Taylor, G. (1963). *The shape and acceleration of a drop in a high-speed air stream. In: Batchelor GK (ed) The scientific papers of GI Taylor, vol III.*, 81. University Press, Cambridge. 54

Thompson, K.W. (1987). Time dependent boundary conditions for hyperbolic systems. *Journal of Computational Physics*, **68**, 1–24. 58

Trontin, P. (2009). *Développement d'une approche de type LES pour la simulation d'écoulements diphasiques avec interface. Application à l'atomisation primaire.*. Ph.D. thesis, Ecole nationale superieure de l'aeronautique et de l'espace. vii, 20, 31

Tryggvason, G. & Unverdi, S.O. (1992). A front-tracking method for viscous, incompressible, multi-fluid flows. *J. Comput. Phys.*, **100**, 25–37. 18

Vallet, A., Burluka, A. & Borghi, R. (2001). Development of an eulerian model for the atomization of a liquid jet. *Atomization and Sprays*, **11**, 619–642. 25, 26

Varga, C.M. (2002). *Initial break-up of a small diameter liquid jet by high-speed gas stream*. Ph.D. thesis, UCSD, San Diego. vi, 3, 6, 7, 8, 40

Varga, C.M., Lasheras, J.C. & Hopfinger, E.J. (2003). Initial breakup of a small diameter liquid jet by high-speed gas stream. *Journal of Fluid Mechanics*, **497**, 405–434. 3, 6, 41

Vargaftik, N., Vinogradov, Y. & Yargin, V. (1996). *Handbook of physical Properties of Liquids and Gases*, 1359. Begell House. 14

Villermaux, E. (1998). Mixing and spray formation in coaxial jets. *Journal of propulsion and power*, **14**, 807–817. 5, 50

Villermaux, E. (2007). Fragmentation. *Annual Review of Fluid Mechanics*, **39**, 419–446. 1

Vreman, B., Geurts, B. & Kuerten, H. (1996). Comparison of numerical schemes in large-eddy simiulation of the temporal mixing layer. *International Journal for Numerical Methods in Fluids*, **22**, 297–311. 101

Wang, L. & Stock, D. (1993). Dispersion of heavy particles in turbulent motion. *J. Atmos. Sci.*, **50**, 1897. 54

Wei, N. (2007). *Development of a Next-generation Spray and Atomization Model Using an Eulerian-Lagrangian Methodology*. Ph.D. thesis, University of Wisconsin – Madison. 26

Wilcox, D. (1993). *Turbulence Modeling for CFD*. DCW Industries,Inc. 97

Yi, Y. & Reitz, R. (2004). Modeling the primary break-up of high-speed jets. *Atom. Sprays*, **14**, 53–80. 23

Zaichik, L. & Alipchenkov, V. (2003). Pair dispersion and preferential concentration of particles in isotropic turbulence. *Phys. Fluids*, **15**, 1776. 54

Zaichik, L., Simonin, O. & Alipchenkov, V. (2003). Two statistical models for predicting collision rates of inertial particles in homogeneous isotropic turbulence. *Phys. Fluids*, **15**, 2995. 54

Zamansky, R., Vinkovkc, I. & Gorokhovski, M. (2010). Les approach coupled with stochastic forcing of subgrid acceleration in a high-reynolds-number channel flow. *J. Turbul.*, **11**, 1–18. vii, 44, 47